



**PHD**

**Meshless Additive Manufacturing**

Kim, Soo-Hwa

*Award date:*  
2022

*Awarding institution:*  
University of Bath

[Link to publication](#)

**Alternative formats**

If you require this document in an alternative format, please contact:  
[openaccess@bath.ac.uk](mailto:openaccess@bath.ac.uk)

Copyright of this thesis rests with the author. Access is subject to the above licence, if given. If no licence is specified above, original content in this thesis is licensed under the terms of the Creative Commons Attribution-NonCommercial 4.0 International (CC BY-NC-ND 4.0) Licence (<https://creativecommons.org/licenses/by-nc-nd/4.0/>). Any third-party copyright material present remains the property of its respective owner(s) and is licensed under its existing terms.

**Take down policy**

If you consider content within Bath's Research Portal to be in breach of UK law, please contact: [openaccess@bath.ac.uk](mailto:openaccess@bath.ac.uk) with the details. Your claim will be investigated and, where appropriate, the item will be removed from public view as soon as possible.

# Meshless Additive Manufacturing

Soo-Hwa Kim

A thesis submitted for the degree of Doctor of Philosophy

University of Bath

Department of Mechanical Engineering

March 2022

## COPYRIGHT

Attention is drawn to the fact that copyright of this thesis rests with the author and copyright of any previously published materials included may rest with third parties. A copy of this thesis has been supplied on condition that anyone who consults it understands that they must not copy it or use material from it except as licenced, permitted by law or with the consent of the author or other copyright owners, as applicable.

Signature of Author .....

Soo-Hwa Kim





## Abstract

Additive manufacturing (AM) processes produce components by adding material in a layer-by-layer fashion. This allows new types of geometries to be feasible, particularly lattice structures. Although lattices are possible to additively manufacture, the modelling capabilities and customisation is greatly limited by the current conventional AM process flow due to their complex topologies. Within the process flow, there are several stages that use mesh-based modelling posing a costly trade-off between computational memory limits and geometric accuracy.

Meshless implicit-based modelling overcomes the bottlenecks arising from mesh-based issues. This approach is ideal for a sub-class of lattices called triply-periodic minimal surfaces (TPMS) that are defined by a single implicit function. These lattices are gaining popularity in industries and the AM community due to their high surface-area-to-volume ratio, infinitely smooth, and non-self intersecting properties. These properties highlight the challenges presented by conventional mesh-based modelling, promoting a need for an alternative implicit-based modelling approach.

The vision in this thesis is to expand design capabilities and customisation of AM lattice structures, specifically focussing on TPMS, without using mesh-based modelling. The approach taken in this thesis is to customise TPMS by altering the implicit functions to design specification and then directly slicing the manipulated functions as infill. As is, TPMS implicit functions define infinitely thin lattices that are not feasible to manufacture. The functions can be manipulated to create lattice structures, however, the resulting geometry from the manipulated functions was not intuitive. As such the first part of this research was to characterise the resulting geometric properties from manipulating the implicit functions.

Once characterised, such that the TPMS can be customised to a certain geometric specification, this can be used in a direct slicing process flow to fabricate customised TPMS structures. The next step was to create an algorithm to generate toolpaths for an AM machine using manipulated TPMS functions. From this, printed TPMS structures could be related using experimental methods to link engineering properties to the geometric properties. This link enables designers to create lattices in a more purposeful way without the need to use CAD.

Resulting from this research, this thesis presents the following novel research contributions. Firstly, a set of numerical methods were established to calculate the volume fraction, surface area, and minimum thickness of manipulated TPMS structures to a known accuracy tolerance. Next by using this set, empirical geometric relationships between the manipulated implicit functions and the geometric properties were established. Finally, a method was developed to AM TPMS structures with tunable geometric or mechanical properties without using mesh-based methods. The developments achieved in this thesis promote the use of implicit-based modelling and TPMS structures in AM.

# List of Publications

- Kim, S. M., J. Stirling, J. M. Flynn, “*Volume fraction, surface area, and minimum thickness parameters for five triply-periodic minimal surfaces*”, Progress in Additive Manufacturing, **Submitted**, (2022).
- E. R. Rahal, T. Jeremiah, Kim, S. M., K. Fraser, O. J. Pountney, J. M. Flynn, *Approximations of Triply Periodic (Minimal) Gyroid Surfaces for use in CAD Modelling and Simulations*, **In Preparation**, (2022).
- Kim, S. M., J. M. Flynn, “*Adaptive Direct Slicing of Solid and Sheet TPMS Structures for FDM*”, International Journal of Computer Integrated Manufacturing, **In Preparation**, (2022).

# Acknowledgments

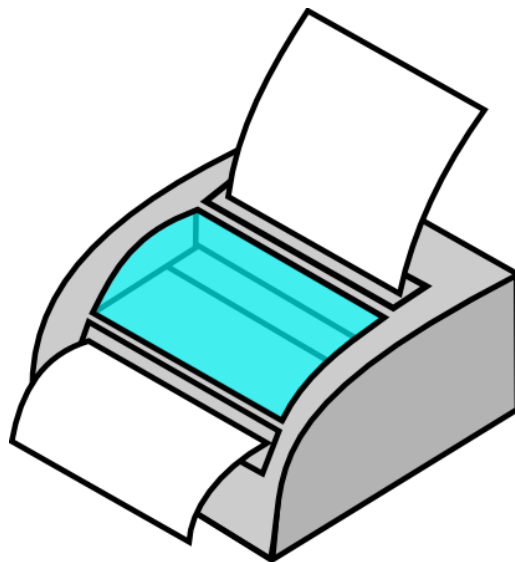
I would first like to express my gratitude to my primary supervisor, Joseph Flynn, for his guidance, patience, and motivation during these last three years. As his first PhD student, I am honoured to have been at the beginning of his own research group and excited by what we achieved in the following years. Thank you for granting me the opportunity to work in such an exciting domain. Next I want to thank my second supervisor, Vimal Dhokia, for his unwavering support, enthusiastic career advice, and positive energy. His genuine care and continuous encouragement helped to keep me sane, focussed, and on track during the pandemic. I would also like to thank Nigel Johnston, Evros Loukaides, and Steve Newman for their long-term support and advice. I also appreciate my viva examiners Andrew Plummer and Jonathan Corney for a great viva experience and helpful insight. Finally, thank you to all my friends from AMPS, the mechanical engineering department, the physics department, and kickboxing (Steph Hall, Gauthier Fieux, Fedra Zaribaf, Jasmine Rance, Debbie Janson, Lorenzo Giunta, Max Valentine, Joe Betts, Ben Rogers, and many more!) for being on this adventure with me and for all the fun memories of cats, tiny hands, googly eyes, bananas, garlic bread lollipops, and frog windsocks.

Outside of the university, I'd first like to thank my best friend, Brooke Lathon, for all her love and friendship over the years. I am so excited about the start of her own family with her new little one and for her own upcoming PhD adventure. Also, I'd like to thank my foodie friends from APL for all the snacks and delicious pho lunches. Thank you to the Claverton Pumping Station and fellow volunteers for the fulfilling projects from building sheds to making bonfires and the exposure to English heritage. I also want to thank The Packhorse for helping me keep my sanity.

Last but not least, I would like to thank my family. To my beardy husband, Julian Stirling, I cannot thank you enough for patiently being with me through all the highs and lows over the years. Your continual encouragement, advice, and silly songs got me through my PhD. You have made my PhD and move to England such a wonderful experience. I'm so lucky to be your wife and I just love you so much. Additionally, I'd like to thank my in-laws for the loving support, fun vacations around England, and lovely Christmases together. 나의 가족에게 많은 감사를 드립니다. 엄마, 기니, 호돌이 그리고 한국에 거주하시는 이모님. 그들의 끊임없는 기도와 사랑, 특히 이모님과 엄마가 보내주시는 간식은 나에게 많은 용기와 따뜻한 격려가 되었습니다. 사랑해요.

---

Don't let your printer know you are in a hurry



they smell fear.

# Contents

|  |             |
|--|-------------|
| <b>Abstract</b>  | <b>i</b>    |
| <b>List of Publications</b>  | <b>ii</b>   |
| <b>Acknowledgments</b>   | <b>iii</b>  |
| <b>List of Figures</b>   | <b>viii</b> |
| <b>List of Tables</b>  | <b>xi</b>   |
| <b>1 Introduction</b>  | <b>1</b>    |
| <b>2 Review of Additively Manufactured Lattices</b>                              | <b>4</b>    |
| 2.1 Introduction . . . . .   | 4           |
| 2.2 Additive Manufacturing Current Status . . . . .                              | 4           |
| 2.2.1 Definition and Brief History . . . . .                                     | 4           |
| 2.2.2 Conventional Additive Manufacturing Process Flow . . . . .                 | 5           |
| 2.2.3 Additive Manufacturing Comparison with Traditional Manufacturing . . . . . | 7           |
| 2.2.4 Trending Industrial Applications of AM . . . . .                           | 9           |
| 2.3 Additively Manufactured Lattices . . . . .                                   | 12          |
| 2.3.1 Lattice Geometries . . . . .   | 12          |
| 2.3.2 Benefits of Manufacturing Lattices . . . . .                               | 12          |
| 2.3.3 Current Process for Additively Manufacturing Lattices . . . . .            | 14          |
| 2.3.4 Current Difficulties of Manufacturing Lattices . . . . .                   | 15          |
| 2.4 Emerging Methods . . . . .   | 18          |
| 2.4.1 Current Emerging Methods . . . . .   | 18          |
| 2.4.2 Triply-Periodic Minimal Surfaces . . . . .                                 | 21          |
| 2.4.3 Unresolved Challenges . . . . .  | 25          |
| <b>3 Research Aim, Objectives, and Scope</b>                                     | <b>29</b>   |
| 3.1 Introduction . . . . .   | 29          |
| 3.2 Aim, Objectives, and Contributions . . . . .                                 | 29          |
| 3.2.1 Research Aim . . . . .   | 29          |
| 3.2.2 Research Objectives . . . . .  | 30          |
| 3.2.3 Research Contributions . . . . .   | 31          |

---

|          |  |           |
|----------|--|-----------|
| 3.3      | Research Scope and Boundaries . . . . .  | 32        |
| 3.3.1    | Geometric Property Calculation Phase . . . . .                                 | 32        |
| 3.3.2    | Toolpath Algorithm Development Phase . . . . .                                 | 32        |
| 3.3.3    | Experimental Phase . . . . .   | 33        |
| 3.3.4    | Research Boundaries . . . . .  | 33        |
| <b>4</b> | <b>Research Methodology and Framework</b>                                      | <b>35</b> |
| 4.1      | Research Context . . . . .   | 35        |
| 4.2      | Research Framework . . . . .   | 36        |
| 4.3      | Research Methodology . . . . .   | 36        |
| 4.3.1    | Implicit Modelling Methods . . . . .   | 36        |
| 4.3.2    | Geometric Property Calculation Phase . . . . .                                 | 38        |
| 4.3.3    | Toolpath Algorithm Development Phase . . . . .                                 | 40        |
| 4.3.4    | Experimental Phase . . . . .   | 42        |
| 4.4      | Summary . . . . .  | 43        |
| <b>5</b> | <b>Calculation of TPMS Geometric Properties</b>                                | <b>44</b> |
| 5.1      | Introduction . . . . .   | 44        |
| 5.2      | Background of TPMS structures . . . . .  | 44        |
| 5.2.1    | Definition of the Geometric Properties . . . . .                               | 46        |
| 5.2.2    | Convergence Testing . . . . .  | 47        |
| 5.3      | Numerical Techniques for Geometric Calculations . . . . .                      | 47        |
| 5.3.1    | Assessment of Various Numerical Techniques . . . . .                           | 47        |
| 5.3.2    | Formulated Set of Numerical Techniques . . . . .                               | 53        |
| 5.4      | Generating Datasets . . . . .  | 53        |
| 5.4.1    | MATLAB Program . . . . .   | 54        |
| 5.4.2    | Mesh-free Monte Carlo Estimation of Volume Fraction . . . . .                  | 55        |
| 5.4.3    | Coarse Sampling of the TPMS Unit Cells for Mesh-Based<br>Estimations . . . . . | 55        |
| 5.4.4    | Convergence for Mesh-Based Estimations . . . . .                               | 58        |
| 5.4.5    | Mesh-Based Estimation of the Surface Area . . . . .                            | 58        |
| 5.4.6    | Mesh-Based Estimation of the Minimum Thickness . . . . .                       | 59        |
| 5.4.7    | Robust Chebyshev Fitting . . . . .   | 60        |
| 5.5      | Results . . . . .  | 62        |
| 5.5.1    | Volume Fraction . . . . .  | 63        |
| 5.5.2    | Surface Area . . . . .   | 64        |
| 5.5.3    | Minimum Thickness . . . . .  | 65        |
| 5.6      | Discussion . . . . .   | 66        |
| 5.7      | Conclusion . . . . .   | 70        |
| <b>6</b> | <b>Adaptive Direct Slicing of TPMS Structures</b>                              | <b>72</b> |
| 6.1      | Introduction . . . . .   | 72        |
| 6.2      | Investigating Current Infill Techniques . . . . .                              | 74        |
| 6.3      | Direct Slicing Toolpath Algorithm . . . . .                                    | 76        |
| 6.3.1    | Customised TPMS Structure Inputs . . . . .                                     | 76        |

---

|          |   |            |
|----------|---|------------|
| 6.3.2    | Calculate Adjacent Contour Isovalues . . . . .                          | 77         |
| 6.3.3    | Calculate Contour Lines Per Slice . . . . .                             | 80         |
| 6.3.4    | Convert To GCode . . . . .  | 81         |
| 6.4      | Discussion . . . . .  | 83         |
| 6.4.1    | Streamlined AM Process Flow . . . . .                                   | 83         |
| 6.4.2    | Opportunities for Continued Development . . . . .                       | 85         |
| 6.5      | Conclusion . . . . .  | 86         |
| <b>7</b> | <b>Experimental Application in Additive Manufacturing</b>               | <b>88</b>  |
| 7.1      | Introduction . . . . .  | 88         |
| 7.2      | Test Specimen Information . . . . .                                     | 88         |
| 7.3      | PLA Density Measurement . . . . .                                       | 89         |
| 7.4      | Volume Fraction Measurements . . . . .                                  | 90         |
| 7.5      | Compression Testing . . . . .   | 93         |
| 7.6      | Calculate Gibson-Ashby Relationship . . . . .                           | 94         |
| 7.7      | Discussion . . . . .  | 95         |
| 7.8      | Conclusion . . . . .  | 98         |
| <b>8</b> | <b>Discussions and Conclusions</b>                                      | <b>99</b>  |
| 8.1      | Introduction . . . . .  | 99         |
| 8.2      | Overarching Discussion . . . . .  | 99         |
| 8.3      | Conclusions . . . . .   | 101        |
| 8.4      | Future Works . . . . .  | 102        |
| 8.4.1    | Optimisation of Toolpath Algorithm . . . . .                            | 103        |
| 8.4.2    | Tunable Properties for Wide Range of Engineering Applications . . . . . | 103        |
|          | <b>Appendices</b>   | <b>128</b> |
| <b>A</b> | <b>Appendix: Polynomial Fitting and Residual Plots</b>                  | <b>129</b> |
| <b>B</b> | <b>Appendix: Experimental Compressive Testing Plots</b>                 | <b>145</b> |



# List of Figures

|      |  |    |
|------|--|----|
| 2.1  | The conventional AM process flow . . . . .   | 6  |
| 2.2  | Step-like surface finish of FDM parts . . . . .  | 7  |
| 2.3  | Examples of issues that can arise from AM . . . . .  | 8  |
| 2.4  | Primitive unit cell (simple cubic) and 3D lattice composed of multiple unit cells. The lattice was created by translating the unit cell in 3D. . . . . | 12 |
| 2.5  | Simple cubic, body-centred cubic, and face-centred cubic lattice primitive unit cells . . . . .  | 12 |
| 2.6  | Heat exchanger with a lattice design . . . . .   | 13 |
| 2.7  | Parametric modelling of structure boundaries . . . . .   | 14 |
| 2.8  | Two possible AM process flows for creating lattices . . . . .  | 16 |
| 2.9  | Planar triangular facet versus a curved Bézier triangular facet . .  | 17 |
| 2.10 | Example of STL estimation resolution . . . . .   | 18 |
| 2.11 | General method for the marching squares algorithm . . . . .  | 19 |
| 2.12 | Examples of implicitly-based modelling and slicing . . . . .   | 19 |
| 2.13 | The AM process flow with direct slicing method . . . . .   | 20 |
| 2.14 | Examples of TPMS: Schwartz Primitive, Schoen Gyroid, Schwartz Diamond, Neovius, Schoen iWP . . . . .   | 21 |
| 2.15 | TPMS fundamental patch . . . . .   | 22 |
| 2.16 | Creation of a TPMS lattice from a fundamental patch . . . . .  | 23 |
| 2.17 | Two methods for adding volume to TPMS structures . . . . .   | 26 |
| 2.18 | TPMS structures created using multiple isovalues . . . . .   | 26 |
| 2.19 | Feng <i>et al.</i> method for implicit direct slicing . . . . .  | 27 |
| 2.20 | Ding <i>et al.</i> method for implicit direct slicing . . . . .  | 27 |
| 4.1  | Identified bottlenecks in the conventional AM process flow . . . .   | 35 |
| 4.2  | Thesis research framework . . . . .  | 36 |
| 4.3  | TPMS Gyroid volume change with varying isovalues . . . . .   | 37 |
| 4.4  | 2D slice of a single unit cell of Primitive showing the distinct subvolumes . . . . .  | 38 |
| 4.5  | 3D depiction of single unit cell of Primitive showing the distinct subvolumes . . . . .  | 39 |
| 4.6  | Example of filler contour line vs. solid hatching toolpaths . . . .  | 41 |
| 5.1  | Primitive unit cell set to different isovalues . . . . .   | 45 |

---

|      |   |    |
|------|---|----|
| 5.2  | Single unit cells of the Primitive, Gyroid, Diamond, Neovius, and iWP for single and double surface structures . . . . .  | 47 |
| 5.3  | Gradient descent method to correct vertices . . . . .   | 48 |
| 5.4  | Vertex correction using explicit functions and resulting mesh issues  | 49 |
| 5.5  | Multiple meshes required for deterministic volume fraction calculation . . . . .  | 50 |
| 5.6  | Quasi-Monte Carlo integration method for surface area calculation   | 50 |
| 5.7  | Quasi-Monte Carlo integration parameters . . . . .  | 51 |
| 5.8  | Comparison of accuracy of the quasi Monte Carlo method vs. the triangular mesh area method . . . . .                      | 52 |
| 5.9  | Fast marching method for minimum thickness calculation . . . . .  | 53 |
| 5.10 | Fast marching method ambiguity issues . . . . .   | 54 |
| 5.11 | Flowchart for MATLAB program used to calculate TPMS geometric properties . . . . .  | 56 |
| 5.12 | Volume fraction convergence with increasing number of randomised points . . . . .   | 57 |
| 5.13 | Monte Carlo integration method for volume fraction . . . . .  | 58 |
| 5.14 | Triangular mesh midpoint subdivision . . . . .  | 59 |
| 5.15 | Definition minimum thickness used . . . . .   | 60 |
| 5.16 | Comparison of the volume fraction as a function of normalised isovalue for all single surface TPMS structures . . . . .   | 63 |
| 5.17 | Contour plot showing volume fractions for all possible isovalue combinations for Primitive . . . . .                      | 64 |
| 5.18 | Comparison of the volume fraction as a function of normalised isovalue for all double surface TPMS structures . . . . .   | 65 |
| 5.19 | Comparison of the surface area as a function of normalised isovalue for all single surface TPMS structures . . . . .      | 66 |
| 5.20 | Comparison of the surface area as a function of normalised isovalue for all double surface TPMS structures . . . . .      | 67 |
| 5.21 | Comparison of the minimum thickness as a function of normalised isovalue for all single surface TPMS structures . . . . . | 68 |
| 5.22 | Comparison of the minimum thickness as a function of normalised isovalue for all double surface TPMS structures . . . . . | 69 |
| 5.23 | Comparison of SAVR as a function of normalised isovalue for all single surface TPMS structures . . . . .                  | 70 |
| 6.1  | General process flow for the CAM stage for FDM . . . . .  | 73 |
| 6.2  | Toolpath line instructions . . . . .  | 73 |
| 6.3  | Process for creating Gyroid infill toolpaths for a slice in PrusaSlicer   | 75 |
| 6.4  | Direct slicing toolpath algorithm steps . . . . .   | 76 |
| 6.5  | Adjusting isovalues based on nozzle size . . . . .  | 78 |
| 6.6  | Adjacent filament line spacing . . . . .  | 79 |
| 6.7  | Gyroid surface beyond lattice isovalue range . . . . .  | 79 |
| 6.8  | Labelled photograph of line types on printed Gyroid double and single surface structures . . . . .                        | 80 |

---

---

|      |   |     |
|------|---|-----|
| 6.9  | Evaluation of MATLAB <code>contourc</code> estimation error . . . . .   | 81  |
| 6.10 | Printed Gyroid parts showing before and after the Newton-Raphson<br>correction . . . . .  | 82  |
| 6.11 | Reorganisation of contour line coordinate print order . . . . .   | 82  |
| 6.12 | Printed brim feature implementation . . . . .   | 83  |
| 6.13 | Printed wipe feature implementation . . . . .   | 83  |
| 6.14 | Simulation print display from a GCode file . . . . .  | 84  |
| 6.15 | Gaps between filament due to thickness distribution of varying<br>isovalues . . . . .   | 85  |
| 6.16 | Gaps between filament at primitive patch vertex . . . . .   | 86  |
| 6.17 | Gaps due to primitive patch vertex shown on printed double and<br>single surface structures . . . . .                           | 87  |
| 7.1  | Printed specimens of eight thickness levels of varying volume frac-<br>tions . . . . .  | 90  |
| 7.2  | Printed specimen on printer bed with labelled $x, y, z$ directions . .  | 91  |
| 7.3  | Plot showing the discrepancy between the measured and calculated<br>volume fraction . . . . .                                   | 92  |
| 7.4  | Progression of compressive testing . . . . .  | 93  |
| 7.5  | Two types of compressive stress-strain curve behaviour . . . . .  | 95  |
| 7.6  | Nonlinear fitting of the measured volume fraction and Young's<br>modulus data values for the Gibson-Ashby power law constants . | 96  |
| 7.7  | Plot showing the discrepancy between the measured and calculated<br>Young's modulus . . . . .                                   | 97  |
| 8.1  | The work flow of this research . . . . .  | 100 |

---

# List of Tables

|     |  |    |
|-----|--|----|
| 5.1 | TPMS valid isovalue range and normalisation factor . . . . .       | 46 |
| 7.1 | Test specimen information summary . . . . .                        | 89 |
| 7.2 | Corresponding isovalues to test specimen thickness level . . . . . | 90 |
| 7.3 | Mass and length measurements with uncertainties . . . . .          | 92 |



# Chapter 1

## Introduction

Additive manufacturing (AM) is one of the key elements of the fourth industrial revolution, i.e. the recent movement towards intelligent automation and production [1, 2]. This is due to its unique automated manufacturing process that fabricates parts by adding material in a layer-by-layer fashion. This allows for manufacturing highly customised parts using different types of AM technologies, feed material, and novel geometries. Thus, AM is rapidly expanding across multiple industries including aerospace, electrical components, architecture, and healthcare [3–7].

The conventional AM process flow is the same regardless of the AM technology. The process flow starts from a virtual 3D model designed in either computer-aided design (CAD) or reverse engineering techniques, e.g. laser scanning. The model then is exported to a computer-aided manufacturing (CAM) software using an intermediary file. Within the CAM software, it is sliced into layers and prepared for the AM machine. The slice instructions are exported as machine code for the AM machine. The AM machine automatically fabricates the part by adding material in layers. Finally, any post-processing is performed as needed.

Due to a conventional process flow, various AM technologies, and feed materials, AM offers several advantages as a manufacturing process. The three main advantages AM offers are the novel feasible geometries, highly customised parts, and a local manufacturing distribution model [3,5,6,8]. From this, AM has opened up the possibility of manufacturing various customised lattice structures which were previously difficult or impossible to manufacture [9]. Lattices and cellular scaffolds are commonly found throughout nature, for example atomic bonding in crystals, soap films, and inner bone matrices [10]. Lattices have high surface-area-to-volume-ratio (SAVR), porous networks, and are lightweight. This is appealing to multiple industries as this enhances biomimicry for medical implants, lightweight aircraft saving material cost, creates novel geometries for heat exchangers, electrical components, and more [3–7,9,11,12].

Modelling lattice structures in the conventional AM process flow occurs at either the CAD stage or the CAM stage. However, there are modelling difficulties associated with both of these stages. It is challenging to model lattices with traditional CAD software. Traditional CAD software estimates surfaces using

---

parametric surface patches. As lattices have a high SAVR, this requires a large number of patches to describe the shape accurately [16, 144–146]. This becomes increasingly computationally expensive as the surface area and curvature of the lattice increases. This also similarly suffers during the transfer from the CAD software to the CAM software as most intermediary file formats estimate surfaces with triangular meshes [13–17]. Alternatively, lattice structures modelled at the CAM stage as infill, are computationally efficient. However, the infill types and customisation options are usually limited or not present depending on the AM technology and the software company. This is because infill is not traditionally based on designed engineering requirements but the designs are loosely based on the strength, production time, and material consumption. These modelling difficulties limit AM lattice design capabilities.

There are newly emerging CAD software that specialise in modelling lattice structures. They have implicitly-based kernels that model shapes using implicit functions rather than parametric surface patches [18, 19]. As such, this is an efficient method to model any surface that can be described by implicit functions. In particular, TPMS are a sub-class of lattices that can be modelled with a single implicit function. These surfaces are infinitely smooth, minimal surfaces, free of self-intersections, and are embedded in  $\mathbb{R}^3$ . These unique attributes have gained a lot of attention in the AM community and industry. There is a considerable ongoing research effort across many industrial applications and the physical properties, such as mechanical properties and fluidics [20]. Also, an additional advantage of TPMS being defined as a single implicit function is the function can be easily manipulated to alter the lattice structure. Currently, AM of TPMS also faces the same modelling difficulties as other AM lattice structures as well as the challenges with geometrical customisation due to the complex mathematics of the TPMS implicit functions.

The goal of this thesis is expanding the capability of the AM of lattice structures, focussing on TPMS. The approach taken in this thesis is by using methods that do not rely on mesh-based modelling, hence meshless AM. The developed methods and algorithms attempt to reach audiences beyond those who have access to expensive software licenses or advanced mathematical and programming capabilities.

The outline of this thesis to accomplish this goal is as follows. This thesis starts in Chapter 2 by reviewing the literature, focussing on the AM of lattice structures, understanding the process flow bottlenecks, and identifying the research gaps. From this, in Chapter 3 the aims, objectives, and scope are set for this research. Then Chapter 4 objectively frames this research and discusses the methodology to address each bottleneck. The next three chapters detail the main research of this thesis. Chapter 5 addresses the geometrical customisation difficulties of TPMS. This is done by establishing robust relationships between the TPMS implicit function and the geometric properties. From this, Chapter 6 describes a novel method to AM geometrically customised TPMS. This chapter goes into detail about the development of a direct slicing toolpath algorithm that bypasses the need for mesh-based modelling. This is based on the geometric rela-

tionships developed in the previous chapter. Then, in Chapter 7, an experimental campaign was conducted to test manufactured specimens based on methods from the previous chapter. Volume measurements and compression testing related compressive mechanical properties to the volume fractions and the results were compared with the simulated calculations. This thesis closes in Chapter 8 with an overarching discussion, conclusions, and future work ideas.



# Chapter 2

## Review of Additively Manufactured Lattices: Global Trends and Computational Challenges

### 2.1 Introduction

This chapter presents a review of the literature of AM lattices. The review begins by highlighting the current status of AM development, the comparison of AM with traditional manufacturing processes, and trending AM applications in industry. This then sets the stage for the review of AM lattices, which covers the current status, challenges, and research gaps.

### 2.2 Additive Manufacturing Current Status

#### 2.2.1 Definition and Brief History

AM, also referred to as 3D printing, is a process that builds components by adding feed material in layers to physically reproduce a digital 3D model of an object. This differs from traditional subtractive manufacturing methods that start with bulk material and remove material until the desired component remains, such as milling from a solid block of metal. Developed in the 1980s, multiple AM technologies were developed and patented [21–24]. Then in 2005, Dr. Adrian Bowyer from the University of Bath started the RepRap project [25]. The RepRap project goal was to develop low-cost, open-source AM machines that could manufacture most of their own components. The impact from this project is that AM has become more attainable globally for a wider audience. Today, some AM machines can cost as low as approximately £200, whereas in the 1980s, they would have costed equivalent to almost £500,000 by today’s economy [26, 27].

The layer-wise manufacturing approach of AM affords numerous key benefits [21]. Principally, novel geometries, such as enclosed complex architectures, are not only possible but customisable. In addition, AM is capable of manufacturing with a wide range of materials. These design capabilities offer a wide range of customisation to designers.

### 2.2.2 Conventional Additive Manufacturing Process Flow

AM encompasses many technologies that differ with machinery and material [28]. However, the conventional process flow is the same for all technologies [21]. The stages are as follows, and presented in Figure 2.1:

1. The desired 3D component is digitally modelled either using CAD software or reverse engineering techniques, i.e. reproducing a 3D digital model from laser scanning a physical object.
2. The 3D model is outputted to a file format that is compatible with the CAM software, usually a stereolithography (STL) file. This intermediary file typically estimates the 3D model geometry using a triangular mesh.
3. The intermediary file is imported into the CAM software, also known as the toolpath planner software or slicer software. This software is either downloaded onto a personal computer or is on a computer directly connected to the AM machine. The software is often of the same company as the AM machine to create machine-specific machine code [29].

Once the intermediary file is imported, the model is edited, such as material and infill, and the printer settings are applied, such as sizing, orientation, support material, and positioning on the build platform. The edited model is then sliced into layers along the vertical axis relative to the printer bed. These layers describe the model in a 2D plane as toolpaths for the machine. The editing and slicing phase can be repeated multiple times until finalised. Finally, these instructions are exported as a machine code file format, e.g. a GCode file, to the AM machine.

4. The machine automatically runs based on the printer settings and the machine code instructions. The AM machine fabrication process and the material depend on the AM technology.
5. After the machine is finished, the component can be removed from the build platform. The final product may need to undergo post processing, which might include removal of unprocessed material, additional manufacturing modifications, surface modification, removal of additional sacrificial support material, etc.

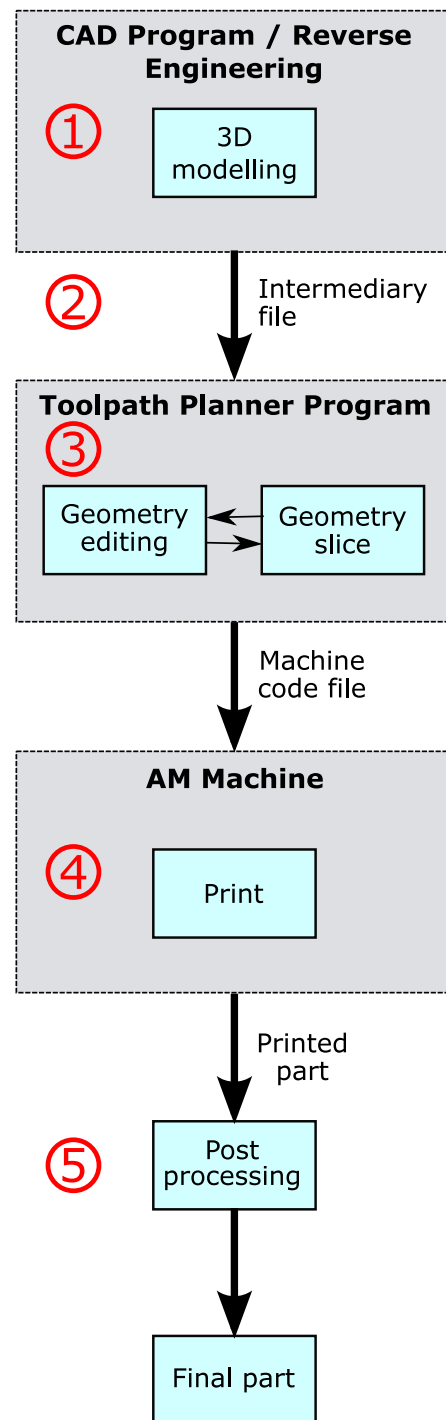


Figure 2.1: The conventional AM process flow. The process flow goes through the stages starting from a 3D digital model to a final product. The numbered stages correspond and are explained in detail Section 2.2.2. [Figure adapted from Ref [21]]



Figure 2.2: Two parts printed using FDM showing how the layers produce a step-like surface finish. The part on the left was printed with a 0.4 mm nozzle and the part on the right was printed with a 0.8 mm. The part on the left has a higher resolution and therefore has a less step-like finish. [Figure adapted from [www.3dwithus.com/3d-printer-nozzle-sizes-02mm-08mm-settings](http://www.3dwithus.com/3d-printer-nozzle-sizes-02mm-08mm-settings).]

### 2.2.3 Additive Manufacturing Comparison with Traditional Manufacturing

Traditional manufacturing starts with stock material then manufactures by subtracting, dividing, joining, or transforming (casting) the material until it is in a desired shape [30]. These are inherently different fabrication processes to AM. From this, AM offers three main benefits: (1) novel manufacturable geometries, (2) highly customised parts, and (3) local manufacturing business model.

Firstly, the AM process can manufacture novel geometries. These novel geometries are impossible to create without multiple separate components using traditional manufacturing methods [21]. In particular, complex architectures within parts are feasible with AM. Complex architectures could have customisable attributes such as lightweight and high SAVR properties.

The geometric limitations of AM are a subset of structural features such as overhanging features relative to the print direction, print orientation, and the build volume dimensions [31]. These challenges are unique to AM and need to be addressed with any print. Otherwise, the print may be either impossible due to dimensional constraints or cause the print to fail.

Secondly, the layer-by-layer fabrication allows considerable freedom for designers to customise not only based on geometric design but colour, material properties, mechanical properties, etc [32]. AM has the potential to only use material as needed to create parts almost exactly like a digital 3D model using supporting structures only as needed. Also, the different available materials can be tailored to the engineering specifications of the final part, such as mechanical properties.

The layered manufacturing approach also has disadvantages. The resolution can vary between the AM technologies. For example, laser technology depends

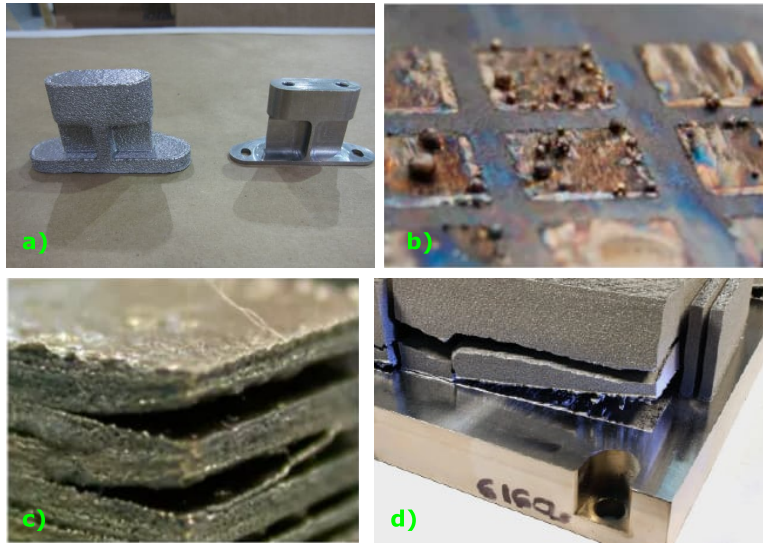


Figure 2.3: Examples of issues that can arise from AM: Figure a) shows surface roughness before any post-processing, b) shows melt balls from inconsistent melting, c) shows delamination between slice layers, and d) shows cracking from excess thermal stress. [Figure adapted from [www.engineering.com/story/7-issues-to-look-out-for-in-metal-3d-printing](http://www.engineering.com/story/7-issues-to-look-out-for-in-metal-3d-printing).]

on the galvanometric mirror drives and laser beam width, and fused deposition modelling (FDM), also known as fused filament fabrication (FFF), depends on the nozzle width. This may produce a step-like finish and surface roughness [31] as shown in Figure 2.2. Another issue is the material defects depending on the AM technology. For example, powder bed fusion (PBF) can have issues with residual thermal stress from the intense laser power and consistent melting issues [33,34]. Figure 2.3 shows examples of issues that can arise from AM including rough surface finish, inconsistent melting, layer delamination, and cracking.

Finally, there is an increased demand for innovative, customised, high-quality products at affordable competitive prices [8]. This promotes more of a localised business model rather than a globalised business model. AM offers a manufacturing process that uses fewer materials and fabrication stages. Local production using AM reduces the need for packaging, warehousing, and shipping [3]. This results in a leaner AM supply chain with simpler logistics, less overhead costs, and lead time [35]. An example of this model is the OpenFlexure Microscope project by Collins *et al.* [36]. The OpenFlexure microscope is a laboratory-grade microscope where the custom mechanical components are produced using FDM. The project focusses on decentralised production of microscopes as *in vitro* diagnostic devices in the Global South where supply chain disruptions are frequent [37]. Decentralised production, enabled by FDM, is especially beneficial for medical equipment in Sub-Saharan Africa as it provides not only local industry, but also increases the availability of local service engineers in an area where an estimated 70% of all medical equipment is out of service [38].

There are multiple prevailing challenges with integrating AM into industry. These drawbacks can result in high costs, production limitations, final product deficiencies, and design limitations. This makes AM more suitable for individual or low-volume production [6, 8, 32]. Depending on the AM technology it can be a costly investment to obtain the AM machine and feed materials, and it only becomes more economic as the geometry complexity increases [8]. There is also a need for AM-specific quality standardisation [39]. This ensures the final product quality, repeatability, and consistency within rapidly growing AM capabilities and competing financial interests from industries.

While AM has rapidly advanced with cutting-edge technology, the conventional process flow still relies on file formats from the 1980's, i.e. STL and GCode files [40]. This causes a disjoint in the digital portion of the process flow, as the original model needs to be re-approximated. The re-approximation can lead to loss of data from the original model, and a unidirectional flow of data [15]. However, CAM software generally does not translate between different AM technologies or even different AM machine companies. The universal file formats are to accommodate generalised CAD software and AM machine-specific CAM software [41].

As AM can create parts with different materials, mechanical properties, and geometries, this reaches a wider range of industries. Industries incorporating AM include electrical components, aerospace, and medicine [4].

### **2.2.4 Trending Industrial Applications of AM**

AM is a highly customisable manufacturing process that has impacted various industries. This section discusses AM development and progression in several major industries. See also Section 2.3.2 for industry specific applications of AM lattices.

#### **Electrical Components Industries**

Current conventional manufacturing processes involve using photolithography for producing electronic components. Photolithography is a very complicated, expensive, and chemically hazardous process [4]. Originally, 2D inkjet manufacturing was researched for single-layer electronic components, but now AM can fabricate complex multi-layered, multi-functional components [42]. AM is relatively low-cost, highly precise, and can use carbon-based feed materials such as ink containing carbon nanotubes or graphene [43–46]. Currently, there are two main routes of research for AM electrical components: carbon-based feed material and developing AM microtechnology.

Carbon-based feed materials are good candidates for making electrical components, such as batteries, solar panels, and supercapacitors, more powerful [47, 48]. For instance, AM lithium-ion batteries, commonly used for electronics and electric cars, initially had electrodes that lacked conducting additives, such as carbon-based additives. This significantly reduced battery performance [49–51]. Parts

with carbon-based feed materials are challenging to create since graphene and carbon nanotube molecules need to be in the correct orientation and maintain molecular structural integrity post manufacturing [52].

The AM technologies used to develop micro-scale electrical components are capable of manufacturing patterns  $<10\ \mu\text{m}$  thick [53,54]. The challenge is to manufacture components with micro-scale tolerances in a reliable and timely fashion. Current techniques have a trade-off between reproducibility, accuracy, and fabrication speed. Additionally, the machine nozzles can get clogged or contaminated from trace amounts of feed material sticking to the nozzle due to the high charge to mass ratio of trace droplets [4, 55]. As micro-scale fabrication requires high accuracy, mesh-based intermediary files can introduce geometric errors [56–60].

### **Mobility (Automotive and Aerospace) Industries**

The automotive and aerospace industries are constantly under pressure to improve performance and reduce weight [61]. AM allows these industries to move beyond traditional manufacturing constraints to design novel products for a wide variety of uses with intricate geometries and high strength materials [62]. The primary applications are manufacturing and repairing parts as well as the tools used to mass produce parts [63,64]. AM is now capable of manufacturing lithium-ion batteries for electric cars, miniature engines for unmanned aerial vehicles (UAVs), and even entire cars [61,65–69].

The materials for these industries must be lightweight and have high strength. Complex shapes using these materials, such as titanium (Ti) and nickel (Ni) alloys, are difficult to manufacture using conventional methods [70]. Metallic compounds, such as Ti and Ni, intermetallic compounds, such as Ti-Al, ceramics and carbon fibre reinforced plastics (CFRP) have shown good mechanical properties at high temperatures. This is due to their high strength, high stiffness and good creep, corrosion, and oxidation resistance [71–74]. This makes them suitable for a variety of parts, such as turbine blades in aeroplanes and car chassis [75–78]. Ceramics and composites are also researched to make parts, such as nozzles and thrusters for spacecraft [79,80]. One major issue is that multiple process parameters cause residual porosity and inhomogeneous microstructures, which greatly affect the mechanical properties of the finished part [71,81–83]. Some parameters include wire versus powder feed material, laser power, and the AM technology used [7,70,84]. Many of the AM technologies used operate under high heat, which can lead to thermal stresses, cracking, and distortion. Recently, cold metal transfer additive manufacturing (CMTAM), a newer type of gas metal arc welding AM process, is catching attention since it reduces thermal input, is spatter-free, and has high welding speed compared to traditional metal inert gas welding [85–87].

Designing parts that go beyond previous limitations, e.g. operating at temperatures beyond previous limits, can require exploring using new complex geometries. Many types of intricate geometries can only be manufactured using AM. As such, AM can create parts with high SAVR with intricate internal lattice structures. Some examples are compact heat exchangers to improve flow distri-

bution [88]. While AM enables intricate geometries to be made there is a limit to the complexity. An increase in sharp corners due to the low resolution mesh-based modelling is challenging for AM laser technologies. This is because the laser head must rotate tangential to the manufacturing path and cannot cover corners continuously [89]. The geometric inaccuracies can significantly affect the cost of the final component where seemingly insignificant amounts of material can make a significant impact in overall cost, especially for spacecrafts where components can cost over £10,000 per kilogram [90, 91].

## Medical Industries

Medical treatment is inherently challenging because every human body is unique, complex, and delicate. AM is able to create personalised implants, prostheses, and devices for direct use on the patient as well as for surgical planning and medical training [92, 93]. A number of large hospital centres now have their own AM laboratories to allow doctors to be directly involved [94]. This also forgoes the need of buying medical devices from external companies and having to wait for transportation. Regulations are still being formulated that can apply to individual hospitals. Having qualified teams of medical staff and engineers are vital to design and create medical components [94].

Because of AM, patients can have a range of personalised implants and prostheses. AM is able to create parts to fit the unique target area and mimic the original biological structure. This requires AM parts to have high accuracy. To fit these needs, different AM technologies can manufacture using various metal or polymer materials for bone, joint, or cartilage replacements and prostheses [95]. The accuracy levels can vary between different AM technologies as well as accuracy issues resulting from laser scanned images and the mesh-based file [96–98].

Another area of AM research is potentially using biomaterials as feed material. Biomaterials are synthetic or natural materials that interact with biological systems. Particularly, hydrogels are of interest since they mimic the 3D microenvironment of cells and are suitable scaffolding for live cells for tissue repair or for minimally invasive delivery of drugs, microelectric mechanical systems (MEMS), or other sensors [99–101]. The idea is to manufacture these hydrogel scaffolds with live cells either *ex vivo* or *in situ* to replicate grafts or biological structures, such as skin tissue [102]. Skin tissue has a complex 3D architecture consisting of different types of specialised proteins organised into different skin layers. Koch *et al.* investigated different AM techniques for skin tissue generation [103]. However, manufacturing tissue and organs is not a reality yet due to some challenging hurdles. Live cells are delicate and require stringent environmental conditions before use and need to be able to self-assemble into functional biological constructs post manufacturing [104].



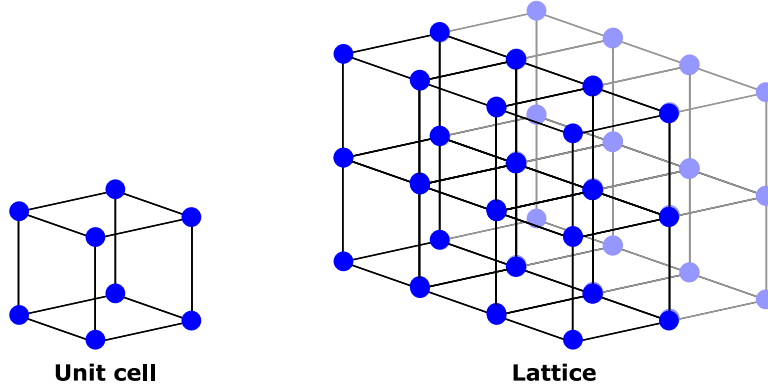


Figure 2.4: Primitive unit cell (simple cubic) and 3D lattice composed of multiple unit cells. The lattice was created by translating the unit cell in 3D.

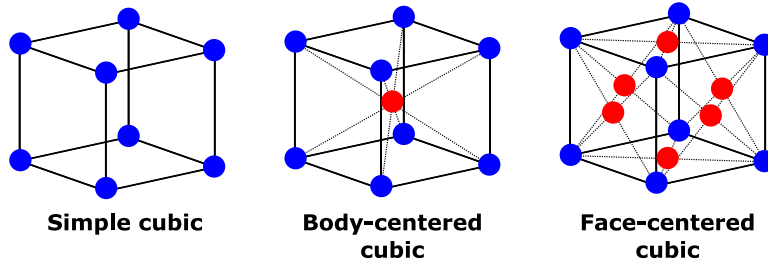


Figure 2.5: Simple cubic, body-centred cubic, and face-centred cubic lattice primitive unit cells. The different colours and line types are for visual purposes.

## 2.3 Additively Manufactured Lattices

### 2.3.1 Lattice Geometries

Lattices are a regular repeating pattern of arranged set of points, also known as a primitive lattice unit cell [105, 106]. The unit cell is the smallest volume that can reproduce the entire lattice. A 3D lattice is created by non-overlapping, translation (tiling) of the unit cell in 3D. Figure 2.4 shows an example of a 3D lattice created from translating a basis of a simple cubic lattice unit cell. There are many different types of lattices and cellular structures where cellular structures may not strictly adhere to the definition. Figure 2.5 show three different common lattice unit cells: simple cubic, body centred cubic, and face centred cubic. 3D lattices and cellular structures are ubiquitous throughout nature ranging from the atomic scale to visible macroscale. A few examples include: crystalline structures with a basis of atoms or molecules, soap films, inner bone matrices, butterfly wings, etc. [12].

### 2.3.2 Benefits of Manufacturing Lattices

Lattice structures have unique attributes such as high SAVR, lightweighting, and distinct subvolumes [10, 107–109]. This results in customisable multifunctional, highly specific properties (mechanical, thermal, acoustic, and electrical), as well

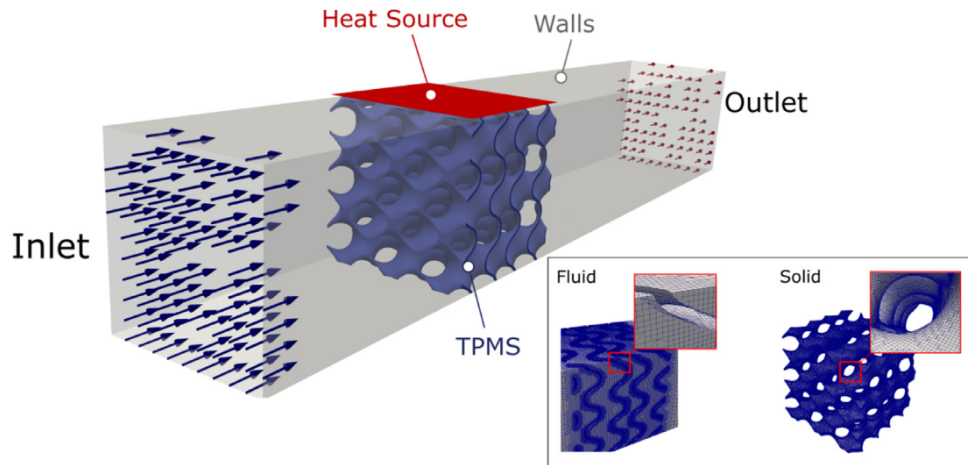


Figure 2.6: Model of a heat exchanger with a lattice design with distinct subvolumes. [Figure directly reproduced from Ref [110]].

as other benefits such as saving material cost. Hence, these properties make lattice structures attractive for engineering applications. AM has opened up the possibility of fabricating and customising lattice structures, where it was previously challenging or impossible to do so with traditional manufacturing processes.

### Addressing Global Trends

AM lattices have enhanced technology and innovation across multiple industries. Fluid transport and electrical component research has been augmented by incorporating AM lattices. The high surface area of lattice structures improves energy transport in heat exchangers [111]. Also, as many lattice types have distinct subvolumes, these separated labyrinths can contain different fluids. Attarzadeh *et al.* and Pelaconi *et al.* investigated the fluid and heat transport performance for heat exchangers using different AM lattices types, as shown in Figure 2.6 [110, 112]. AM lattices have also been developed for microfluidics. For example, Dudukovic *et al.* have created AM lattices using microstereolithography varying the outer structure and surface area [113]. Microfluidics and microreactors have the benefit of more controllability, safety, energy efficiency, and scalability [114]. Burns *et al.* investigated using AM lattices for filtration, optimising pore size to reduce pumping energy costs [115]. Lithium ion batteries with electrode lattices have improved performance. By increasing the surface area and decreasing diffusion path, this has improved the lithium ion transport [116]. There is also research into the lattice material and type to improve ion transport performance [117, 118].

Aerospace parts fabricated with AM lattice structures are lightweight whilst maintaining mechanical strength due to the high SAVR of lattices [9, 119]. Bühring *et al.* quantified how sandwich panels with a pyramidal lattice interior reduced weight and the mechanical limitations of AlSi10Mg [120]. Bici *et al.* designed a novel wing leading edge component with outer walls and inner lattice struc-

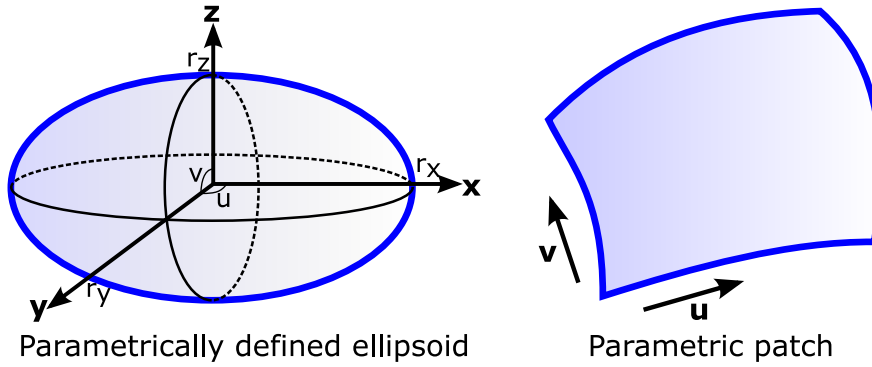


Figure 2.7: Shape boundaries defined by parametric functions. The left-side is an ellipsoid defined by parametric equations in terms of  $u$  and  $v$ . The right-side shows a quadrilateral parametric patch of a portion of a surface. [Figure adapted from [www.cs.princeton.edu/courses/archive/fall100/cs426/lectures/surfaces/sld006.htm](http://www.cs.princeton.edu/courses/archive/fall100/cs426/lectures/surfaces/sld006.htm)].

ture [119]. This was optimised for multiple parameters including weight, aerodynamic loads, and anti-ice properties. The other benefit to lightweighting is that it reduces the cost of material which increases the feasibility of using AM lattices. Khorasani *et al.* outlined the feasibility of fabricating parts via AM by modelling the cost analysis and concluded that AM was cost-effective for complex aerospace parts compared to CNC machining [121].

Biomedical research with AM lattices spans several areas, including medical implants and tissue regeneration. Medical implant lattice structures can have customised materials and lattice types based on the implant location in the body and function [122]. Biocompatible materials range from titanium alloys to thermoplastic polymers [123, 124]. The designed lattice type is based on engineering specifications such as mechanical properties. For example, Caiazzo *et al.* and Feng *et al.* investigated multiple lattice types and the resulting mechanical properties for biomedical use [125, 126]. Alternatively, the lattice structure could be customised based on the contouring of a prosthesis or the remodelling of human bone [127, 128]. Tissue regeneration also benefits from AM lattices as it can enhance healing by providing scaffolding for new tissue to grow between. Kovalcik *et al.* investigated biocompatible lattices that can be manufactured with FDM and its capabilities for tissue engineering by comparing the mechanical strength, weight, and proliferation of cell growth with PLA scaffolds [129]. Eltaher *et al.* created extrusion-based sacrificial sugar-protein lattices that naturally degrade as new tissue is generated [130].

### 2.3.3 Current Process for Additively Manufacturing Lattices

Currently, lattices can be designed in the CAM or CAD stage of the AM process flow. Traditional CAD software can create lattices by creating shapes based on

parametric modelling, as shown in Figure 2.7. This is done by defining boundaries as parametric functions [131]. Therefore simple geometries such as ellipsoids, polygons, etc. benefit from this type of modelling. When shapes are complex, piecewise-parametric patches are needed. As the number of patches increases, more computer resources are used [132–134].

Alternatively, in the CAM stage, lattices are designed as infill options present in commercial FDM CAM software. Infill is a built-in “filler” pattern, generally a type of lattice, that fills the “inside” volume of the imported 3D model. The purpose is to lightweight the shape, save on material and print time, and help prevent warping when the material shrinks after cooling. Infill usually comes with two types of customisation, infill type and infill density [11]. The lattice options are based on what is built into the software. Due to the limited customisation of infill and availability across AM technologies, infill is not generally used for modelling lattice structures engineered to a performance specification. Both process flows for creating AM lattices are shown in Figure 2.8.

### 2.3.4 Current Difficulties of Manufacturing Lattices

#### Lattice Design as Infill

The challenge with designing lattices as infill is lack of customisability, i.e. right-side of Figure 2.8. Whether infill is an option is dependent on the AM technology. This is a feature generally present in FDM CAM software but is generally not for other technologies, such as PBF or VAT photopolymerisation [135]. The infill type options depend on the CAM software. For example, currently Cura has fourteen infill patterns, PrusaSlicer has sixteen, and Simplify3D has six [136]. Not all infill patterns are lattices, some are concentric circles or concentric lines based on the exterior perimeter.

Customising infill lattices depends on options that the commercial CAM software provides, such as infill density [11, 137]. The options are generally very limited. Although infill is an efficient and streamlined method for creating AM lattices, it is currently limited by customisability [138]. Thus, this limits the capability of designing lattices to an engineering specification. Also, CAM software is not typically integrated with design tools, such as finite element analysis (FEA). As such, modelling AM lattices to a design specification is typically done in the CAD stage.

#### Lattice Design in CAD

Lattices are difficult to model in traditional CAD software using parametric modelling, i.e. left-side of Figure 2.8. As lattices can have high surface area, complex topology, and high curvature, this requires a large number of parametric patches to describe the surface. This causes issues with rendering and estimating complex topology without self-intersection problems [139].

Another challenge with this process flow occurs when transferring the virtual model into the CAM software. CAM software is often separate to the original

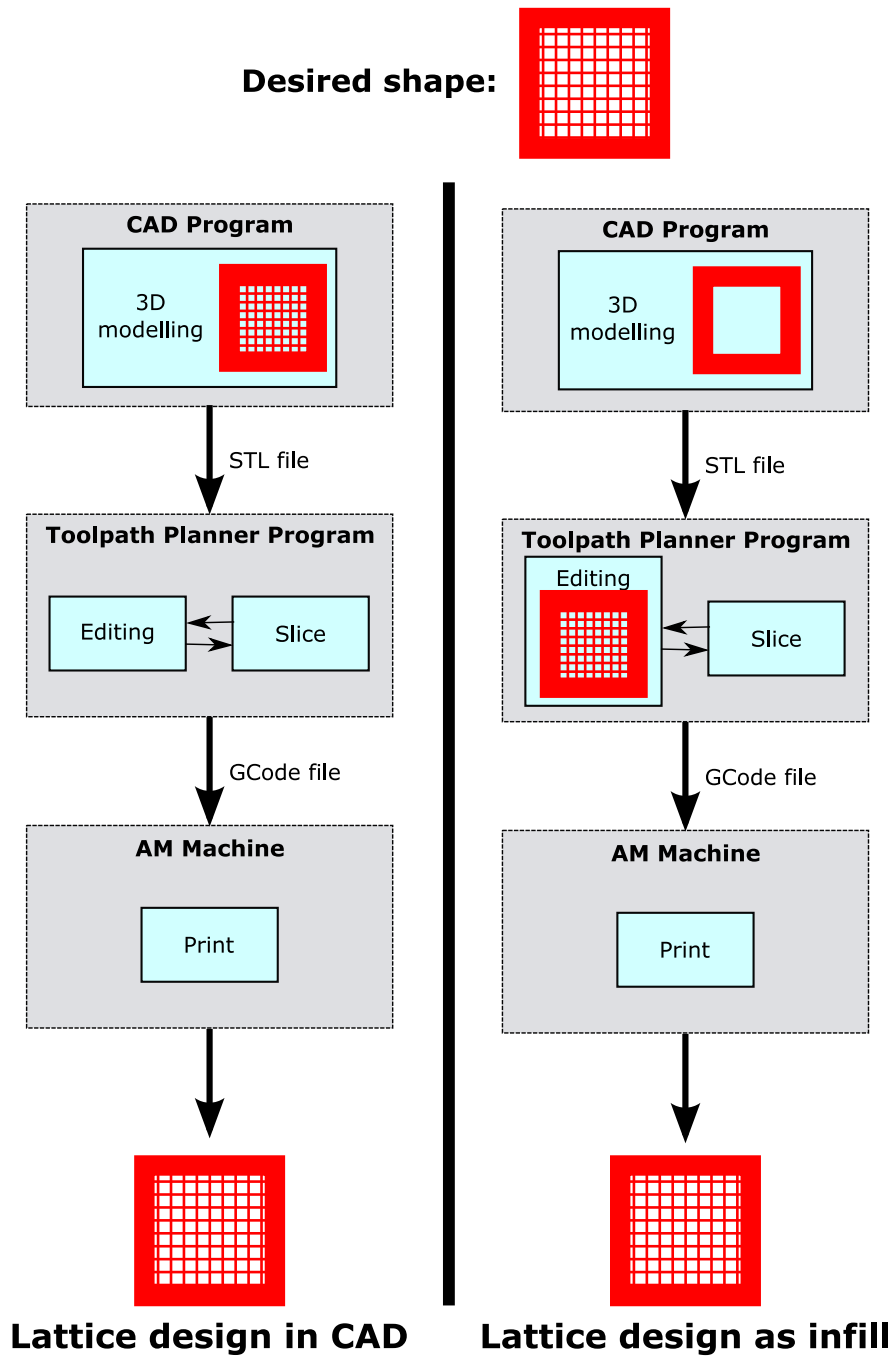


Figure 2.8: Two possible AM process flows for creating lattices. The left-side shows a flow where the lattice is created using the CAD software. The right-side shows a flow where the outer structure is created in CAD and the lattice is created later in the CAM software as infill.

CAD software and specific to the AM machine/technology. Therefore a generalised mesh-based intermediary file is used to transfer the virtual model, typically a STL file format [41,140]. The 3D CAD model translation to a mesh-based file can create tessellation problems such as missing facets, inconsistent facet ori-

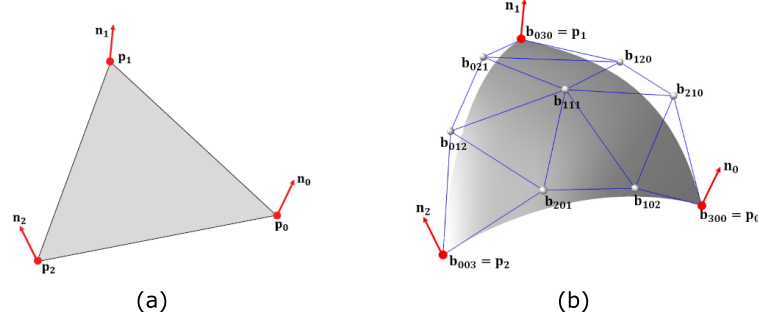


Figure 2.9: Planar triangular facet (a) versus a curved Bézier triangular facet (b). [Figure adapted from [143].]

entation, presence of internal walls and structures, and non-manifold topology conditions [17]. Because of these issues, correction algorithms or post processing software, such as Autodesk Netfabb, may be needed to repair the intermediary file before use [141, 142].

The triangular mesh-based modelling of STL files is best suited for flat polygonal models. Curved geometries are challenging to describe accurately without increasing the number of triangles as shown in Figure 2.10. The costly trade-off is as the number of triangles increases, the file size increases. Therefore, lattices with complex curved topology and high surface area are challenging to model with triangular meshes [16, 144–146]. There are methods to optimise the triangular mesh-based modelling. For example, adaptive tessellation for regions with high curvature or complexity helps reduce the file size [13, 140]. Other mesh-based file formats use non-planar facets, i.e. curved Bézier triangular facets [147]. Figure 2.9 shows the difference between a planar triangular facet and a curved triangular facet. There are other file formats created to resolve the STL file issues. A couple of common alternative file formats are the AMF and 3MF files. AMF is an XML-based format recognized by ASTM. It is similar to the STL file but it contains more information about the model, such as colour, texture, material, etc., and uses curved triangular facets [148, 149]. However, it is not an open format and the non-planar facets are more complex which antagonises the simplicity of a planar triangular mesh [14]. 3MF is an XML-based format created by Microsoft. Although it is industry-led, it is still an open format. It typically uses a planar triangle mesh like STL files and is more compact than AMF [150–152]. Like the AMF, it encodes information such as colour, material, and textures and is designed to be more compatible between CAD and CAM software [153]. However, these file format alternatives are still mesh-based file formats.

The multitude of issues arising from using mesh-based intermediary files poses the question of whether it is even necessary to use an intermediate file. The idea of bypassing an intermediate file altogether and directly passing CAD slices to the AM machine initially seems intuitive. Parts modelled with parametric patches have issues with rendering and estimating complex topology without self-intersection problems [139]. Thus, CAD model slicers are time consuming

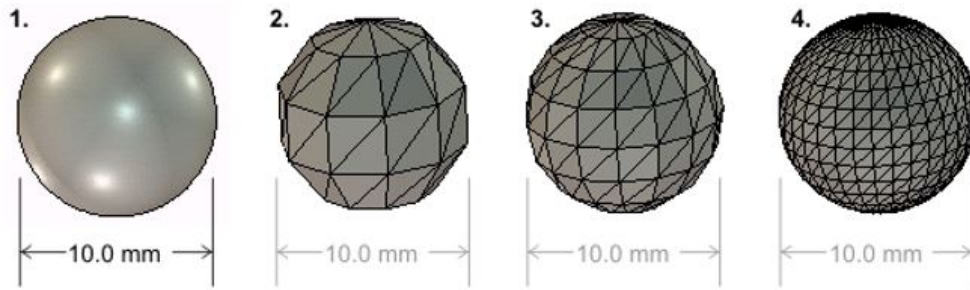


Figure 2.10: Shape (1) shows the surface to be estimated, then shapes (2), (3), and (4) show a triangular mesh estimation of (1) with increasing resolution. [Figure directly reproduced from [www.solidsolutions.co.uk/blog/2015/04/preparing-SOLIDWORKS-models-for-3d-printing](http://www.solidsolutions.co.uk/blog/2015/04/preparing-SOLIDWORKS-models-for-3d-printing).]

and computationally expensive as geometric complexity increases. There is research into using direct parametrically-based CAD slicers, such as using image processing for each slice, though it is still in early development and can only handle simple geometries [154].

## 2.4 Emerging Methods

### 2.4.1 Current Emerging Methods

As the field of AM lattices is rapidly expanding, simultaneously there is ongoing research to alleviate the challenges highlighted above. The following are current emerging methods to address these challenges.

#### 3MF File Format Lattice Extension

In 2015, the 3MF Consortium released a new lattice extension to their 3MF file format [155]. The new lattice extension represents cellular structures as a set of beam elements especially beneficial to parametric models [156, 157]. Then in late 2021, the 3MF Consortium announced a Volumetric Design extension where the 3MF file format describes shapes in the form of a mathematical, field-based description, i.e. implicit functions, rather than a mesh-based or NURBS estimation of the shape surface [158]. The mathematically defined volume can be used to specify properties such as colour and material, as well as blend multiple shapes together.

#### Implicit-Based Modelling

An implicit modelling environment, also known as functional-based representation (FRep), models surfaces based on implicit functions rather than parametric functions or patches. This is advantageous for modelling surfaces that can easily



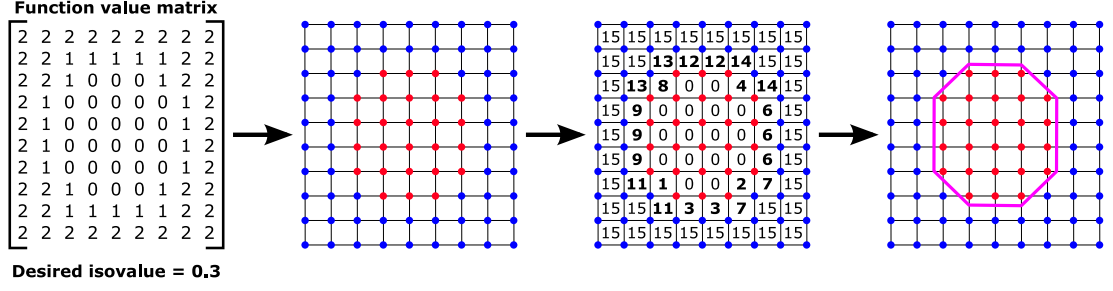


Figure 2.11: The general method for the 2D marching squares algorithm starts with an implicit function value matrix. This is calculated from a  $[x, y]$  grid and the surface implicit function. Then, each value in the matrix is evaluated whether it is above or below the desired isovalue. Each square is then assigned a number based on a look-up table [159]. The contour line is then traced.

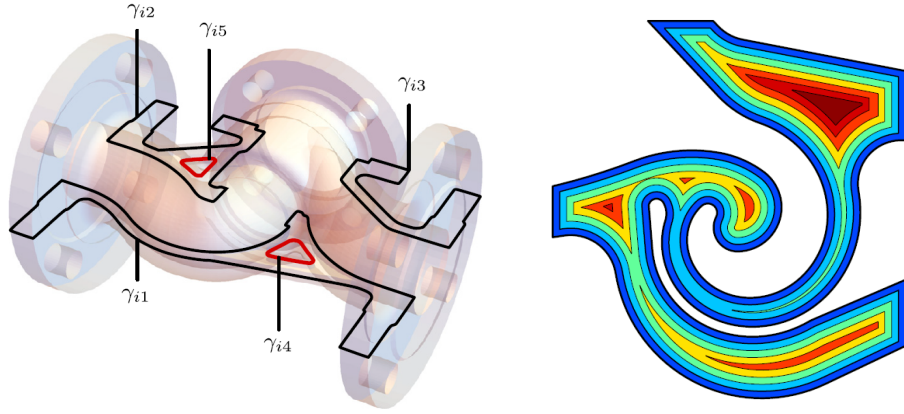


Figure 2.12: Implicit model showing slices at a particular  $z$ -height. The perimeter lines are directly sliced from the implicit function contour. The right-hand side diagram shows a slice with the perimeter toolpath based on the implicit function. The adjacent toolpath lines are based on offsetting by a constant distance [163]. [Figure directly reproduced from Ref [163]].

be described with implicit functions. Implicit functions are defined as

$$f(x, y, z) = c, \quad (2.1)$$

where  $f$  is a 3D function with coordinates in  $x, y, z$  and  $c$  is the constant isovalue. The surface exists when the isovalue evaluates to 0. The most common method to determine coordinates on the surface is to use a marching algorithm, such as marching squares or marching cubes, and the steps are shown in Figure 2.11 [159–161]. The method starts with a mesh of coordinates that are evaluated for the sign value using the implicit function. Then, based on a look-up table of each square, cube, or tetrahedron the surface contour can be traced. There are also variations to implementing marching algorithms, such as adaptive sampling [162].

Currently, there are developing methods using implicit modelling including methods to directly convert the implicit function contours into toolpaths, an



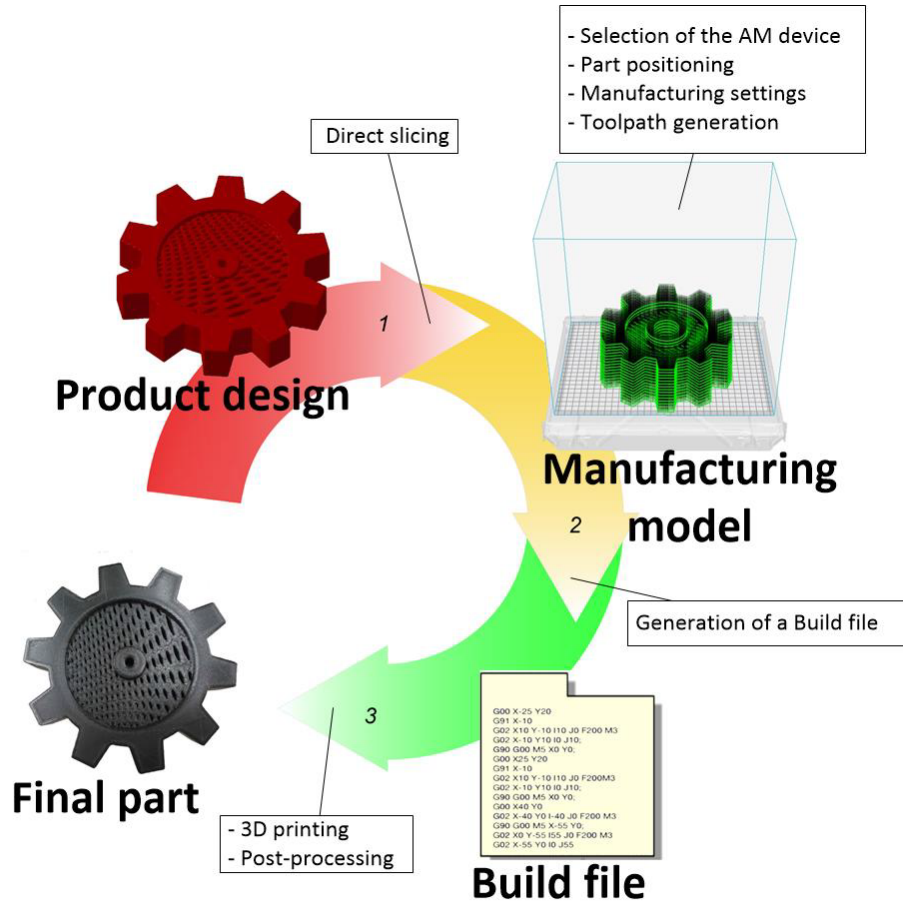


Figure 2.13: AM process flow where the designed model is directly sliced and prepared for the AM machine without the need for a mesh-based intermediary file.[Figure directly reproduced from Ref [19]].

example is shown in Figure 2.12. Using implicit functions to directly slice models bypasses the need for mesh-based modelling as shown in Figure 2.13. Popov *et al.* and Song *et al.* have developed adaptive methods to efficiently find implicit contours on each slice to be translated into toolpaths [19,162]. Steuben *et al.* has developed methods for creating multiple adjacent perimeter toolpaths based on implicit functions using Delauney Triangulation [163]. These groups and Adams *et al.* have also extensively investigated different infill patterns and lattices and their mechanical properties [164]. Zhang *et al.* have investigated multiple lattice infill types not present in commercial AM toolpath planner software. They developed methods to create the infill using implicit functions that resemble FDM infill [165].

### Commercial Software For Lattice Generation

There are multiple emerging commercial CAD software that focus on modelling lattice structures. Autodesk NetFabb, PTC Creo, Materialise 3-matic, Carbon

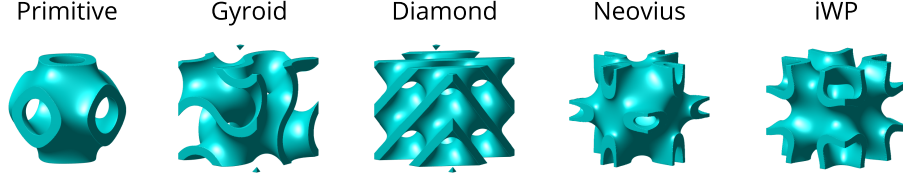


Figure 2.14: Examples of TPMS: Schwartz Primitive, Schoen Gyroid, Schwartz Diamond, Neovius, Schoen iWP.

Design Engine, Ansys SpaceClaim, and Siemens NX focus on generating lattice structures, mostly beam lattice types [142, 166–170]. These software offer methods to specify regions within a part to include lattices and have adjustable lattice parameters including thickness and cell size. Some also offer simulation of the lattice structure subjected to different mechanical loads [171]. Rhinoceros 3D estimates lattice surfaces using NURBS [172]. These software have plug-ins including General Lattice that can create many different types of lattice structures. Some examples of commercial CAD software that operate based on implicitly-based modelling are Gen3D and nTopology. Gen3D is capable of customised models by type, volume gradients, and multiple other adjustable parameters [173]. They also offer modelling specific to the design of hydraulic components. nTopology also offers customisable lattice types with the design freedom for advanced customisation including blending multiple lattice types. They also have topology optimisation based on built-in FEA tools [174]. While many of these software have advanced capabilities to model lattice structures, the issue is that most still rely on mesh-based intermediary files to transfer the structure to the CAM software.

### 2.4.2 Triply-Periodic Minimal Surfaces

The newly emerging methods have alleviated some issues with AM lattices, as well as opening up more possibilities for implicitly-defined structures. Of the implicitly-defined structures, there is a type of lattice called the triply-periodic minimal surface (TPMS). TPMS have been rapidly gaining attention in the AM community due to their unique properties.

#### Triply-Periodic Minimal Surface Definition

TPMS are a subclass of lattices. Figure 2.14 shows examples of five of these lattices, specifically the Schwartz Primitive, Schoen Gyroid, Schwartz Diamond, Neovius, Schoen iWP. These lattices have smooth continuous surfaces, high SAVR, and are defined by a single implicit function. They are minimal surfaces as they are mathematically defined as having zero mean curvature at each point on the surface. The mean curvature is defined as

$$H = \frac{k_1 + k_2}{2}, \quad (2.2)$$

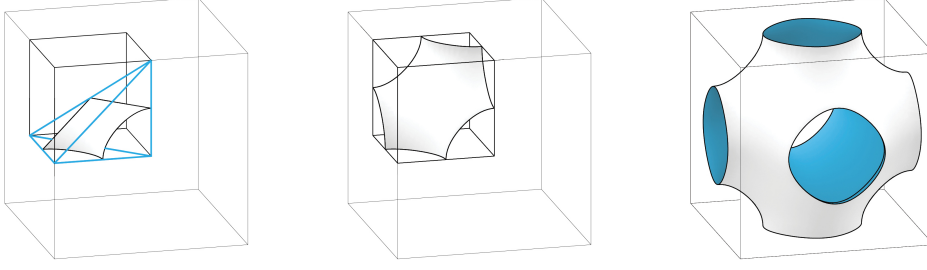


Figure 2.15: The fundamental patch (left-most diagram) for the TPMS Primitive is shown compared with one unit cell of the lattice (right-most diagram). The fundamental patch is a quadrilateral and a surface patch (centre diagram) is comprised of four fundamental patches. [Figure directly reproduced from [www.wewanttorearn.wordpress.com/2019/02/03/triply-periodic-minimal-surfaces/](http://www.wewanttorearn.wordpress.com/2019/02/03/triply-periodic-minimal-surfaces/).]

where  $H$  is the mean curvature and  $k_1$  and  $k_2$  are the orthogonal principal curvatures. As almost all TPMS are free of self-intersections and are considered embedded in  $\mathbb{R}^3$  in the real coordinate space. As such, the volume is divided into two disjoint subvolumes or labyrinths [175]. The TPMS implicit function values of the coordinates contained within the subvolumes either all evaluate negatively or positively. TPMS lattices are composed of fundamental patches, also referred to as primitive patches, where a fundamental patch is the smallest portion of the surface from which the entire surface can be constructed. Figure 2.15 shows the fundamental patch for the TPMS Primitive and Figure 2.16 shows how the patch constructs one lattice unit cell of the Primitive.

In the late 1800's, Schwartz and his student Neovius discovered the first TPMS Primitive and Neovius, respectively [176, 177]. Later in 1970, Schoen went on to discover another 12 TPMS including the popular Gyroid [178]. These discoveries were more “observational” via crystallographic structures without mathematical proof until Karcher formally proved them in 1989 [179]. Many more TPMS were then discovered via discrete differential geometry where most newer surfaces were conjugate surfaces [175]. The TPMS function is generally defined as

$$\phi(\mathbf{r}) = \sum_{l=1}^L \sum_{m=q}^M \mu_{ml} \cos(2\pi \kappa_l (\mathbf{P}_m^T \cdot \mathbf{r})) = 0 \quad (2.3)$$

where  $\kappa_l$  is a scale factor,  $\mu_{ml}$  is the periodic moment,  $\mathbf{P}_m$  is a basis vector, and  $\mathbf{r}$  is a location vector [180–182]. Some of the more simple TPMS functions can be expressed as the Enneper-Weierstrass representation, parameterising the coordinates as

$$x = \Re e^{i\theta} \int_{\omega_0}^{\omega} (1 - \tau^2) R(\tau) d\tau \quad (2.4)$$

$$y = \Re e^{i\theta} \int_{\omega_0}^{\omega} i(1 + \tau^2) R(\tau) d\tau \quad (2.5)$$

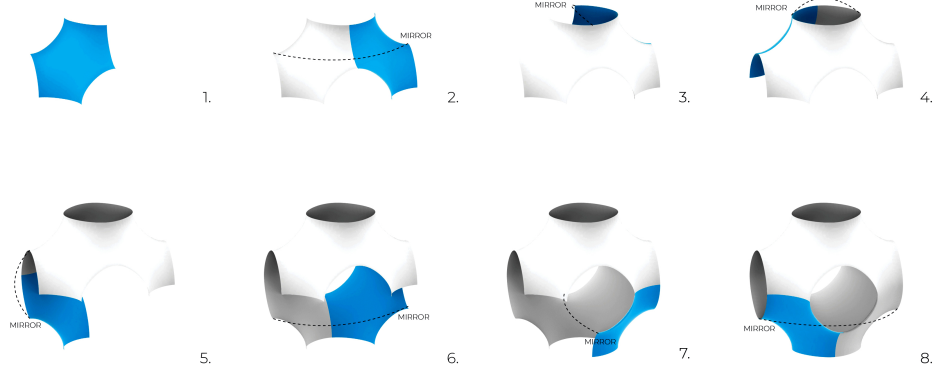


Figure 2.16: This shows how the Primitive lattice unit cell can be constructed with eight tiled surface patches. [Figure directly reproduced from [www.wewanttlearn.wordpress.com/2019/02/03/triply-periodic-minimal-surfaces/](http://www.wewanttlearn.wordpress.com/2019/02/03/triply-periodic-minimal-surfaces/).]

$$z = \Re e^{i\theta} \int_{\omega_0}^{\omega} 2\tau R(\tau) d\tau \quad (2.6)$$

where  $i$  is the imaginary number,  $R(\tau)$  is the Weierstrass function, and  $\theta$  is the Bonnet angle. The integrals are evaluated in  $\tau = \tau_a + ib$  the complex plane over a fixed point  $\omega_0$  to a variable point  $\omega$ . Although the Weierstrass function is known only for several TPMS, the benefit of the parametrisation is the precise coordinates of the surface and the fundamental patches may be solved analytically [183, 184]. This has been done for the Primitive, Gyroid, and Diamond by Gandy *et al.* [185–187].

These intriguing surfaces and similar topology are ubiquitous throughout nature. In ternary mixtures of water, oil, and surfactant, molecules self-assemble into TPMS in either inorganic or organic polymerisation found in mesoporous molecular sieves and contact lens materials [188, 189]. In biological systems, certain lipid bilayer membranes found in chloroplasts grown in light denied conditions, mitochondria, and other organelle found in eukaryotic cells can have complex structures that resemble TPMS [190–192]. This occurs with amphiphilic molecules arranging themselves in a 3D orientation such that the interfacial energy is minimised by the TPMS-like surface architecture and the hydrophobic and hydrophilic portions of the molecules are separated by the non-self intersecting subvolumes of the TPMS. Another example is the monocrystal magnesium calcite plates within the exoskeletons of echinoderms, i.e. sea urchins, sea stars, and sea cucumber [185, 193, 194].

### Triply-Periodic Minimal Surfaces in AM

TPMS are appealing to the AM community for multiple reasons due to their unique properties and resulting physical properties. There is rapidly growing

research to characterise the physical properties of TPMS structures, especially for mechanical testing.

As the structures have less mechanically “weak points” (e.g. corners) and are minimal surfaces, they are especially strong. Many research teams have performed experimental mechanical testing, varying a range of parameters including TPMS type, AM technology, and material [12]. Some examples include Al Ketan *et al.*, who conducted compression testing on various lattice structures, TPMS and non-TPMS [195]. They compared seven types of lattices of varying volume fractions fabricated from Maraging steel with PBF. They found that the TPMS with a sheet structure had overall superior mechanical properties. Liu *et al.*, Maskery *et al.*, Li *et al.*, Strömberg *et al.*, Afshar *et al.*, and Ma *et al.* all fabricated the TPMS structures functionally-graded lattice structures [181, 196–200]. This is where the lattice smoothly varied either in thickness, number of unit cells, lattice type, or location on the part, possibly optimised to mechanical testing characteristics. Other groups have performed experimental mechanical testing and/or finite element analysis (FEA) on TPMS structures fabricated with PBF as well as other AM technologies with various TPMS structures and volume fractions [10, 107, 125, 138, 181, 182, 200–220]. From various research teams, TPMS structures have been mechanically characterised for a broad spectrum of TPMS types, materials, AM technologies, and types of mechanical testing.

There has also been research testing other physical properties. Sankineni *et al.* fabricated several types of TPMS structures from PLA using FDM [208]. Each printed specimen had varying degrees of volume fraction as well as varying levels of structural manipulation in one axis. Each specimen was subjected to a fluid permeability experiment. In the experiment, each specimen was positioned at the bottom of a column filled with water. The sides of the specimens were wrapped in rubber and the flow rate of the water exiting the bottom-side of the specimens were measured. Other fluidic testing with TPMS structures with varying volume fractions was done with computational fluid dynamics (CFD) [201, 221, 222]. Yang *et al.* tested various TPMS structures fabricated by VAT photopolymerisation or stereolithography (SLA) with resin for their acoustic absorption capabilities [223]. They varied the volume fraction and the structures outer dimensions. Then, using the two-microphone impedance method, the sample is placed inside an impedance tube, with a sound source on one side of the tube, and microphones measuring the sound absorption on the other side [224]. Abueidda *et al.* and Dalaq *et al.* designed AM carbon-reinforced thin TPMS structures [215, 225–227]. The structures after fabrication, were reinforced in epoxy. They performed various experimental and simulation tests comparing different TPMS shape reinforcements. They tested FEA, heat transfer, and electrical conductivity. As TPMS have unique properties of high interest across many applications, these research teams have characterised varied TPMS structures for fluidics, heat transfer, electrical conductivity, and acoustics.

Alongside research on physical properties, there is also much interest in modelling and structural capabilities. Yoo *et al.* created novel Gyroid structures where the TPMS was altered to allow up to five different fluids to be separate [228].

Feng *et al.* designed toolpaths that can be directly translated to machine code for AM [229]. These use TPMS implicit functions and build toolpath lines surrounding the TPMS surface with a uniform wall thickness. There has also been research about creating hybrid TPMS structures. Hybrid structures are an amalgamation of a TPMS structure with another type of lattice structure, either TPMS or non-TPMS. This is done by using Euclidean set operators on the two functions to create a new shape. Ding *et al.* and Wang *et al.* have also created methods to convert TPMS surfaces to toolpaths with solid hatching infill on the “inside” of the structure [16, 230]. Both Chen *et al.* and Panesar *et al.* have various hybrid structures and performed finite element analysis (FEA) [107, 231]. Additionally, there has been other research on various algorithms for modelling TPMS structures and even an available research-focussed design program, FLatt Pack, from Maskery *et al.* [171, 232, 233]. FLatt Pack is a free, stand-alone lattice CAD software with twenty-three customisable lattices that can export in formats appropriate for AM, such as a STL file, and perform FEA. The lattice structures can be adjusted using the implicit function isovalue and the volume fraction input specification.

Due to their unique characteristics, TPMS are an attractive type of structure for AM. As AM affords geometric freedom and customised materials, the AM TPMS research that spans across modelling capabilities, novel optimised structures, AM technologies and materials, and experimental physical properties is rapidly expanding.

### 2.4.3 Unresolved Challenges

Although there are exciting emerging methods and research for AM lattice structures, particularly for TPMS, there are unresolved challenges. These challenges are gaps in the literature and occur at certain stages within the AM process flow that create bottlenecks hindering AM capability.

The first unresolved challenge is modelling TPMS structures to a geometric design specification. As TPMS are infinitely thin surfaces, volume needs to be added so that they create feasibly manufacturable structures. There are different methods used by various research groups to add volume to TPMS structures as this is not a straightforward process. One method is to set the implicit function to different isovalues and then designate a subvolume as solid material. The other method is to start with the TPMS contour lines and uniformly thicken the structure or only change the number of lattice unit cells similar to infill density. Of the papers reviewed for experimental mechanical testing, approximately 60% used the isovalue method [10, 181, 182, 195–198, 200, 202, 203, 205, 208–210, 212, 214], 30% used uniform thickness method [125, 138, 201, 204, 206, 215, 216], and 10% did not explicitly state which method they used [207, 211, 213].

As there are two different methods, there are discrepancies in the structures they create. TPMS implicit functions set to varying isovalues does not change the local position on the surface isotropically [10]. Thus, when isovalues are used for modelling structures, these structures do not have a uniform thickness. Therefore,

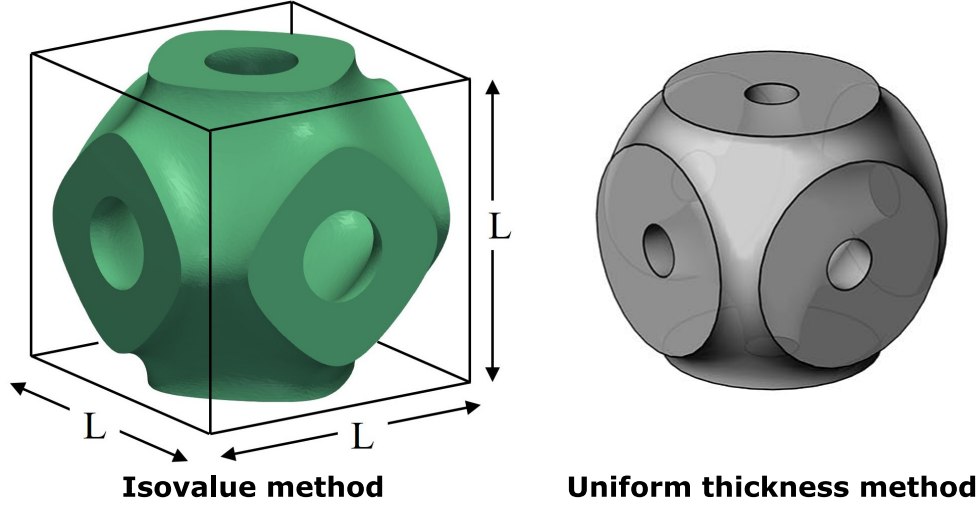


Figure 2.17: Two methods for adding volume to TPMS structures for a single lattice unit cell. The left-side shows the isovalue method where two implicit functions are set to two different isovalues and the subvolume between is considered the solid structure. The right-side shows the uniform thickness method where the TPMS is uniformly thickened from the TPMS implicit function. [Figure directly reproduced from Refs [233,234]].

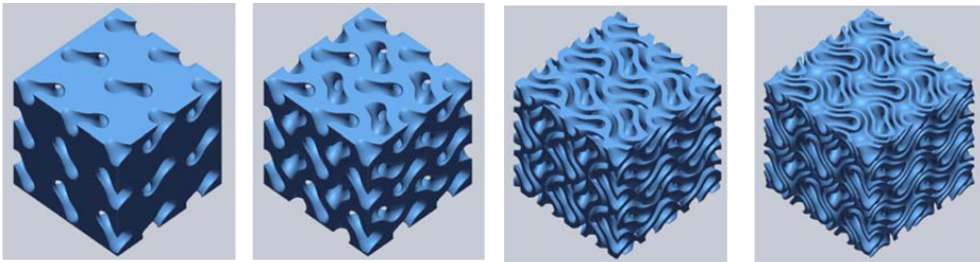


Figure 2.18: TPMS structures created from multiple isovalues. Increasing the number of isovalues, increases the number of distinct pore networks or subvolumes. [Figure modified from Ref [228]]



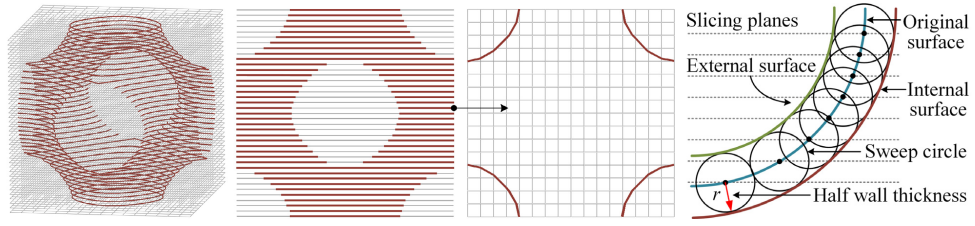


Figure 2.19: Feng *et al.* method for obtaining the implicit function contours. The contours are used to outwardly calculate adjacent toolpath lines that are uniformly thick [229]. [Figure directly reproduced from [229]].

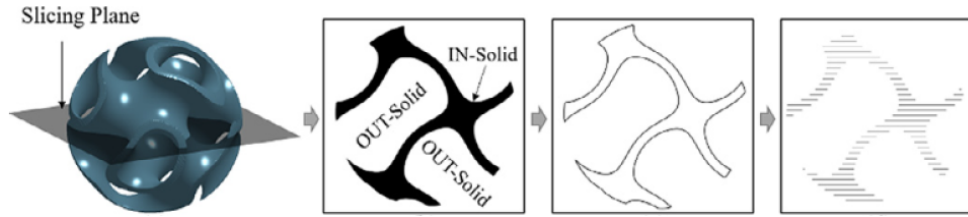


Figure 2.20: Ding *et al.* method for creating the solid hatching toolpath for slices at a particular z-height from an implicit model. The contour of the TPMS is calculated then using boolean operations with solid hatching lines the hatched lines are cut out into the TPMS shape [16]. [Figure directly reproduced from [16]].

the different methods create different structures even when the structures have the same volume fraction, as shown in Figure 2.17.

The method using isovalues to model TPMS structures is a controlled method for adding volume when using implicit-based modelling. This is also a controlled method for creating TPMS structures with multiple layers and distinct pore networks, i.e. subvolumes, as shown in Figure 2.18 [228]. Even though the majority of the reviewed papers use this method, the issue is that the link between isovalues and the geometrical properties is not intuitive. Some research groups resort to using multiple modelling software just to create a TPMS structure to a geometric specification [207, 223, 225, 228]. There are a few regression models relating isovalues to geometric properties [196, 198, 203, 219, 220]. However, there is limited information regarding the calculation and the associated residuals, as well as discrepancies between each other. These discrepancies also show the difficulty in modelling TPMS structures as it is an unresolved challenge.

The second unresolved challenge is that there are limited alternatives to completely avoid mesh-based modelling in the AM process flow. This is especially true for modelling TPMS structures for a design specification. While there are emerging research and commercial software that specialise in modelling lattice structures, many still primarily export models in a mesh-based intermediary file format to the CAM software [142, 169, 170, 172]. Some companies such as nTopology and Gen3D, can export lattices using the 3mf lattice extensions [173, 174]. However, currently only a few CAM software, such as Materialise Magics, are compatible with the new lattice extensions [235].



Direct slicing of implicit-based models bypasses the need for intermediary file formats. As implicit functions form contour lines at different isovalues, these lines can be directly used to create toolpath lines as shown in the literature [19, 162–165]. This method is beneficial for creating toolpaths for TPMS structures. Feng *et al.* has created toolpaths for TPMS structures using contour lines. From a contour line, equidistant adjacent toolpaths are then calculated, as shown in Figure 2.19 [229]. This creates a TPMS structure with uniform thickness. However, there are limited possibilities for creating structures with multiple isovalues or to a geometric design specification. With this method, if there are multiple isovalues present, this may cause issues when equidistant adjacent toolpaths interface seeding from different contour lines. Ding *et al.* and Wang *et al.* also have methods to create toolpaths from TPMS contour lines [16, 230]. They use isovalues to specify the outer structure of the TPMS lattice, then, using Euclidean set operators create solid hatching toolpaths “inside” of the TPMS structure as shown in Figure 2.20. Feng *et al.* and Ding *et al.* manufactured their work by exporting the slices as common line interface (CLI) files. CLI files describe models in 2D slices rather than a 3D solid structure [236]. Some companies, such as nTopology and PTC Creo, are also capable of exporting CLI files [166, 174]. Selective CAM software are able to import this format and translate the slices into machine code for a AM machine.

While there are direct slicing capabilities, this area of research can be expanded. Currently there is limited capability to input any geometrical specification to tailor TPMS structure and their toolpaths. Also, there are limited toolpath options beyond solid hatching using the isovalue method.

These unresolved challenges are gaps within the literature. These challenges limit the capabilities of AM lattices, specifically TPMS structures. Addressing the challenges of TPMS modelling and mesh-based modelling formulates the aim, objectives, and scope of this thesis.

# Chapter 3

## Research Aim, Objectives, and Scope

### 3.1 Introduction

Surveys of the literature resulted in the formulation of the vision for this thesis. From the literature, current AM process flows limit the capability of creating AM lattices, particularly for TPMS shapes. From this, the vision of this thesis is to create an alternative method for fabricating customised AM lattices. Though there are countless ways to approach this problem, this thesis will focus on using implicitly-defined geometries, thereby reworking the AM process flow. This chapter outlines the aim and objectives of this thesis and the resulting research contributions. Additionally, this chapter defines the scope of this research by establishing a set of guidelines. The scope of this research sets clear boundaries with respect to the representative geometries tested, CAM program development, feed material, and AM technologies used.

### 3.2 Aim, Objectives, and Contributions

#### 3.2.1 Research Aim

The aim of this research is to create methods in an alternative AM process flow for customised TPMS structures that address the gaps identified in the literature. From this, individual methods within the process flow will be developed such that they can be adapted into different types of process flows and software packages. As such, this process flow and methods will reach a wide range of designers. As the literature review from the previous chapter has highlighted, there is a need for a streamlined, efficient process.

There are two major gaps noted: (1) difficulties in creating AM TPMS structures with customised geometric properties and (2) limited alternative methods to produce customised TPMS structures that avoid mesh-based modelling. Currently, specialised CAD software or considerable mathematical and program-

ming skills are required to model TPMS structures. Even so, the process is not straightforward leading to diverging methods and structures. By establishing empirical geometric relationships, this consolidates methods for modelling TPMS structures and promotes the wider incorporation of TPMS into CAD products. From this, creating a CAM program with direct slicing methods to translate implicitly-defined geometry into toolpaths for an AM machine avoids the need for mesh-based modelling. As such, the methods employed by this program could be adapted into commercial CAM platforms as infill to be utilised beyond its current scope. Furthermore, this process flow and methods can aid in predicting desirable specific properties, such as mechanical properties, of the final part from the initial mathematical implicit functions.

### 3.2.2 Research Objectives

The envisaged benefits of this process flow are to consolidate, streamline, and greatly reduce the dependency on mesh-based modelling. This thereby improves accuracy and efficiency when modelling TPMS structures. To be clear, while the aim is to create a fully operable alternative process flow, it is an equally important that the individual methods are easily adaptable into different platforms and technologies. To achieve this aim, the following research objectives have been outlined:

1. A set of numerical methods for calculating geometric properties to a clear accuracy tolerance will be established. This generalised set of numerical methods will be used across multiple TPMS structures with varying implicit function isovalues. The calculated geometric properties are volume fraction, surface area, and minimum thickness. The set will be formulated by investigating and comparing different numerical methods with the criteria of reproducibility, accuracy, and computational efficiency.
2. Empirical relationships between the TPMS isovalues and the geometric properties based on (1) will be established. To do this, datasets will be calculated for each case of TPMS structure type and geometric property using the set of numerical methods with a clear accuracy tolerance. Then polynomial fitting models for the datasets will be generated. These models are the empirical relationships designers can use to model TPMS structures to geometrical specification.
3. Once the empirical relationships from (2) are calculated, the TPMS can be customised for a geometric specification. A CAM program will be developed to directly slice shapes defined by implicit functions. Within each slice, the toolpath algorithm will calculate toolpath lines based on implicit function contour lines to generate machine code for the AM machine.
4. The direct slicing method will be expanded for geometrically customise TPMS structures by using the relationships from (2). Additionally, the

relationships will also be used to calculate adjacent toolpath lines based on the TPMS implicit functions.

5. Geometrically customised TPMS structures will be related to engineering properties, such as mechanical properties, using the previous objects. This will be done by experimentally testing the volume measurements and compressive properties of printed TPMS structures with varying volume fractions. While this shows how to establish further relationships with other engineering properties, it also assesses the current status of the toolpath algorithm and application predictability.

### 3.2.3 Research Contributions

The research in this thesis was performed following these objectives. The research successfully fulfilled the research aim. This resulted in the following research contributions:

- A set of numerical methods were established to reliably calculate the volume fraction, surface area, and minimum thickness for TPMS structures created with varying isovalues. Multiple numerical techniques were trialled before a set was established based on criteria of reproducibility, accuracy, and computational efficiency.
- Empirical relationships between the isovalue and geometric properties were established for five TPMS structures. Datasets created using the numerical methods were fit using robust Chebyshev polynomials to a clear accuracy tolerance. The coefficients in a standard polynomial format are available for five TPMS structures for the single and double surface cases. These polynomial relationships are useful as they allow designers to controllably model TPMS structures to design specification by adjusting the TPMS isovalue. While other research teams have calculated geometric properties, this research contributes robust relationships with known tolerances that can be used as is or integrated into the back-end of CAD packages.
- A direct slicing toolpath algorithm was developed that creates GCode for customised TPMS structures based on input geometric property specification. The algorithm adaptively calculates toolpaths based on the contour lines using on the geometric relationships. While other direct slicing methods have been developed by other research groups to create machine code for TPMS, this research can create GCode for geometrically customised TPMS structures. This not only provides developers a deterministic method for manufacturing customised TPMS but also provides a method to relate and tune TPMS structures for an engineering application. Compressive testing was performed on printed Gyroid specimens showed Young's modulus relating to the volume fraction using the Gibson-Ashby relationship. The experiments showed strong preliminary results, with future work identified to close discrepancies.

### 3.3 Research Scope and Boundaries

The research framework will be conducted in three phases: the geometric property calculation phase in Chapter 5, the toolpath algorithm development phase in Chapter 6, and the experimental phase in Chapter 7.

#### 3.3.1 Geometric Property Calculation Phase

During the geometric property calculation phase, the geometric relationships between TPMS isovalues and geometric properties will be established. This will be done for five TPMS: Primitive, Gyroid, Diamond, Neovius, and iWP. These five were chosen as they are commonly researched throughout the literature for AM. For each TPMS the single surface and double surface structures will be considered, where single surface structure are created using one isovalue and double surface structures with two different isovalues. The geometric properties that will be calculated are volume fraction, surface area, and minimum thickness. These properties are the basis to many advanced engineering properties. Minimum thickness will also help designers assess if the model is feasible based on the AM technology resolution. To calculate these geometric properties, a formulated set of numerical methods will be established. From this set, datasets will be calculated for each case of TPMS structure type and geometric property. Then polynomial models will be fit to the datasets, establishing geometric relationships. These relationships will allow designers to controllably customise TPMS to design specification.

#### 3.3.2 Toolpath Algorithm Development Phase

During this phase, a direct slicing toolpath algorithm will be developed to fabricate geometrically customised TPMS structures where the toolpaths are adaptively calculated using the TPMS function. Based on this algorithm, a CAM program will be created to generate machine code, i.e. GCode, from TPMS implicit functions. Prior to the development of the program, preliminary investigations of open-source CAM software will establish the current status of existing algorithms, capabilities, and limitations of TPMS infill. Then a direct slicing CAM program will be developed to generate toolpaths from TPMS implicit contours. From this, the algorithm will be expanded to create geometrically customised TPMS structures using the geometric relationships. This CAM program will allow users to input geometric specifications, TPMS structure type, and other print setting and output machine code ready for an AM machine. This will result in the alternative flow to create geometrically customised TPMS lattices without mesh-based modelling.

### 3.3.3 Experimental Phase

During the experimental phase, testing will build relationships to create TPMS structures tunable for further engineering properties, specifically focussing on compressive mechanical properties. This builds on the previous phase by extending the customisation capabilities of TPMS structures that are directly applicable to designers. The experiments will be carried out as volume measurement tests and compressive mechanical tests. These tests will be performed on TPMS structures with varying volume fractions. Thereby showing how volume fraction and compressive mechanical properties relate. Also, these tests will quantify the effect of imperfections of the toolpath calculation by comparing with theoretical mechanical properties. Therefore, this not only builds further relationships but also quantifies the current status of the alternative process flow and identifies possibilities for future optimisation beyond this thesis.

### 3.3.4 Research Boundaries

This thesis has set clear boundaries for each of the three phases. In the geometric property calculation phase, it is important to consider geometries that push the limits of conventional methods. As TPMS push these limits due to their unique characteristics, the following five TPMS will be the only geometries considered in this thesis: Primitive, Gyroid, Diamond, Neovius, and iWP. The only structure types that will be considered are single and double surface structures. The only geometric properties that will be considered are volume fraction, surface area, and minimum thickness. As the set of numerical methods for calculating geometric properties will be generalised for multiple TPMS, future work beyond this research can use these methods to characterise other TPMS.

In the toolpath algorithm phase, as the breadth of AM spans many different technologies and materials, clear boundaries need to be established. In this thesis, only FDM using plastic feed materials will be considered. Specifically, the Prusa i3 MK3+ AM machine with PLA filament. The direct slicing toolpath algorithm and CAM program development will focus only on developing novel methods and algorithms. The program will focus only on the TPMS structure types and geometric customisation from the previous phase. As the program will only be a pre-alpha prototype, the lattice will be kept to a basic outer structure of a cube and the only adjustable scaling parameters are the cube dimensions and number of lattice unit cells.

In the experimental phase, there are various plausible use cases for experimental testing. Only compression mechanical testing will be performed as there are already established relationships between cellular volume fraction and compressive mechanical properties. As the established relationships are proportional to volume fraction, that will be the only variable for the test specimens. This then limits the only needed geometric testing to volume measurements. Thus, the TPMS type, number of lattice unit cells, feed material, AM technology and

brand, and program version will remain constant. By limiting the number of variables, unwanted variable dependencies in the test data will be kept to a minimum.

# Chapter 4

## Research Methodology and Framework

### 4.1 Research Context

This PhD research will create an AM process flow based on functional-based modelling whose accuracy is not simply a function of the mesh resolution, specifically focussing on TPMS. This is outlined in Chapter 3 to address the gaps in literature identified in Section 2.4.3. This alternative process flow will address the identified gaps. The first gap is the inconsistencies in modelling geometrically customised TPMS structures. As surface equations define infinitely thin surfaces, the surfaces need to be volumised to become feasible for AM. Volumising TPMS to geometric specification is not straightforward, thus leading to diverging methods and structures. The second gap is the limited alternative methods to produce customised TPMS structures that avoid mesh-based modelling. As lattice structures can have high SAVR, complex topology, and high curvature, using mesh-based modelling has a costly trade-off of resolution accuracy and computational efficiency, as well as other mesh-based issues. Therefore, mesh-based modelling creates bottlenecks in the AM process flow for AM lattices. In the conventional AM process flow, these bottlenecks occur at the CAD stage with parametric modelling and at the intermediary file stage with triangular mesh modelling, as shown by Figure 4.1.

**Bottlenecks in AM flow for customised lattices**

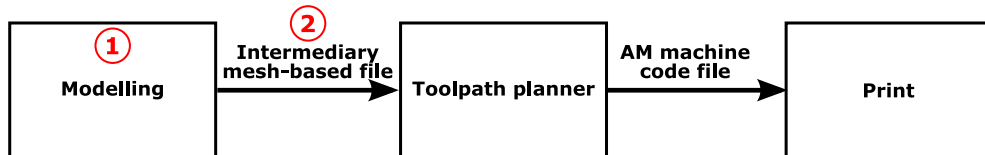


Figure 4.1: Diagram highlighting where the identified mesh-based modelling bottlenecks in the conventional AM process flow for AM lattices (numbered red text). These bottlenecks occur at the CAD stage with parametric modelling (1) and at the intermediary file stage with triangular mesh modelling (2).



## 4.2 Research Framework

The research framework of this thesis is based on an implicit-modelling approach. The framework is conducted in the three phases defined in Chapter 3, shown in Figure 4.2. The phases are the geometric property calculation phase, the toolpath algorithm development phase, and the experimental phase. During the geometric property calculation phase, geometric relationships between TPMS isovalues and geometric properties will be established. Next in the toolpath algorithm development phase, direct slicing toolpath algorithms are developed using the geometric relationships from the prior phase. Then the experimental phase uses the developments from the previous two phases to print geometrically customised TPMS structures and experimentally test for volume measurements and compressive mechanical properties.

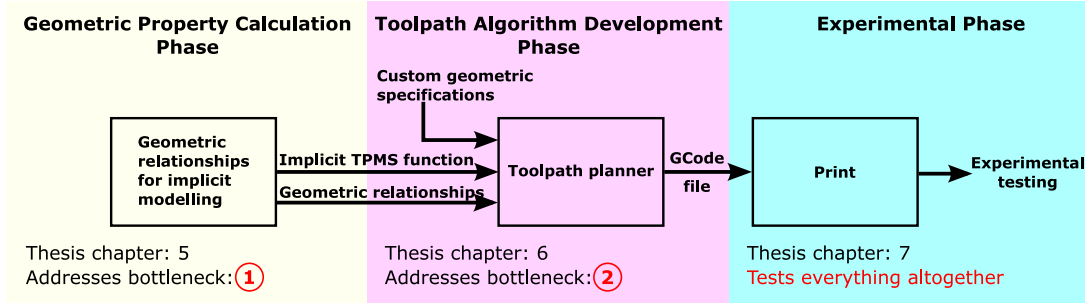


Figure 4.2: Diagram showing the research framework for this thesis. The framework is conducted in three phases essentially following the progression of the AM process flow. Each phase in the diagram shows the process flow progression, the corresponding thesis chapter, and the mesh-based modelling bottleneck addressed from Figure 4.1.

## 4.3 Research Methodology

The gaps in the literature highlight the difficulties in creating customised AM TPMS structures. By creating an alternative process flow, this will query whether implicit-based meshless methods increase the feasibility of AM TPMS structures. Within this process flow, implicit modelling methods will be employed to address each gap. The order of developing this process flow will follow the progression of the AM process flow. Thus, as this flow is developed, from establishing relationships for modelling through experimental testing of printed specimens, subsequent developments will validate prior developments.

### 4.3.1 Implicit Modelling Methods

Implicit modelling is becoming increasingly prevalent due to modern computing. The GPU processing of modern computing makes rendering implicit models more

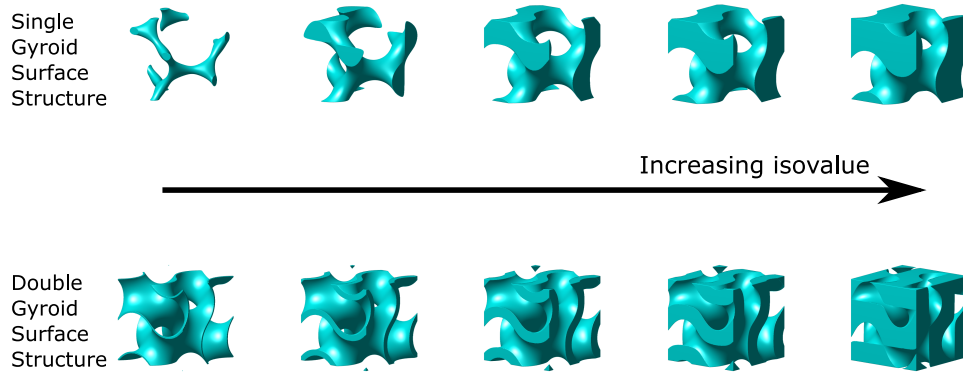


Figure 4.3: Diagram depicting how the volume of TPMS Gyroid single and double surface structures change with varying isovalues.

efficient [18,139,237]. As such, this is becoming an increasingly popular framework for modelling lattice geometries. As lattices can have high SAVR, complex topology, and high curvature properties, they become computationally challenging to model accurately using mesh-based modelling. Therefore, modelling lattices using implicit functions is computationally efficient compared to mesh-based modelling.

One benefit of using implicit modelling is lattice structures can be spatially varied, smoothly, via manipulation of the underlying implicit function. This is an important feature of implicit modelling as implicit functions define infinitely thin surfaces. As such, the implicit functions can be manipulated, such as via the isovalue, to add volume into a lattice structure to make them feasible for AM.

Particularly, TPMS are a type of lattice that are mathematically defined with by a single implicit function. Their unique properties make them attractive for engineering applications. Using implicit modelling, the structure volume can be customised by setting the implicit function to different isovalues. Also, different types of structures can be created by setting the implicit function to a different number of isovalues. Figure 4.3 shows two different types of Gyroid structures: set to one isovalue, i.e. “single surface structure” or also referred to as “solid structure”, and set to two isovalues, i.e. “double surface structure” also referred to “sheet structure”. The figure also shows how the structure volume can be controlled by varying the isovalue.

Another benefit of implicit modelling is easily identifying the distinct subvolumes by evaluating the TPMS implicit function for Euclidean coordinates within the system volume. Coordinates on the surface will evaluate to zero and distinct subvolumes will evaluate to values with opposite signs. Designers can use the subvolumes to designate the solid printed material and free space or even a second material. Figures 4.4 and 4.5 show the subvolumes of a TPMS Primitive structure from a 2D and 3D perspective respectively.

Additionally, in a 2D slice, implicit functions set at different isovalues create contour lines, also known as isolines. As AM machines need printing instructions in the form of lines, the contour lines can be directly translated into toolpaths.

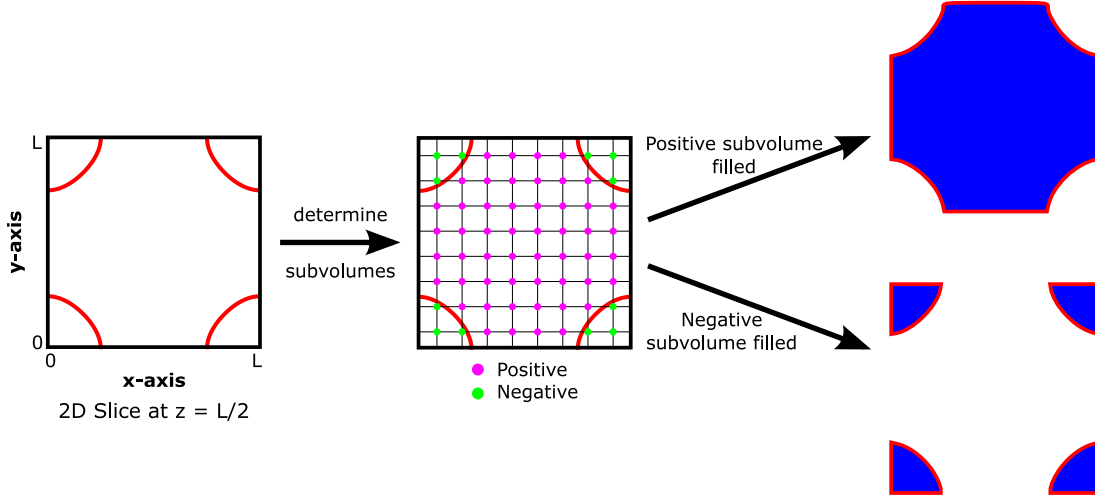


Figure 4.4: 2D slice of a single unit cell of Primitive at  $z = \frac{L}{2}$  (red lines), where  $L$  is the length of the unit cell. This shows how coordinates within the unit cell volume can be categorised into subvolume depending on what sign the function evaluates to. A particular subvolume can be considered the solid printed material based on the designers choice.

Commercial FDM CAM software use contour lines from explicit functions to create infill structures. Thus, once the TPMS implicit functions have been manipulated to achieve a geometric specification, the implicit functions can be directly translated into toolpaths for the AM machine.

As recent advancements in computing power has made implicit rendering more efficient, it is now possible for AM to reap the benefit of implicit modelling [18, 139, 237]. Using implicit modelling methods throughout the AM process flow avoids the mesh-based modelling bottlenecks. From this, the implicit functions can be used to controllably geometrically customise TPMS structures. The following is the methodology of this thesis for implementing implicit modelling methods into an AM process flow.

### 4.3.2 Geometric Property Calculation Phase

During the geometric property calculation phase, relationships between the TPMS implicit function isovalues and geometric properties will be established. As many physical properties are based on elementary geometric properties, the geometric properties need to be controllable to design structures to an engineering specification. While manipulating the isovalue is a controllable method for adjusting the structure volume, the relationship between the isovalue and geometric properties of the structure is not intuitive. This limits their use to highly specialised communities. This phase addresses the first gap from the literature review and helps avoid the mesh-based modelling bottleneck arising from traditional CAD software. The work of this phase is covered in Chapter 5.

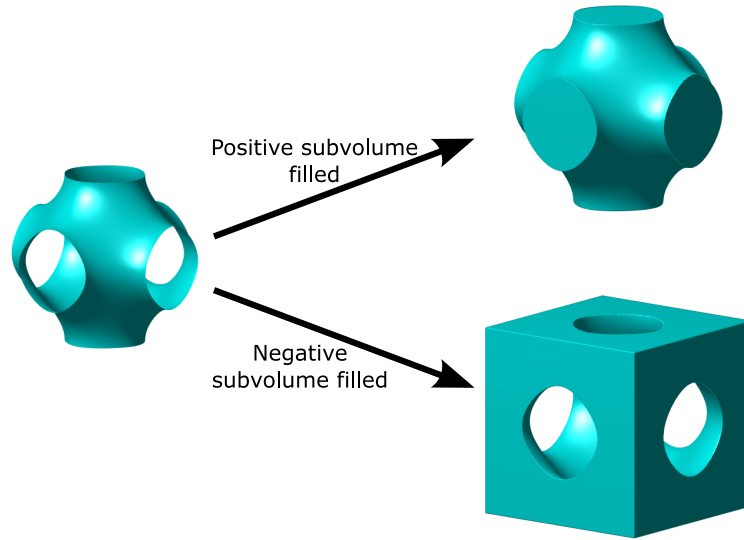


Figure 4.5: Single unit cell of Primitive showing how a particular subvolume can be considered solid material based on the designer's choice.

To establish the relationships, the geometric properties of TPMS structures need to be calculated. The calculated geometric properties will be volume fraction, surface area, and minimum thickness. These geometric properties were chosen as many advanced physical properties are based on the volume and surface area. The minimum thickness is useful for manufacturing feasibility to account for printed toolpath resolution, such as an FDM nozzle size. Analytically solving for the geometric properties is not feasible with currently known methods. For a pure TPMS, i.e. when the isovalue evaluates to zero, the volume and surface area can be analytically solved for if the Weierstrauss equation is known [185–187]. The analytical method assumes the surface is minimal. However, once a TPMS structure is manipulated using isovalues, the surface is no longer minimal, hence the analytical method cannot be used. As such, there are numerous numerical techniques for calculating geometric properties. Based on the aim of this thesis, the preferred numerical techniques will be chosen based on three criteria: computational efficiency, reliability, and accuracy. Five popular TPMS were selected to broaden and generalise formulating the set of numerical techniques. Additionally, both the single and double surface structures will be analysed.

Once the set of numerical techniques are established, the geometric properties for each TPMS structure type will be calculated. Each structure type will be calculated with varying isovalues. To ensure stability, each calculated property undergoes a convergence test until a tolerance is achieved. This will produce a total of thirty datasets. The datasets are then used to calculate polynomial fitting models. These models are the relationships between the geometric properties and the isovalues.

There will be several outcomes of this phase. Firstly, geometric relationships will be established between the isovalue and the geometric properties for the five

TPMS structures. The relationships promote freely generated tailored surfaces without the need of expensive CAD software or advanced mathematical ability. Secondly, the datasets can be used as look-up databases as well as for combining multiple geometric properties, such as calculating SAVR. Finally, the set of numerical techniques and the MATLAB program used to calculate the geometric properties and relationships are openly available on a GitLab repository [238]. These can be used for further expansion for calculating the geometric properties of other TPMS structures.

### 4.3.3 Toolpath Algorithm Development Phase

The next step is to be able to manufacture customised TPMS structures without using intermediary mesh-based file formats. To do this a direct slicing toolpath algorithm will be developed. The direct slicing toolpath algorithm converts contour lines into toolpaths on a slice-by-slice basis. From the previous phase, TPMS structures can be geometrically customised with the relationships. Using the iso-value for a specified geometric property and TPMS structure, the corresponding contour can be translated into toolpaths. This method creates the TPMS structure at the CAM stage as infill that can be customised to geometric specification. The work of this phase is covered in Chapter 6.

A CAM program needs to be created to develop the toolpath algorithm. As such, the program needs to generate machine code for an AM machine to fabricate TPMS structures based on input geometric specifications. This algorithm will not only calculate toolpath lines from contours based on geometric specification but also for solid infill. As such, all types of TPMS structures investigated in the previous phase can be manufactured. The impact is the toolpath algorithm could be adapted as an infill option into commercial CAM software as well as a method to accept implicit-based modelling from either implicitly-based CAD software or intermediary file formats.

The CAM program will produce machine code for Prusa Mk3 i3 FDM machines using PLA filament. FDM machines are ideal for prototyping and developing geometries as they print quickly, are easily accessible, and are cost efficient. Also, PLA is inexpensive, non-toxic, and environmentally safe [206]. Additionally, as PrusaSlicer is an open-source commercial CAM software, the output GCode files and the built-in Gyroid infill algorithm can be utilised to help develop the CAM program and toolpath algorithm.

The steps for calculating the toolpaths from the TPMS implicit functions are as follows. First, the isovalues that correspond to the specified geometry will be calculated based on the relationships from the previous phase adjusting for the nozzle size, overall part size dimensions, and number of lattice unit cells. Then the contours of the isovalues will be calculated using numerical techniques and translated into toolpaths on a slice-by-slice basis. After all slices have calculated toolpaths, the program will output a GCode file.

In the previous phase, the volume of single and double surface structures were controlled by varying the isovalues. Thus, the isovalues will be calculated

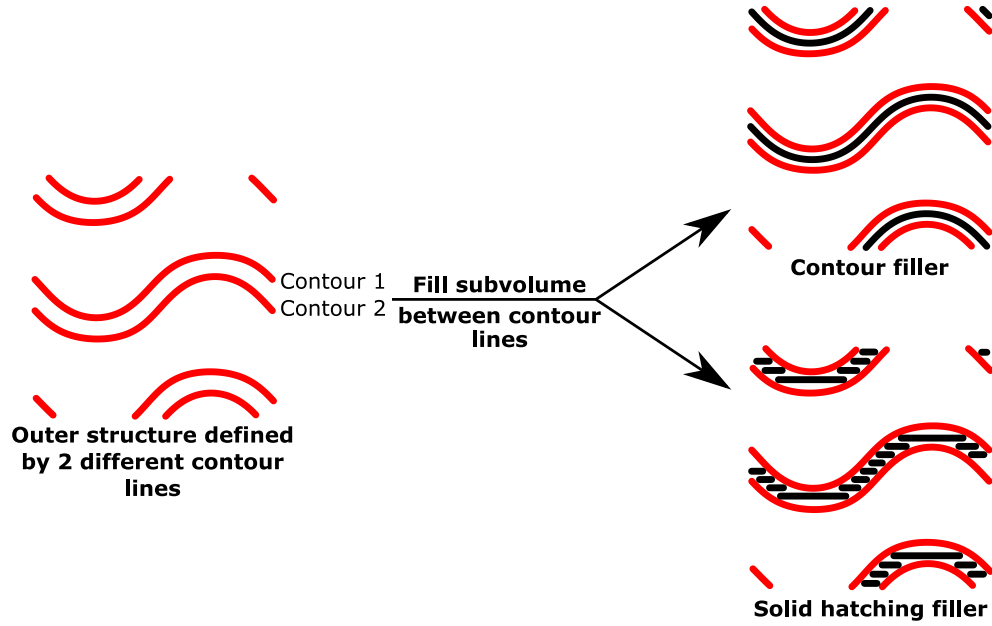


Figure 4.6: Diagram depicting a 2D slice of a double surface Gyroid described with two different contour lines, i.e. Gyroid function set to two different isovalues. To fill the subvolume between the contour lines there are two approaches: contour lines and solid infill. In this example, the contour line method only requires one toolpath line between the perimeter isovalue lines whereas the solid infill method requires multiple short segments.

using the relationships to form the perimeter of the TPMS structure. However, filling the entire “solid material” subvolume requires additional toolpaths, hereby referred to as filler toolpaths. There are different toolpath techniques to fill in the solid region. For example, Ding *et al.* with their direct slicing algorithm used solid hatching inside TPMS structures [16]. The developed program will calculate the inset filler toolpaths from adjacent contour lines. This method will use the minimum thickness relationship for the corresponding TPMS type from the previous phase as well as input specifications and printer settings, such as the nozzle size and number of lattice unit cells. As the minimum thickness relationship will be established this method is will be possible. This creates geometrically customised TPMS structures that are made with nested TPMS based on the inset contour lines. Also, as TPMS contour lines are curved, using contour filler lines reduces the number of toolpath lines as opposed to solid hatching as shown in Figure 4.6.

The outcomes of this phase are a developed toolpath algorithm and a CAM program that uses this algorithm to create GCode for customised TPMS structures. Compared with other research groups that have produced implicit-based direct slicing CAM programs, this will have the novel capability to create a geometrically customised TPMS. As the toolpaths will be adaptively calculated based on the user inputs, designers are able to create geometrically tunable TPMS structures. This is possible with the geometric polynomials from the previous phase.

The algorithm could be implemented into commercial CAM software as customisable infill options. Also, as the algorithm directly uses implicit functions to calculate toolpaths, this could be adapted to accept models from implicitly-defined CAD software and intermediary files. The CAM program is openly-available on GitLab [239].

#### 4.3.4 Experimental Phase

The final phase of this thesis is to experimentally test printed customised TPMS structures. The tests will demonstrate how to relate the geometric relationships to extended engineering properties. As such, this extends the novel research contributions from the prior phase to create tunable TPMS structures for an engineering application. Also, the tests will assess the accuracy of the print compared to the virtual model. The work of this phase is covered in Chapter 7.

When designing a part for an engineering application, i.e. mechanical, fluid dynamics, etc., the desired geometric specification may not necessarily be known. However, by using the developed toolpath algorithm and CAM program to print TPMS structures with varying geometric properties, further relationships can be established. As such, this phase will demonstrate how to relate geometric properties to an engineering requirement. Also, this will test the accuracy of the print which affects the predictability of the further relationship.

To demonstrate establishing further relationships, compressive mechanical testing will be conducted. Compressive mechanical testing has an established relationship between the compressive mechanical properties and the volume fraction of lattices. This relationship is a power law called the Gibson-Ashby relationship given by

$$M = C(V_f)^n \quad (4.1)$$

where  $M$  is the relative mechanical property, i.e. Young's modulus ( $E$ ) or Yield Strength ( $Y$ ),  $V_f$  is the volume fraction between the lattice and a solid object, and  $C$  and  $n$  are constants [240].

The experimental design will follow the ISO-604:2003 Plastics – Determination of compressive properties [241]. The experiments will vary one parameter, the volume fraction, for one type of TPMS structure, the double surface Gyroid. Care will be taken to ensure other potential variables will be kept constant, i.e. same feed material, material brand/colour, TPMS structure type, AM machine type, testing equipment, and CAM program version. Also, the uncertainty will be captured by sample and measurement repetitions.

The geometric accuracy of the printed TPMS structures will be quantified by volume measurements before compression testing. The volume will be measured by first weighing the mass of each specimen and measuring the dimensions of the outer structure. The density of the PLA will be calculated from a section of filament from the same batch as the printed Gyroid specimens. The volume fraction of the Gyroid specimens will be calculated from these measurements. The error

and uncertainties between the volume and compressive property measurements will quantify the accuracy of the printed specimens.

The outcomes of this phase will be the compression testing and comparison analysis results. The compression testing will demonstrate calculating the relationship between volume fraction and compressive mechanical properties for Gyroid specimens. Additionally, this will also tests the compressive properties of printed TPMS structures fabricated using the novel toolpath algorithm from the previous phase. The comparison analysis quantifies the accuracy of the printed TPMS specimens. This can be used for future projects to optimise the toolpath calculations to improve the accuracy and some ideas are outlined in Chapter 8.

## 4.4 Summary

This chapter has discussed the approach and methods developed in this thesis to create an alternative AM process flow and experimentally test printed specimens, focussing on TPMS structures. The methods discussed using implicit modelling and direct slicing to avoid mesh-based bottlenecks from the conventional AM process flow. The work done in this thesis follows the direction of the process flow. As the thesis progresses, the outputs of each phase build on one another to ultimately create a working AM process flow.



# Chapter 5

## Calculation of TPMS Geometric Properties

### 5.1 Introduction

This chapter will cover establishing the relationships between TPMS function iso-values and geometric properties, discussed in Chapter 4 as the geometric property calculation phase of this thesis. This chapter will specifically focus on which geometric properties were calculated, formulating the set of numerical techniques used to calculate the geometric properties, calculation of the geometric property datasets, and establishing the relationships between the TPMS structures and the geometric properties. Although geometric properties are the basis for many advanced physical properties, such as mechanical strength, energy transfer coefficients, etc., there is currently no straightforward method for calculating them. Thus, this shows a clear need for an empirical relationship between the TPMS function isovalues and their resulting geometric properties.

Five TPMS were considered in this chapter: Primitive, Gyroid, Diamond, Neovius, and iWP. These five TPMS were specifically chosen as they are popular amongst the AM community when reviewing the literature in Chapter 2. Establishing methods for calculating the geometric properties for multiple TPMS helps ensure generality. As implicit functions define an infinitely thin surface, the TPMS implicit functions were set to varying isovalues to create structures feasible for AM. The geometric properties calculated for each structure were the volume fraction, surface area, and minimum thickness. These are all relative to one unit cell of the lattice making for ease of scalability for designers.

### 5.2 Background of TPMS structures

Implicit functions are defined as

$$f(x, y, z) = c \tag{5.1}$$

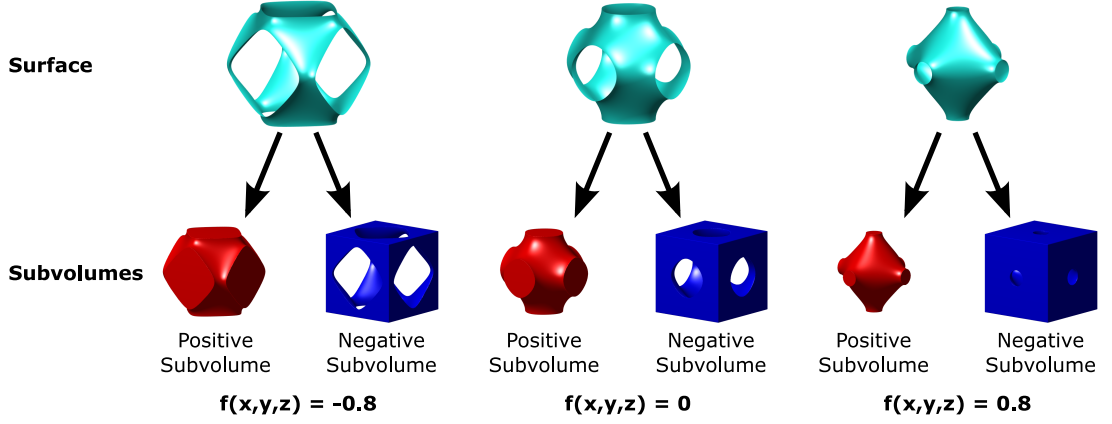


Figure 5.1: Single unit cells of the Primitive set to isovalues of  $-0.8$ ,  $0$ , and  $0.8$ . This shows how the surface moves as the isovalue changes, thereby changing the volume fraction of each subvolume.

where  $f$  is a 3D function with coordinates in  $x$ ,  $y$ ,  $z$  and  $c$  is the constant isovalue where the pure surface exists when the isovalue evaluates to zero. As TPMS are embedded surfaces, varying the isovalue controllably adjusts the volume fraction of the two subvolumes. Visually, this gives the appearance of either ‘inflating’ or ‘deflating’ the surface as shown in Figure 5.1.

The implicit functions of TPMS are an approximation of the Enneper-Weierstrauss representations [175]. The five considered TPMS implicit functions are expressed using the widely adopted trigonometric approximations as follows [201, 214, 220],

Primitive:

$$f(x, y, z) = \cos(\omega x) + \cos(\omega y) + \cos(\omega z) \quad (5.2)$$

Gyroid:

$$f(x, y, z) = \sin(\omega x) \cos(\omega y) + \sin(\omega y) \cos(\omega z) + \sin(\omega z) \cos(\omega x) \quad (5.3)$$

Diamond:

$$f(x, y, z) = \sin(\omega x) \sin(\omega y) \sin(\omega z) + \sin(\omega x) \cos(\omega y) \cos(\omega z) \\ + \cos(\omega x) \sin(\omega y) \cos(\omega z) + \cos(\omega x) \cos(\omega y) \sin(\omega z) \quad (5.4)$$

Neovius:

$$f(x, y, z) = 3 [\cos(\omega x) + \cos(\omega y) + \cos(\omega z)] + 4 \cos(\omega x) \cos(\omega y) \cos(\omega z) \quad (5.5)$$

iWP:

$$f(x, y, z) = 2 [\cos(\omega x) \cos(\omega y) + \cos(\omega y) \cos(\omega z) + \cos(\omega z) \cos(\omega x)] \\ - [\cos(2\omega x) + \cos(2\omega y) + \cos(2\omega z)], \quad (5.6)$$

Table 5.1: Isovalue range for each TPMS where the surface is considered a valid lattice surface. The lattice ranges can be normalised to the range  $[-1, 1]$  with the normalisation factor.

| TPMS      | Min. isovalue | Max. isovalue | Normalisation factor |
|-----------|---------------|---------------|----------------------|
| Primitive | -0.99         | 0.99          | 1.01                 |
| Gyroid    | -1.35         | 1.35          | 0.74                 |
| Diamond   | -0.87         | 0.87          | 1.15                 |
| Neovius   | -0.63         | 0.63          | 1.59                 |
| iWP       | -2.98(-2.60)  | 2.60          | 0.38                 |

in which  $\omega = \frac{2\pi}{L}$  where  $L$  is the side length of the lattice unit cell. The unit cell length  $L$  can easily be scaled to any length dimensions prior to the lattice structure being manufactured.

As the TPMS implicit functions are combinations of trigonometric functions, there are isovalues at which the surface ceases to exist. Furthermore, at the extreme limits of existence, the surface is no longer a continuous lattice. Therefore, the isovalues in which a valid lattice exists needs to be defined for each TPMS. Currently, there is no known method for defining a lattice range, so a visual inspection was conducted and the ranges for each of the five TPMS were generously chosen, such that the all structures within the lattice range were valid lattices. The isovalue range is different for each TPMS as isovalues are essentially arbitrary constant values. Therefore, for the purpose of comparing different TPMS geometric properties, the lattice ranges were normalised to the range  $[-1, 1]$ . The data for iWP was created for the range  $[-2.98, 2.60]$ , however, the range was truncated to  $[-2.60, 2.60]$  for the fitting and plotting. This ensures that all normalised ranges were centred on an isovalue of zero, which promotes ease of comparison. The lattice isovalue ranges and the normalisation factors are summarised in Table 5.1.

There were two types of surface structures considered, the single and double surface structures. The single surface structure is defined as the TPMS implicit function set to one isovalue and one subvolume was considered “solid material” or “inside” and the other subvolume is free space or “outside”. The double surface structure is defined as two TPMS implicit functions (of the same TPMS) set to different isovalues where the space between the surfaces was considered “solid material” or “inside”. The five TPMS single and double surface structures are depicted in Figure 5.2.

### 5.2.1 Definition of the Geometric Properties

The three geometric properties investigated in this chapter were the volume fraction, surface area, and minimum thickness. Volume and surface area are elementary geometric properties that relate to many different types of physical properties. The calculated properties can also be combined to other useful properties such as SAVR. The minimum thickness is useful for manufacturing feasibility.

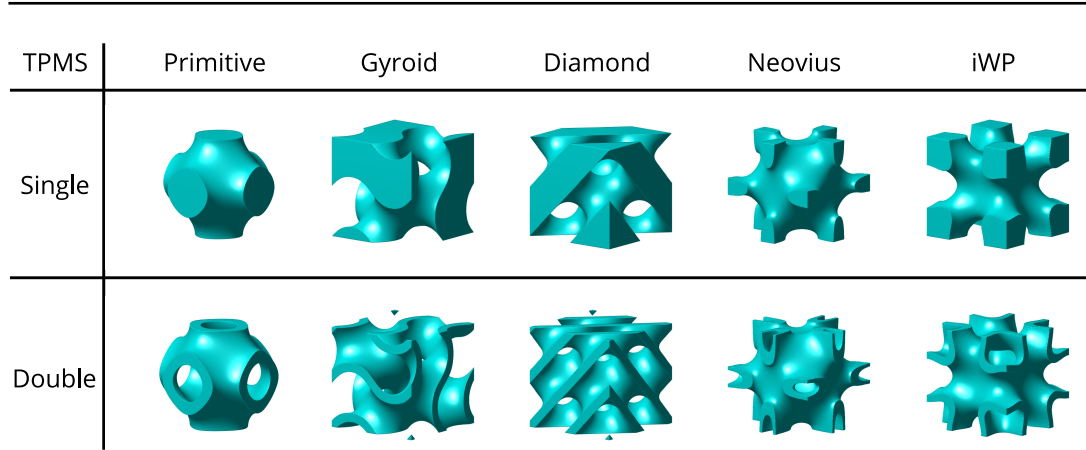


Figure 5.2: Single unit cells of the Primitive, Gyroid, Diamond, Neovius, and iWP for single and double surface structures.

For example, if the model structure is too thin for an FDM nozzle diameter, this should be flagged to the designer.

### 5.2.2 Convergence Testing

All geometric calculations used convergence testing to ensure resulting values were consistent and accurate. As the accuracy of numerical techniques improve with iteration of increasing resolution to an extent, it was necessary to identify when the value asymptotes. In this thesis, a convergence tolerance was generously set to 1%. While in many cases this was generous, this was to maintain generality of the calculation to encompass multiple types of TPMS as well as isovalue ranges at the extrema. During the convergence test, the current iteration was compared with the previous two iterations to check they were within 1% of each other. This was to help prevent selecting an oscillating value. As such, all values in the finalised datasets have passed the convergence test.

## 5.3 Numerical Techniques for Geometric Calculations

### 5.3.1 Assessment of Various Numerical Techniques

There are various numerical techniques that are relevant to estimating the geometric properties of interest. Some operate on the underlying surface equations and others require an approximated surface mesh. The following sections describe the techniques that were implemented and trialled but ultimately rejected in pursuit of a preferred suite of numerical techniques.

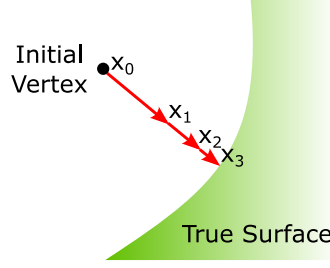


Figure 5.3: The gradient descent method for correcting vertices onto a surface. The vertices are iteratively corrected by minimising the gradient value using a specified step-size.

### Vertex Correction

Often, implicit surfaces are visualised by approximating the surface using a triangular mesh approximation. The *de facto* method for this is to use a marching algorithm and, more often than not, the marching cubes algorithm. The result is a triangle mesh approximation of the surface, where vertices may not lie exactly on the underlying implicit surface. As such, it was necessary to correct the positions of these vertices prior to estimating the geometric properties of the surface.

The first method assessed was the gradient descent method. This method iteratively corrects a coordinate's location by minimising the gradient value as shown in Figure 5.3. The governing equation is

$$x_{n+1} = x_n - \alpha \nabla f(x) \quad (5.7)$$

where  $x$  is the vertex coordinate,  $\alpha$  is a specified step-size,  $\nabla f(x)$  is the gradient of the implicit function, and  $n$  is the iteration. This is repeated until a specified convergence tolerance is met.

The difficulty with using this method was that it was difficult to specify a step-size that was suitable for all five TPMS structures. Furthermore, this technique was susceptible to finding unwanted local minima if the specified step-size was too large or the initial vertex was far from the surface [242].

Another method assessed was a 1D vertex correction method. This method corrects vertices in 1D, in either  $x$ ,  $y$ , or  $z$ , using the TPMS explicit functions. For example, if a coordinate is to be corrected in the  $x$ -direction,  $x$  will be solved for using the explicit function for  $x$  holding  $y$  and  $z$  constant. Before proceeding with this method, each of the TPMS functions needed to be converted into an explicit form. In solving for the explicit functions, the following two general explicit forms arose for the different TPMS. The form for Primitive and Neovius is

$$\psi = \frac{\arccos A}{2\pi} \quad (5.8)$$

and for Gyroid, Diamond, and iWP is

$$\psi = \frac{\arccos 0.5(-A \pm \sqrt{A^2 - 4B})}{2\pi} \quad (5.9)$$

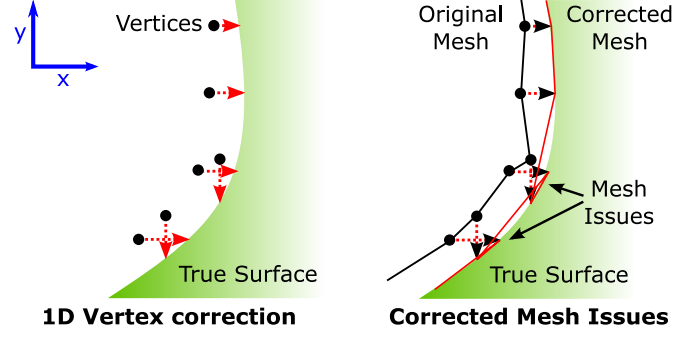


Figure 5.4: Correcting initial vertices in 1D using the explicit forms of the TPMS functions. The correction would be along the  $x$ ,  $y$ , or  $z$  dimension depending on which explicit form was used. The right-hand side depicts how this can lead to mesh issues when adjacent vertices are corrected in different dimensions by inverting triangles.

where  $\psi$  represents either  $x$ ,  $y$ , or  $z$ , and  $A$  and  $B$  are unique coefficients that depended on the TPMS functions and the isovalue.

Though the explicit forms were established for each surface, some significant challenges remained. As the TPMS functions are comprised of trigonometric functions, the explicit forms evaluate to multiple roots (possible surface locations). However, this issue was surmountable, and methods for identifying the correct roots were formulated. The correct root for certain domains was determined arduously by visual inspection for each TPMS. Furthermore, vertices could conceivably be corrected in either the  $x$ -,  $y$ -, or  $z$ -direction. The sensible choice was to trial all three directions and establish the shortest distance to the surface. Nevertheless, issues still remained, as the triangulation of the mesh could be corrupted (inverted triangles) during correction, as shown in Figure 5.4. As such, despite this being an efficient method to correct vertices precisely onto the surface, there were sufficient pitfalls in terms of mesh integrity for this method to be rejected. Furthermore, the difficulties of this method antagonises the aim of this thesis.

## Volume Fraction Calculation

Deterministic methods for calculating the volume of  $n$ -sided polygon structures require closed (manifold) meshes [243]. The TPMS structures contained within a lattice unit cell are open at the unit cell boundaries. Thus, the deterministic methods are invalid unless an additional meshing step is added to close the mesh at the boundaries. Figure 5.5 shows the mesh estimating the surface, the mesh at the unit cell wall “inside” the structure, and where the meshes need to be stitched. While it is possible to create a closed mesh between the TPMS structures and the unit cell wall boundaries, there are often issues with stitching the edges of dissimilar meshes. This leads to an open surface issue. Ultimately, this was deemed a sufficient barrier to reject this method, despite the initial appeal of estimating the volume fraction this way.

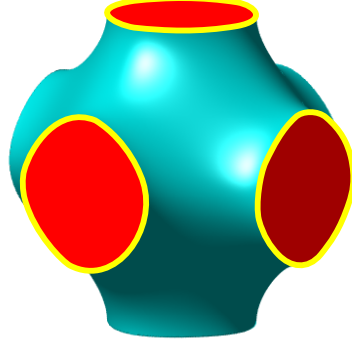


Figure 5.5: Two different meshes on a Primitive single surface structure. First in blue showing the mesh estimating the surface and the second in red estimating the unit cell wall “inside” the structure. These two meshes would require an additional step to seamlessly stitch the two together to use the deterministic volume fraction calculation.

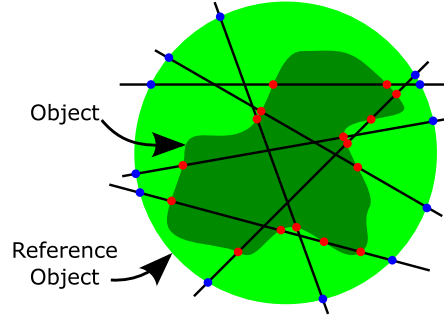


Figure 5.6: Quasi-Monte Carlo integration method for surface area calculation. Randomised uniformly distributed lines are created such that they intersect the reference object. The surface area is based on the ratio of intersection points with the reference object to the object of interest.

### Surface Area Calculation

A quasi-Monte Carlo integration method proposed by Li *et al.* [244] to calculate surface area of a surface was trialled. To calculate the surface area, the TPMS were bounded in full by a reference object with a known surface area, i.e. a sphere, as shown in Figure 5.6. Then, a set of uniformly distributed lines was generated such that all lines intersect the reference object. The lines are generated relative to the centroid of the reference object. A quasi-Monte Carlo of affine transformations were performed on the lines based on four parameters,  $r$ ,  $\theta$ ,  $\phi$ , and  $\psi$  as shown in Figure 5.7. The distance along the sphere radius  $R$  was defined by  $r$  existed in the domain of  $r \in [0, R)$ . The latitude and longitude,  $\theta$ ,  $\phi$ , respectively existed in the domain of  $\theta \in [0, \pi]$  and  $\phi \in [0, 2\pi)$ . The angle between each line and a defined reference line,  $\psi$ , tilted the generated line in the domain  $\psi \in [0, \pi)$ .

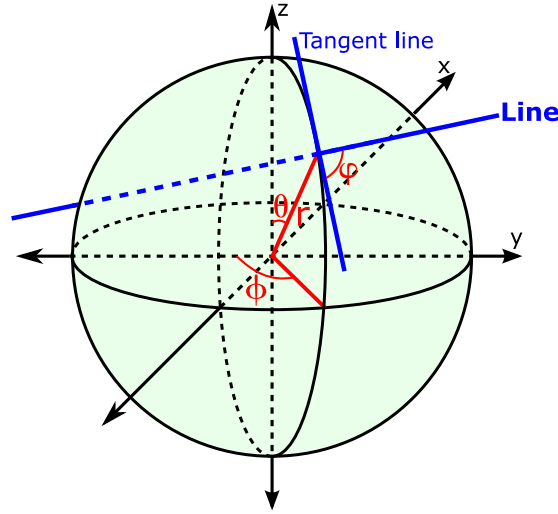


Figure 5.7: The four randomised parameters used to generate the uniformly distributed lines for a Quasi-Monte Carlo integration method.

The 'quasi-Monte Carlo' sampling technique arose due to low discrepancy pseudo-randomised points seeding issues prior to 2007 [245,246]. This ensures the generated points are more uniformly distributed but not perfectly uniform whilst keeping properties of some randomised numbers. Specifically, scrambled Sobol sequences were implemented as they are more stable than Hatton sequences. Also, when applied they have a lower absolute error when generating numbers for dimensions greater than one [247]. However, since the method from the Li *et al.* publication, modern pseudorandom number generators use the Mersenne Twister algorithm with robust seeding such that this method was obsolete for this purpose [246]. Currently, the Mersenne Twister is the most widely used pseudorandom number generators across different platforms. This is the default generator algorithm since R2007a and previous generators were considered 'flawed' [248]. As such, using modern generators was deemed a better method to generating the parameters for the Monte Carlo integration calculation.

The appeal of the quasi-Monte Carlo approach was that it is a mesh-free method. It therefore did not require an accurate mesh approximation of the underlying implicit surface. However, the reality of this approach was that it is far less efficient than using a refined triangle mesh approximation of the surface. The triangular mesh can be used to calculate the surface area by calculating the summation of the areas of all triangle facets. The quasi-Monte Carlo method required considerable additional computation in order to converge to the same extent as the triangle mesh method. A comparison test of the two methods for calculating the surface area of a sphere was performed. The triangle mesh method used the MATLAB `isosurface` function to build a series of increasingly refined mesh approximations of the sphere. A comparison of the two methods' convergence, given in Figure 5.8, clearly shows that the triangular mesh method leads to more accurate results at a lower computational expense.



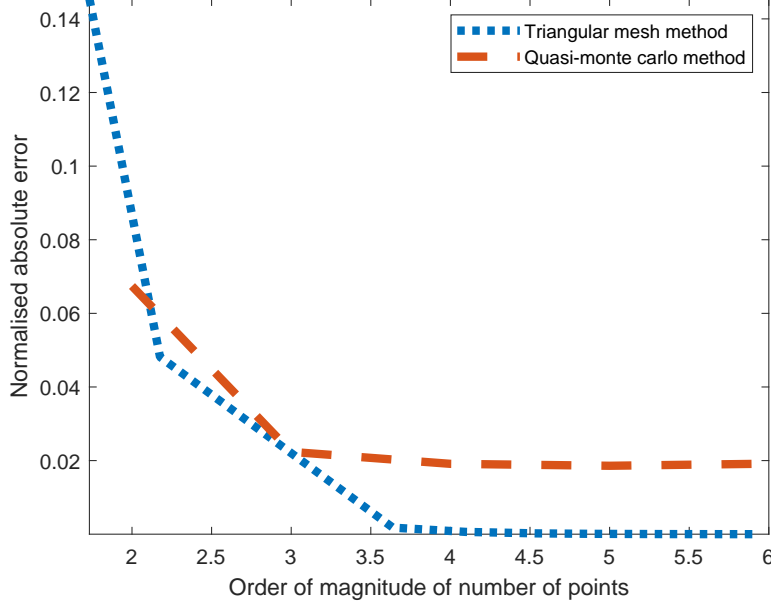


Figure 5.8: Comparison of calculated surface area values for a sphere between the quasi-Monte Carlo integration method and the triangular mesh method. The plot compares the absolute error, i.e. the absolute value of the difference between the estimated surface area and the true surface area, normalised by the true surface area value. Both methods are subject to an increasing number of points to show the difference in the convergence. The number of points refers to the net size for the quasi-Monte Carlo method and number of vertices of the triangular mesh method. It is clear that beyond  $10^3$  points the triangular mesh method has converged to a more accurate value whilst the quasi-Monte Carlo is behaving asymptotically.

### Minimum Thickness Calculation

The Fast Marching Method (FMM) is a method to search for the shortest distance from a starting location [249]. FMM starts at a vertex and expands outwards iteratively with larger and larger spheres until a target is reached. In this application, the starting vertex was on the first surface. These vertices were defined from a triangular mesh. An iterative outward search was conducted until the target surface was reached, as shown by Figure 5.9.

The spheres were discretely estimated by sphere nodes, i.e. points that lie on the sphere. To determine if the target surface was reached, the sphere nodes were evaluated using the target surface implicit function. The target was reached if sign of a sphere node function value was different to the starting vertex function value. As the searching method needs to occur in the correct subvolume, portions of the sphere in the other subvolume were considered “frozen” and were not stored or expanded.

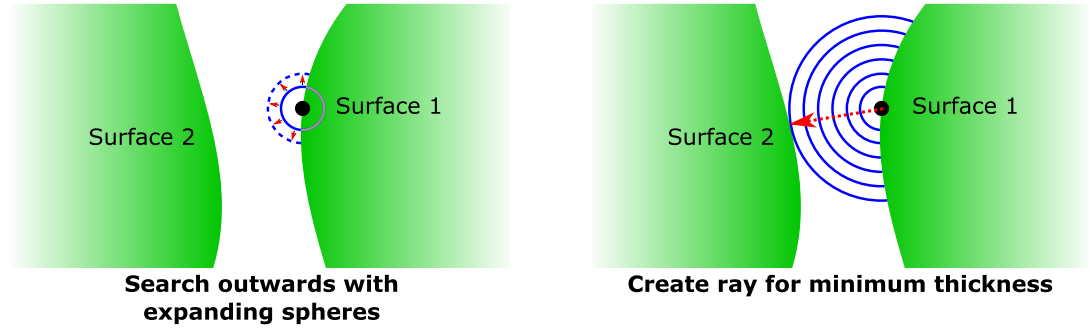


Figure 5.9: The FMM for minimum thickness calculation. This method measures the minimum distance between two surface starting from the first surface and expanding outwards until the second surface is reached. As shown in the left-hand side, if part of the search sphere is within a forbidden region (grey nodes), the search is terminated for that portion of the sphere.

FMM was rejected as there were computational resource limitations and the minimum thickness definition was ambiguous for this application. Calculating the minimum thickness using FMM used considerable computational resources. A large number of vertices on the surface is required to ensure a local minima is not obtained. Also, each vertex search requires discretely-described spheres requiring extensive computational memory. As each vertex search was independent from one another and parallel computing was employed, the calculation still required the use of high performance computing (HPC). This was computationally inefficient, used resources not widely available, and convergence testing could not be conducted due to memory limitations. The computational memory limits and lack of convergence testing resulted in unreliable data.

Additionally, as FMM detects the target with a sign change, this becomes ambiguous when defining thickness for a single surface structure. With structures defined by two different isovalues the end goal was determined by the target implicit function value sign change. Whereas, with a single surface, by the implementation of FMM, a distance could technically be defined anywhere on the surface adjacent to the starting vertex, as shown in Figure 5.10. Therefore, a different definitive method for calculating minimum thickness was required.

### 5.3.2 Formulated Set of Numerical Techniques

After assessing multiple methods, a set of numerical techniques was chosen to generate the datasets for the geometrical properties of the TPMS structures. As such, the next section details the process and calculation of the finalised datasets.

## 5.4 Generating Datasets

A MATLAB program was created to generate the datasets for the geometric properties. The version of MATLAB used was R2019a and the program is openly

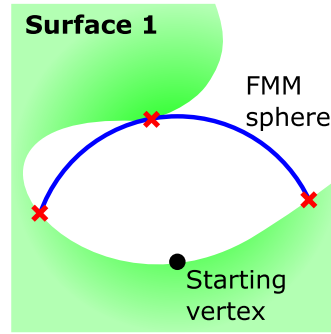


Figure 5.10: FMM thickness ambiguity issues for single surface structures. The diagram shows three points, red x's, on the FMM searching sphere that could potentially be defined as an endpoint if thickness were based on a sign change.

available in the GitLab repository [238]. The developed MATLAB program calculates the geometric properties for the five TPMS for each single and double surface structures with varying isovalues. In total, thirty unique datasets were produced for each type of lattice structure and geometric property. As most of the code was generalised in the program, from input parameters to tolerances, additional TPMS could theoretically be added.

### 5.4.1 MATLAB Program

The flowchart for how the MATLAB program operates is shown in Figure 5.11. There are two main phases in the program within the top-level function (`TPMS_Analysis.m`): (1) calculating the geometric property datasets for each TPMS structure and (2) polynomial fitting and plotting the structures. The inputs for the program are strings indicating which TPMS to evaluate and by default all five are calculated if none are specified. The program first initialises structures, output directories, coarse mesh surface estimations, etc. During this initialisation the program checks whether text files of the datasets are present in the designated output directory. During phase 1, each geometric property is calculated to convergence for each TPMS structure type. The results are exported as a text file in the output directory. The program will only calculate datasets if they are not present in the output directory. Phase 1 is bypassed if all dataset text files are present.

Phase 2 reads in the dataset text files. For double surface structures, volume fraction and surface area raw data values are combined by subtraction and addition respectively. The Chebyshev polynomial fitting models are then fit and created for all geometric properties and structure type for a total of thirty polynomial models. The polynomial coefficients are exported in text files. Along with the coefficients, residual plots and tolerance logs providing details on the fitting are output as well. Plots for each TPMS structure, geometric property, and structure type are then created and output as MATLAB fig and pdf files. Customised plots where multiple plots are created on one figure is a separate provided MATLAB top-level function called `generateCustomPlots.m`. This function can create

plots based on the user inputs of TPMS, type of geometric property, and a combination of properties, such as SAVR. The separate plots are created and output with normalised and non-normalised isovalues as MATLAB fig and pdf files.

### 5.4.2 Mesh-free Monte Carlo Estimation of Volume Fraction

A Monte Carlo integration method was used to estimate the volume fraction (Figure 5.13). Samples of random points were generated uniformly within the bounding box of a lattice unit cell, ranging from  $[-0.5, 0.5]$  in the  $x$ -,  $y$ -,  $z$ -directions. The volume fraction was calculated as the ratio of points that were “inside” the structure (points evaluating to a negative number using the TPMS implicit equation) to the total number of points generated [250]. The number of randomised points was increased until the volume fraction converges to within 1% of the previous two calculated values.

The convergence testing starts with  $10^7$  randomised points. With each convergence iteration, the number of randomised points was increased by  $\log_{10}(n + 0.1)$  with a new set of generated randomised points. At least three iterations were performed to ensure the volume fraction value fits within the convergence criteria. Figure 5.12 shows an example of a convergence plot for the iWP with an offset of  $-2.98$  starting with  $10^2$  points until  $10^7$  points. This shows that at  $10^5$  points the value comfortably converges below the 1% tolerance.

The drawback of Monte Carlo integration was that the calculation asymptotically approaches the true value [251]. To better understand the uncertainty arising from Monte Carlo integration, each volume fraction calculation performed to convergence for the Primitive surface was repeated 20 times for each isovalue. From these results the largest of these standard deviations was 0.016%, well below the convergence tolerance of 1%, with each value calculated with  $10^{7.2}$  points. While the convergence tolerance may appear highly generous, some of the other TPMS require considerably larger sample sizes to achieve convergence and this can lead to memory shortage issues.

The algorithm used to generate uniformly distributed random points was the Mersenne Twister algorithm, as implemented by the MATLAB version R2019a `rand` function [252]. Concerns over the randomness of previous iterations of the `rand` function have been raised [244], but the Mersenne Twister algorithm was implemented to mitigate these concerns.

### 5.4.3 Coarse Sampling of the TPMS Unit Cells for Mesh-Based Estimations

Estimation of the surface area and minimum thickness properties start by approximating the surface as a triangular mesh. Any meshing algorithm such as Marching Cubes can be used to generate an initial triangular mesh. However, care must be taken to ensure that the vertices are ordered to produce consistent

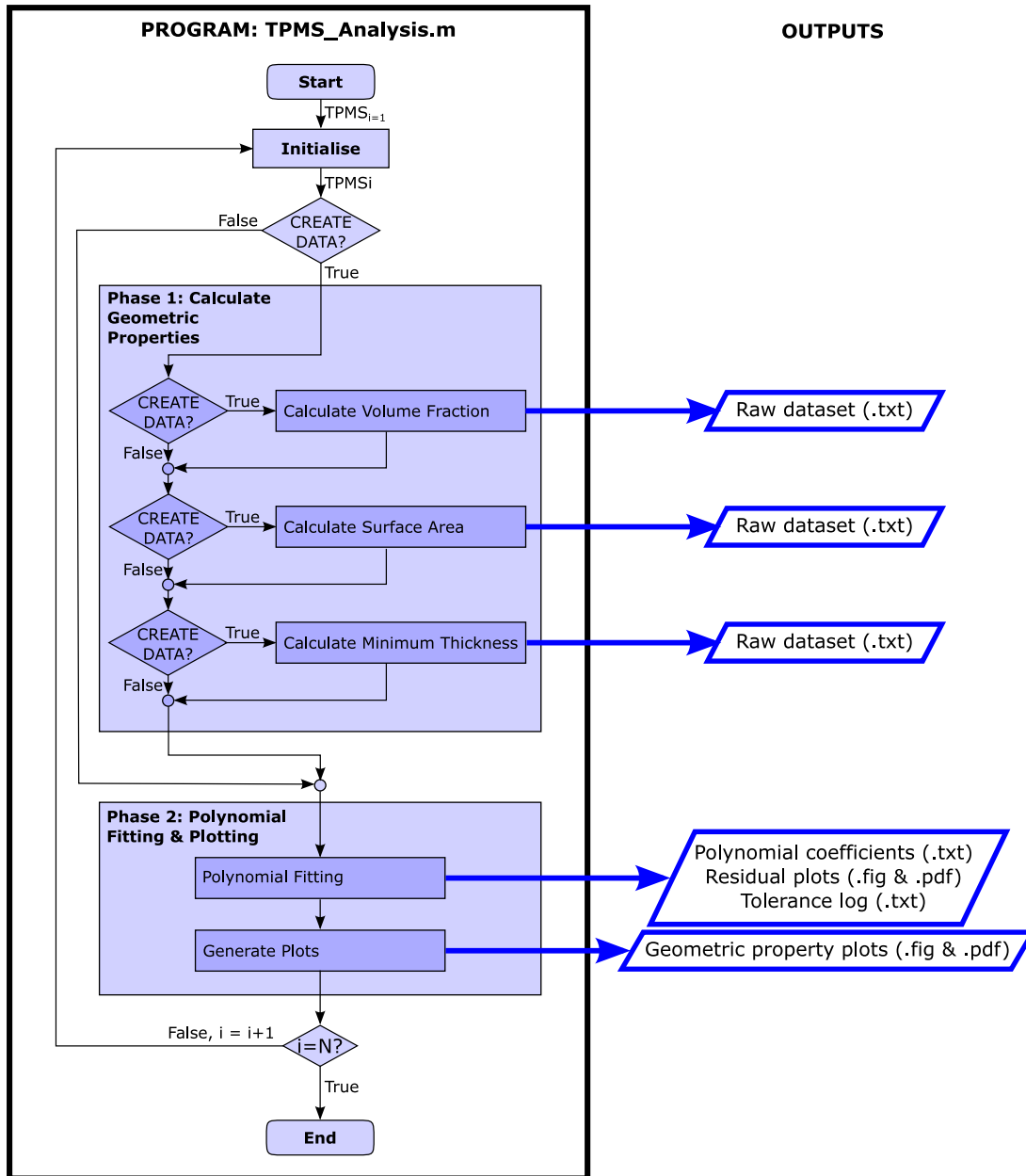


Figure 5.11: Flowchart for MATLAB program used to calculate the TPMS structure geometric properties that is available on the GitLab repository [238]. The program is conducted in two phases within the top-level function (TPMS\_Analysis.m): (1) calculating the geometric property datasets for each TPMS structure and (2) fitting and plotting the structures. The inputs and outputs of the program are listed as they are needed and produced. The boolean flags indicate whether to calculate and create dataset files based on if they exist in the output directory.

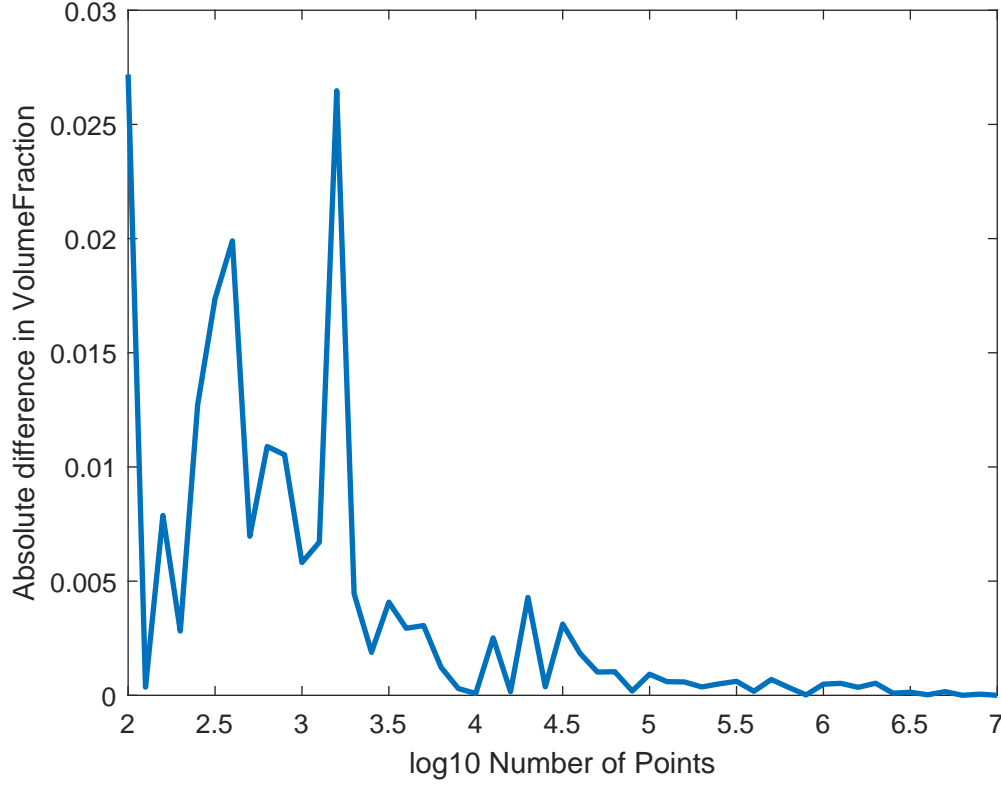


Figure 5.12: Example of volume fraction convergence for iWP with an isovalue of  $-2.98$ . The plot depicts an increasing number of randomised points used to calculate the volume fraction starting ranging from  $10^2$  to  $10^7$  points. The y-axis, the absolute difference in volume fraction, shows that beyond  $10^5$  points comfortably falls below the 1% convergence criteria.

face normals, vertices are not duplicated, a watertight mesh is created, and no degenerate triangles are present in the final mesh.

The MATLAB `isosurface` function used to generate an initial coarse mesh, was seeded by a uniformly spaced  $15 \times 15 \times 15$  grid. As this produces an estimate of the surface, these initial vertices were then corrected to machine precision (double precision floating point) on the surface using the Newton-Raphson method [253]. The gradient of the TPMS surface is the normal vector

$$\nabla f(x, y, z) = \left[ \frac{\partial f}{\partial x}, \frac{\partial f}{\partial y}, \frac{\partial f}{\partial z} \right]^T. \quad (5.10)$$

The vertex correction is performed along the surface normal, ensuring that the integrity of the mesh is preserved. The MATLAB `isosurface` creates a mesh that meets the edge of the unit cell such that the surface is not jagged.

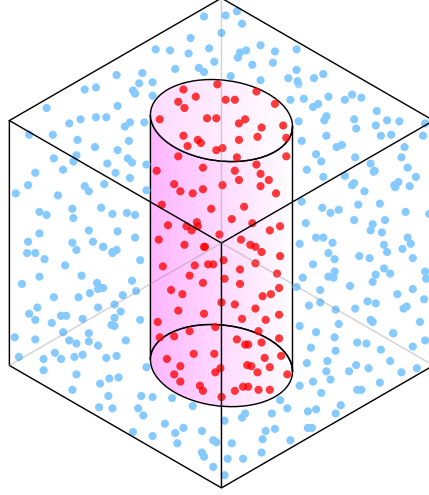


Figure 5.13: Monte Carlo method for calculating volume fraction. Uniformly distributed randomised points spread throughout the unit cell. These evaluated for whether they fall “inside” (red) or “outside” (blue). The volume fraction is calculated as the ratio between these points.

#### 5.4.4 Convergence for Mesh-Based Estimations

After the initial coarse sampling of the surface, additional vertices were added via subdivision of each triangular face. In this method, each triangular face is subdivided by placing a midpoint along each triangle edge. Connecting these points to form a new central triangle results in three smaller triangles arranged around it, as shown in (Figure 5.14). Each new vertex is then corrected with the Newton-Raphson method. This midpoint method could further be improved by creating the triangles adaptively so that triangles tend away from extreme aspect ratios.

This subdivision is used to iteratively produce finer meshes to check the convergence lies within 1% of the previous two calculated values. Any further tolerance refinement would have been likely to exceed memory limitations on the computer hardware.

#### 5.4.5 Mesh-Based Estimation of the Surface Area

Once an accurate triangular mesh has been established for a given TPMS surface, the summation of all triangle areas gives an approximation of the surface area within the unit cell [254]. As previously mentioned, this calculation is improved by mesh subdivision until a tolerance is met. The area of each triangle is efficiently calculated as half the magnitude of the cross product of two vectors that define sides of the triangle shown by

$$A = \frac{1}{2} \sum_i^N \vec{a}_i \times \vec{b}_i \quad (5.11)$$

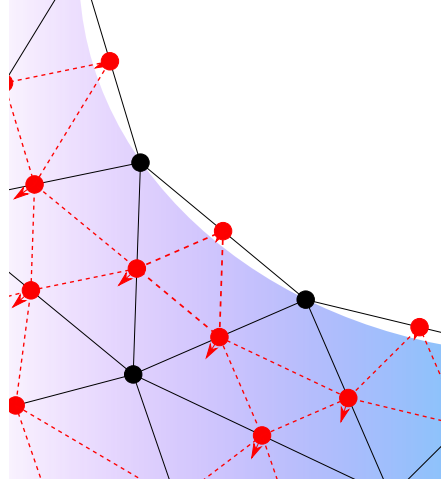


Figure 5.14: The method for iteratively subdividing the mesh. First midpoints are added along each edge of each triangle face, subdividing each triangular face into four triangular faces. Then the new midpoints are corrected onto the surface using the Newton-Raphson method

where  $A$  is the total surface area,  $i$  is each triangle,  $N$  is the total number of triangles, and  $a$  and  $b$  are the vectors that define the sides of each triangle.

#### 5.4.6 Mesh-Based Estimation of the Minimum Thickness

For the double surface structure, the minimum thickness is defined as the minimum distance between the two surfaces that define the volume (Figure 5.15a). As mentioned earlier, the vector defining the absolute minimum distance lies along the normal of both surfaces [255]. The minimum thickness for the single surface structure is open to interpretation and requires a clear definition (Figure 5.15b). As such, for consistency with the double surface structure, the minimum thickness for the single surface structure is defined as the minimum distance along an inward facing normal vector before intersecting the same TPMS surface again.

The minimum thickness calculation is performed by searching along the surface normal of all vertices on the meshed surface. In the case of the double surface structure, the thickness calculation is always performed from the ‘outer’ surface (i.e. the surface with the highest isovalue). The searching is performed by stepping inwardly along the normal vector by a distance much smaller than the conceivable minimum thickness value. At each step, the TPMS isovalue is calculated for the current  $x, y, z$  position until this isovalue is greater than the isovalue of the surface being searched for. The precise position of the surface crossing is then located via the Newton-Raphson method as before. As previously mentioned, this process is repeated with increasingly subdivided meshes until the value has converged.



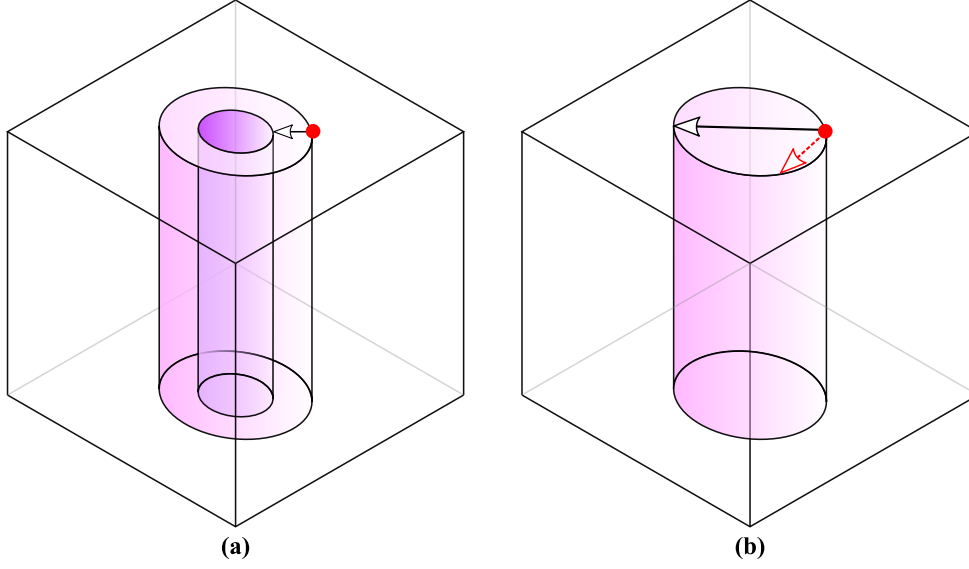


Figure 5.15: Definition minimum thickness used in this work. For double surface structures (a) the minimum thickness is well defined as the minimum distance from one surface to the other surface. The vector representing this displacement is mathematically constrained to be normal to both surfaces. For single surface structures (b) minimum thickness is less well defined as the displacement vector is between two points on the same surface. This could be minimised by a small displacement perpendicular to the surface (red arrow). Hence, for consistency with the double surface structure, the minimum distance for the single surface structure is defined such that the displacement vector is constrained to be normal to the surface.

### 5.4.7 Robust Chebyshev Fitting

To enable integration of the data generated in the above methods into the design process, polynomial functions were fitted to the data points. The fitting model provides the designer with a relationship between the geometric properties and the TPMS isovalue. The resulting polynomial coefficients are easy to incorporate into various modelling platforms to enhance modelling capabilities.

Polynomial fitting was preferred over piecewise interpolation of all data points, as interpolation will over-fit to the uncertainties in the underlying data set. However, simple polynomial fitting is vulnerable to Runge's phenomenon, resulting in unwanted oscillations at the periphery of the fitted region [256]. To avoid Runge's phenomenon, Chebyshev polynomials were fitted to the data. Additionally, the bounded Chebyshev polynomials mirrors the isovalue limits where the TPMS lattice is valid.

The recurrence relationship for determining the Chebyshev polynomials of the first kind for second order and higher are

$$T_n(x) = 2xT_{n-1} - T_{n-2} \quad (5.12)$$

where  $T_n$  is the  $n$ th Chebyshev polynomial of the first kind and  $x$  is the isovalue. The zeroth and first order polynomials are defined as 1 and  $x$  respectively.

The Chebyshev fitting was performed as a linear regression via matrix inversion [257]. Prior to fitting, the isovalue range was scaled to the interval  $[-1, 1]$  over which the Chebyshev polynomials are normalised. The Vandermonde matrix is determined using the normalised isovalues. The Vandermonde matrix, defined by

$$V = \begin{bmatrix} T_0(x_1) & T_1(x_1) & T_2(x_1) & \cdots & T_n(x_1) \\ T_0(x_2) & T_1(x_2) & T_2(x_2) & \cdots & T_n(x_2) \\ T_0(x_3) & T_1(x_3) & T_2(x_3) & \cdots & T_n(x_3) \\ \vdots & \vdots & \vdots & \ddots & \vdots \\ T_0(x_m) & T_1(x_m) & T_2(x_m) & \cdots & T_n(x_m) \end{bmatrix}$$

where  $V$  is the Vandermonde matrix,  $T(x)$  are Chebyshev polynomials of the first kind,  $x$  are the isovalues,  $m$  is the total number of isovalues evaluated, and  $n$  is the highest order of Chebyshev polynomials used. The coefficients are then determined using linear least squares as defined

$$c = R(Q^T y)^{-1} \quad (5.13)$$

where  $c$  is the Chebyshev coefficient,  $Q$  and  $R$  are the QR decomposition of the Vandermonde matrix, and  $y$  is the corresponding geometric property value. After fitting, the final function is scaled back to the correct range.

For single surface structures, having a single varying isovalue, the fitted functions are of the general form

$$G_{ss}(x) = \sum_n c_n T_n(x), \quad (5.14)$$

where  $T_n$  is the  $n$ th Chebyshev polynomial of the first kind [258],  $c_n$  is the  $n$ th coefficient, and  $x$  is the isovalue. For double surface structures with two isovalues the fitted functions are of the general form

$$G_{ds}(x, y) = \sum_{n,m} c_{nm} T_n(x) T_m(y), \quad (5.15)$$

where  $x$  and  $y$  are the isovalues of the two surfaces.

Fitting Chebyshev polynomials comes with numerous advantages. Due to the lack of an appropriate weighting function, the polynomials are not truly orthogonal. However, each antinode of each polynomial has a magnitude of unity. As such, the magnitude of each coefficient is directly comparable. This allows the coefficients to be compared to provide an objective criterion for the order of the final fit. Insignificant higher order terms can then be truncated from the fit.

For single surface structures, the order of the final fit,  $n_f$ , was set such that  $c_{n_f+1} < 10^{-4}$  and  $c_{n_f+2} < 10^{-4}$ . For double surface structures, the order of the final fit,  $N_f$  (where  $N = n + m$ ), was set such that  $c_{nm} \leq 0.05$  for all  $n, m$  where  $n + m = N_f + 1$  or  $n + m = N_f + 2$ . Plots in Appendix A show the polynomial

fitting model plotting with the raw data and the residual plots. The residual plots for some TPMS structures have patterning but as the residuals are very low this does not affect any confidence in the fitting model. Some caution needs to be taken when using the model for certain TPMS double surface structures at the isovalue extrema beyond the centre 95% of the isovalue range as the fitted model does not fall within 1% error of the raw data but still falls within 7%.

Having the Chebyshev polynomial coefficients requires users to have a working knowledge of implementing Chebyshev polynomials. As this may present challenges, the output polynomial coefficients were reformatted into the standard polynomial form. For single surface structures, the output coefficients have the form

$$y = \sum_{n=0}^N b_n x^n \quad (5.16)$$

where  $b_n$  is the output coefficient value,  $x$  is the isovalue,  $y$  is the polynomial fit value, and  $n$  is the polynomial order, and  $N$  is the maximum polynomial order that matches the tolerance criteria and are considered significant. For double surface structures, the output coefficients have the form

$$z = \sum_{n=0}^N \sum_{m=0}^M b_{m,n} x^m y^n \quad (5.17)$$

where  $b_{m,n}$  is the output coefficient value,  $x$  and  $y$  are the isovalues of the two surfaces where  $y > x$ , the sum of  $m$  and  $n$  is the polynomial order, and the sum of  $M$  and  $N$  is the maximum polynomial order that matches the tolerance criteria and are considered significant. The ease of implementing standard polynomial coefficient aligns with the aim of this thesis of reaching a wider audience.

## 5.5 Results

Each TPMS lattice structure has different trends in the geometric properties making some lattices more suitable for certain applications. To directly compare the geometric properties for the five computed TPMS lattice structures, the isovalue range (see Table 5.1) was normalised into the range  $[-1, 1]$ , thus comparing each lattice over the full ranges defined in Table 5.1. Due to the asymmetric range of the iWP lattice, the unscaled range has been truncated to  $[-2.60, 2.60]$  before normalising to ensure that a normalised isovalue of zero still corresponds to the pure iWP surface.

To analyse trends for the double surface structures, the geometric properties for symmetric structures are plotted where the isovalue for the two surfaces are of equal magnitude and opposite sign. Contour plots that show the full parameter range investigated are included in the data repository and are not reported here. All datasets, the final polynomial coefficients in standard polynomial form, and supplemental figures (data plots, convergence plots, polynomial residual plots)

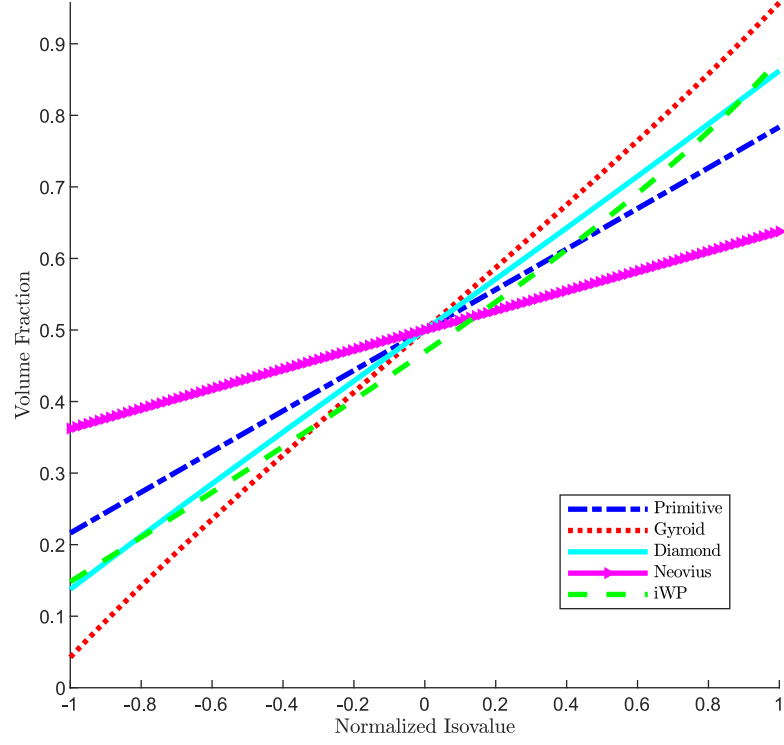


Figure 5.16: Comparison of the volume fraction as a function of normalised isovalue for all single surface TPMS structures, showing almost linear dependence. Normalised isovalues can be converted to isovalues by dividing by the normalisation factor given in Table 5.1.

are available from the University of Bath data archive [259] and the code used to generate this data is hosted on GitLab [238].

### 5.5.1 Volume Fraction

The volume fraction for all single surface TPMS structures monotonically increases with the isovalue, see Figure 5.16. The volume fraction is an almost linear function of isovalue, but each function is slightly sigmoidal for all single surface structures except the iWP structure, which has a monotonically increasing gradient. The volume fraction for all single surface structures, except the iWP structure, intersect at 0 when the isovalue is zero. The Gyroid structure has the largest range of volume fractions ranging from 4% to 96%, whereas the Neovius structure only ranges between 36% and 64%. Thus, the Gyroid single surface structure provides the maximum tunability for internal lightweighting, when compared to the other single surface structures. The data is consistent with the work of [10], which investigated the volume fraction of the single surface structures of Primitive, Gyroid, and Diamond lattices.

The volume fraction for double surface TPMS structures is presented in Figure 5.17 and 5.18. As expected, for the double surface structures there is no minimum

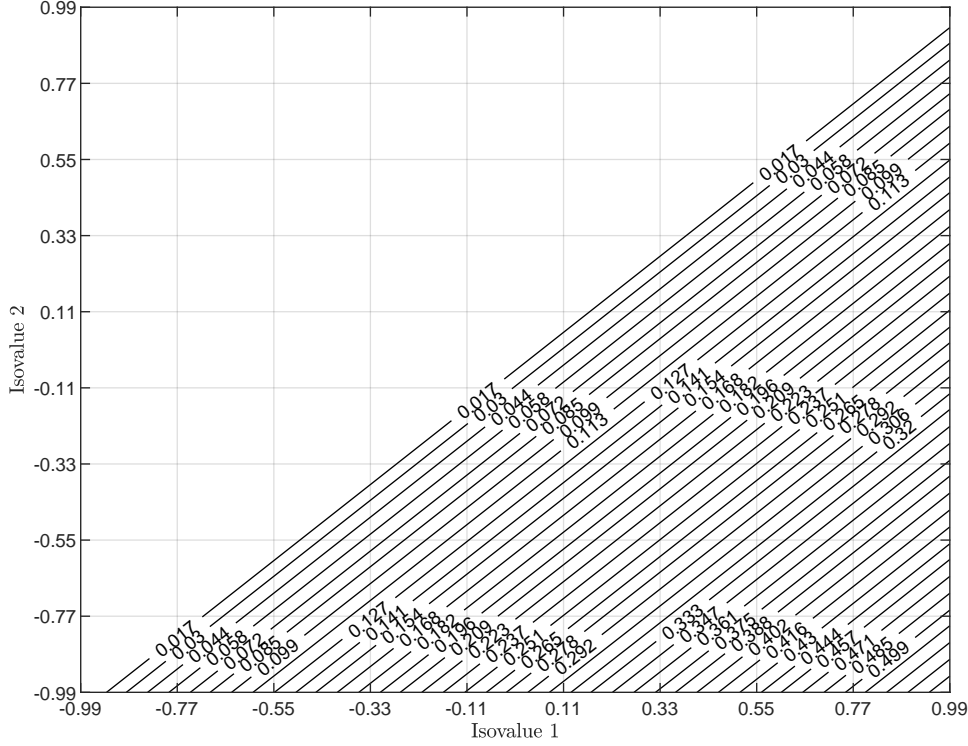


Figure 5.17: Contour plot showing volume fractions for all possible isovalue combinations for Primitive. This plot is presented as an example of a look-up chart to facilitate obtaining a volume fraction value for a specific isovalue pair. The contour plots for the other TPMS and other geometric properties are provided in the data archive [259].

volume fraction as the inner and outer surfaces can be set to the same isovalue. Just as for the single surface structures, the Gyroid has the largest possible range of volume fractions, and the Neovius has the smallest range.

### 5.5.2 Surface Area

The surface area for all single surface TPMS structures has a single maximum at or near an isovalue of 0 (Figure 5.19). Conversely, for symmetric double surface structures, the surface area decreases monotonically as the magnitude of the isovalues increase (Figure 5.20). For both double and single surface structures at low absolute isovalues, the Diamond structure has the highest surface area and the Primitive the lowest. For the highest magnitude isovalues, the Neovius has the highest surface area and Gyroid the lowest. For applications, such as heat transfer, maximising surface area is highly desirable. Considering this in isolation, the Diamond, Neovius and iWP structures are best suited.

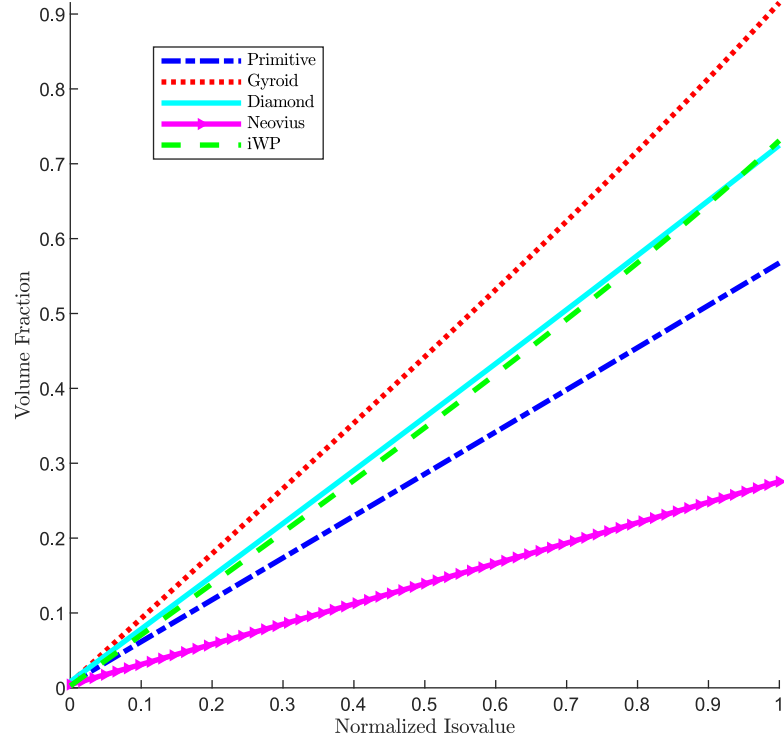


Figure 5.18: Comparison of the volume fraction as a function of normalised isovalue for all double surface TPMS structures, showing almost linear dependence. This plot shows the normalised subset of isovalue combinations for  $f(x, y, z) = \pm c$  to compare the TPMS. Normalised isovalues can be converted to isovalues by dividing by the normalisation factor given in Table 5.1.

### 5.5.3 Minimum Thickness

The minimum thickness for both the single surface and symmetric double surface TPMS structures monotonically increase as the isovalue increases (Figures 5.21 and 5.22). Contour plots for the minimum thickness for all double surface structures are provided in the data archive [259]. The non-linearity of the minimum thickness as a function of isovalue demonstrates that the TPMS structures do not isotropically expand as the isovalue increases.

Just as with the volume, the Gyroid structure has the largest range of thicknesses and the Neovius structure has the lowest. In the case of the single surface structure, the Primitive structure has a similar range to the Gyroid structure. All minimum thickness functions almost converge at the lowest isovalue. For small lattices, the Neovius structure will be hardest to manufacture due to the consistently low minimum thickness for the entire isovalue range.

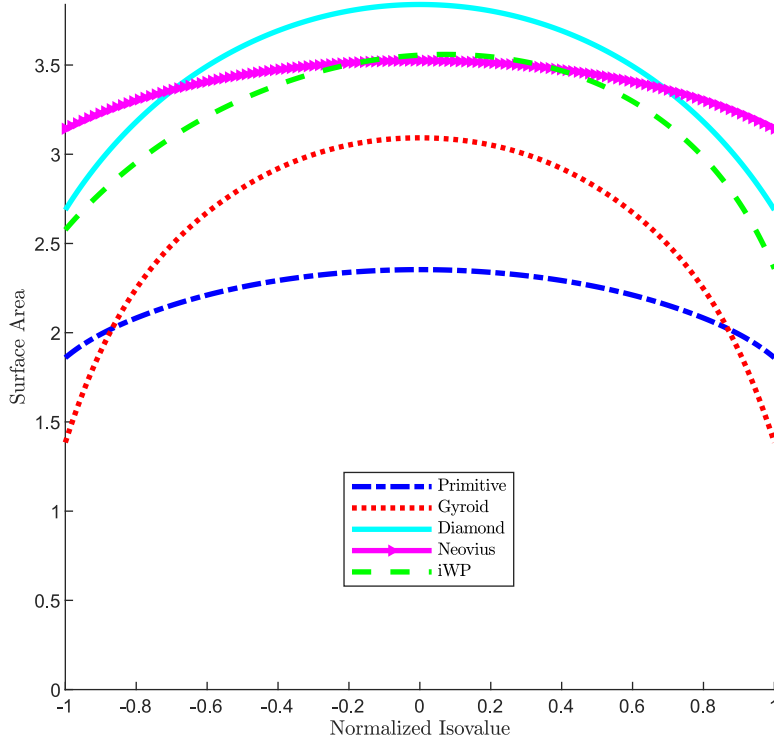


Figure 5.19: Comparison of the surface area as a function of normalised isovalue for all single surface TPMS structures, showing parabolic dependence. Normalised isovalues can be converted to isovalues by dividing by the normalisation factor given in Table 5.1.

## 5.6 Discussion

The full value of the presented work is in the ability to further manipulate the results. By combining the above geometric properties it is possible to calculate other physically meaningful properties. As an illustrative example, consider the SAVR. There are numerous engineering disciplines that require high SAVR geometries, such as heat exchanger design, filtration, etc. For a single surface TPMS structures, Figure 5.23 clearly shows that the SAVR is maximised by selecting the Gyroid at lower isovalues. However, these low isovalues may lead to excessively thin structures. At high isovalues, the Neovius structure has the highest SAVR, but, as previously mentioned, the Neovius has low minimum thicknesses for all isovalues. This example further demonstrates the counter-intuitive nature of the isovalue. With the provided datasets, it is possible to program more complex constraints such as maximising the SAVR while ensuring that the minimum thickness stays above a given limit.

To illustrate the way in which these geometric properties feed into engineering and physical properties, the heat exchanger example is continued. The work of Cowell *et al.* [260] proposes a means of comparing different surfaces in terms of performance in a heat transfer application. Key parameters in this method

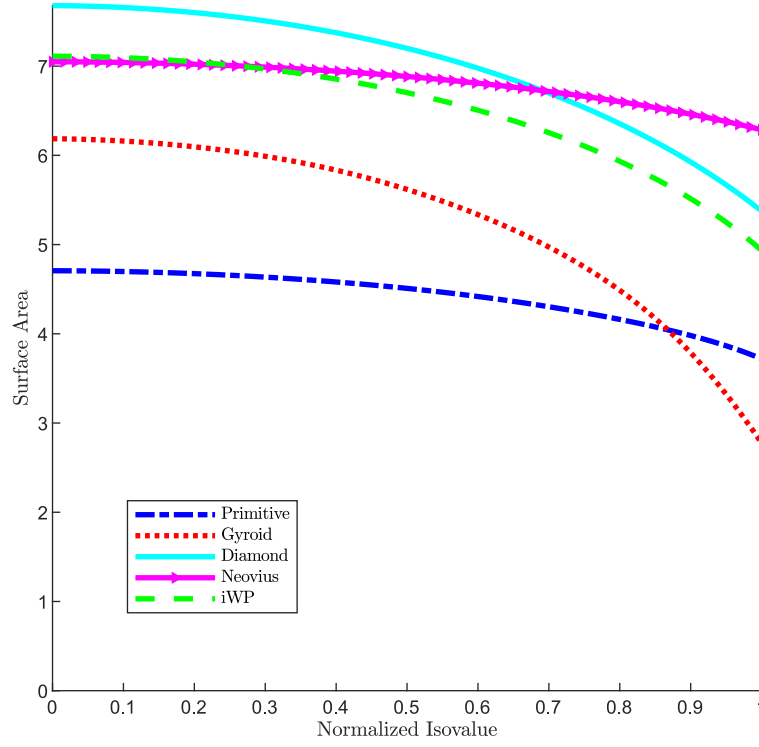


Figure 5.20: Comparison of the surface area as a function of normalised isovalue for all double surface TPMS structures, showing surface area monotonically decreasing with the normalised isovalue. This plot shows the normalised subset of isovalue combinations for  $f(x, y, z) = \pm c$  to compare the TPMS. Normalised isovalue can be converted to isovalue by dividing by the normalisation factor given in Table 5.1.

include the hydraulic diameter,  $d$ , and the ratio of minimum free-flow to frontal area,  $\sigma$ . These are defined as per

$$d = \frac{4\sigma V}{A_s}, \quad (5.18)$$

$$\sigma = \frac{A_c}{A}, \quad (5.19)$$

respectively. Here,  $V$  is the volume of the heat exchanger core,  $A_s$  is the area available for heat transfer,  $A_c$  is the minimum free-flow area and  $A$  is the frontal area of the heat exchanger core. Taking, as others have, multiple TPMS unit cells as a two-fluid heat exchanger core, all of the above parameters are either specified or can be derived from the dataset.  $A_s$  requires the surface area of the chosen unit cell to be scaled to the correct size and then multiplied by the number of unit cells in the core.  $A_c$  can be calculated by multiplying  $A$ , which is known, by the porosity,  $\sigma$ , of the core, which is directly related to the volume fraction.

All data presented have a generously estimated uncertainty of 1% given the convergence tolerances. The accuracy of the dataset as a whole is on average much



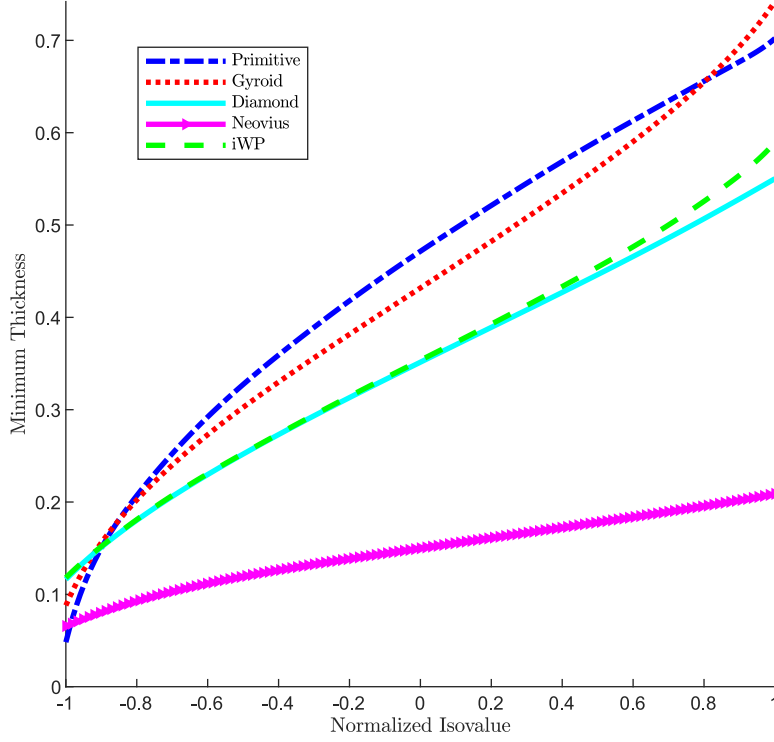


Figure 5.21: Comparison of the minimum thickness as a function of normalised isovalue for all single surface TPMS structures, showing the minimum thickness monotonically increasing with the isovalue. Normalised isovalues can be converted to isovalues by dividing by the normalisation factor given in Table 5.1.

greater than this as two further iterations are calculated after initial convergence. However, it is not possible to guarantee this higher accuracy for all values. The technical limitation preventing tighter convergence tolerances were the memory limitations in MATLAB 2019a, limiting maximum array sizes to 6550 MB. This hinders further convergence for the surface area and minimum thickness calculations as the matrices become exponentially larger with each iteration.

Further uncertainty is introduced by the discrete nature of the numerical sampling. However, due to the dense sampling, low residuals, and the robust nature of the Chebyshev fitting method, this has not increased the estimate of the uncertainty. The data are sufficiently accurate for most practical applications. If cases arise where greater accuracy is paramount, the methods are described, and the original MATLAB code is provided in such a way that the work can be replicated and extended by others.

This work in this chapter addresses the first research gap identified in Section 2.4.3. As there was no straightforward method for creating TPMS structures to a certain geometric specification, this led to divergent methods to add volume to the TPMS mathematical surfaces therefore leading to discrepancies in the structures created. The approach of this work complements the majority of the reviewed work that used isovalues to manipulate the TPMS functions to model TPMS

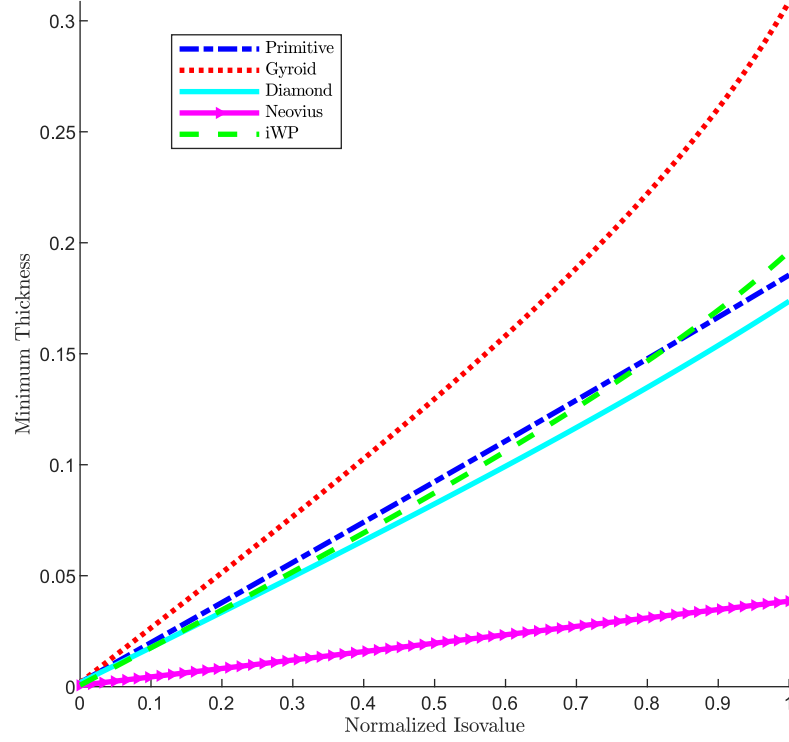


Figure 5.22: Comparison of the minimum thickness as a function of normalised isovalue for all double surface TPMS structures, showing the minimum thickness monotonically increasing with the isovalue. This plot shows the normalised subset of isovalue combinations for  $f(x, y, z) = \pm c$  to compare the TPMS. Normalised isovalues can be converted to isovalues by dividing by the normalisation factor given in Table 5.1.

structures as this is a controlled method when using implicit-based modelling. The research contributions of the set of numerical methods, the MATLAB program, raw datasets, and the empirical geometric relationships provide the link between the isovalues and the resulting geometric properties.

As mentioned in Section 2.4.3 there are other groups that have also related calculated geometric properties of TPMS structures with varying isovalues graphically with some also providing regression models [10, 12, 196, 198, 203, 219, 220]. In comparison, some other research groups have produced visually similar plots for the same TPMS structures for volume fraction and surface area calculations [10, 12]. This work, however, provides a method for calculating the geometric properties that quantify the accuracy of the datasets. Much of the literature has limited information of calculation methods and the respective uncertainties. Additionally, any calculation of minimum thickness property has not been found in the reviewed literature. Furthermore, these datasets have resulted in the formulation of robust empirical models that can be readily implemented into CAD packages. Due to the orthogonality of the Chebyshev polynomials the coefficients can be compared to truncate insignificant higher order terms. This benefit is ab-

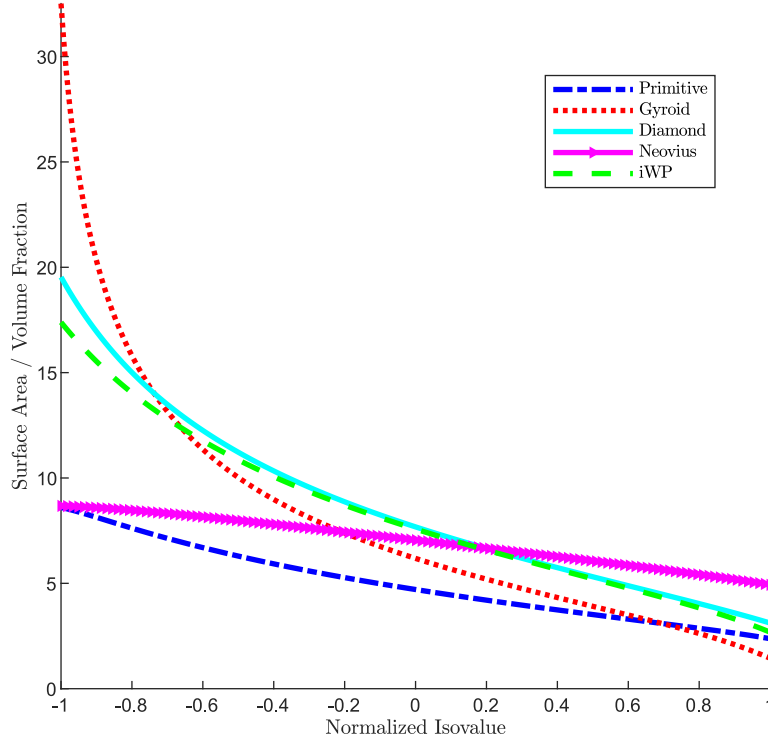


Figure 5.23: Comparison of SAVR as a function of normalised isovalue for all single surface TPMS structures, showing the SAVR monotonically increasing with the isovalue. This is an example of how the geometric properties can be combined. Normalised isovalues can be converted to isovalues by dividing by the normalisation factor given in Table 5.1.

sent when using standard polynomial fitting. The regression models found in the literature provide limited information regarding the fitting and associated residuals as well as discrepancies between each other. While the research contributions can be readily used as is, the methods can be expanded to other TPMS structures or accuracy tolerances.

## 5.7 Conclusion

This research has produced empirical relationships for the geometric properties of prevalent TPMS structures, numerical methods to expand to other implicitly defined TPMS structures, and an openly-available dataset for geometric properties of prevalent TPMS geometries. It therefore represents the first meaningful step towards enabling designers to confidently control the shapes they are creating and will help prevent unforeseen failure during the additive manufacture of components. Furthermore, by providing an empirical relationship between mathematical parameters and the resulting geometric properties, this increases the accessibility

of designing with these geometries, the importance of which is evident in the increasing body of related research.

It should be noted that geometric properties are a fundamental consideration when designing. These further feed into engineering and physical properties, such as compressive strength, permeability, overall heat transfer coefficient, and many more. These geometric properties to further enable the work of those researching engineering and physical properties.

The relationships established serve as the keystone in the next phase of this thesis to develop methods to print geometrically customised TPMS structures. The development of toolpath algorithms are elaborated in the next chapter.

# Chapter 6

## Adaptive Direct Slicing of TPMS Structures

### 6.1 Introduction

CAM software, also commonly referred to as toolpath planner software or slicer software, converts a digital 3D model into machine code for an AM machine. The machine code controls the machine's motion, such as material extrusion, and other auxiliary functions. This is typically done by importing the 3D model surface in a mesh-based file format, such as a STL file. The imported model is edited by the user by adjusting the size dimensions, infill, number of printed parts, location on the printer bed, part orientation, and other printing options, such as support structures. The printing options generally depend on the type of 3D printing and software product. When the editing phase is finished, the part is "sliced", where the 3D model is segmented into layers (parallel to the printer bed) along the vertical,  $z$  axis, where the layer thickness is based on the resolution of the deposition or consolidation of feedstock material. The slices are then ready to be translated and exported as machine code. The 3D printer used in this study is programmed using GCode, the universal machine code for 3D computer-aided manufacturing. This process flow is shown in Figure 6.1.

Although it is not necessarily visible to the user, the CAM software will be deploying a range of algorithms and decision making logic to create the final GCode output. This is not only calculating the toolpath but also the speed, acceleration, extrusion/laser power, and other functionality such as the fan, printing sacrificial supports, etc. In addition to controlling the auxiliary functions of the machine, the GCode program communicates a sequence of destination points that that extrusion head must move to. In the vast majority of cases, the extrusion head moves between destination points using straight line interpolations. It is typical for these destination points to firstly describe the outer shell or perimeter of the printed object. After this, the destination points describe the infill that sits within the boundary. This infill can either be completely solid, or some infill pattern that forms a lighter scaffold within the outer shell. There are other

destination points that are used to describe various forms of support for the print. These include sacrificial supports, rafts and brims to anchor the object to the build plate, or support overhanging faces. It is worth noting that different print settings may be applied to different regions of the print. For example, sacrificial support and infill often adopt different settings to the outer shell of the object. These toolpaths are calculated depending on the type of CAM software. Most calculate based on Euclidean set operations and explicit functions, however, recently there is newer research that calculate toolpaths based on implicit functions [16, 19, 162, 163, 165, 229].

There are multiple inherent differences to how traditional commercial and implicit CAM softwares work. Traditional software workflows typically begin with the 3D model as a triangulated mesh with built-in infill options described by explicit functions. Conversely, implicitly-based software describes 3D models using implicit functions of shapes and describe surfaces based on the function isovalue contours. This opens up the possibility of using shapes based on mathematical functions that would otherwise be challenging to produce in traditional CAD software using parametric surfaces. TPMS are an example of this type of challenging shape. Directly slicing the surface structures from implicit functions streamlines the process flow. This eliminates the incompatibility of parametric kernels for cre-

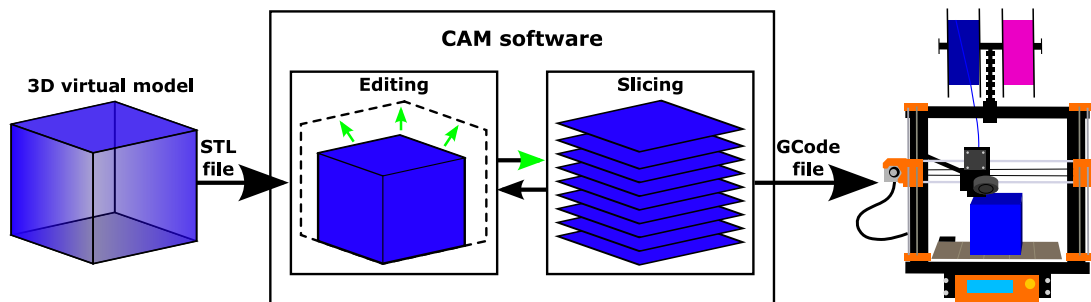


Figure 6.1: General process flow for the CAM stage for FDM. A 3D model is imported into the CAM software. The model is then edited, print settings adjusted, and sliced. The slices are exported as a GCode file to the AM machine which then manufactures the part.

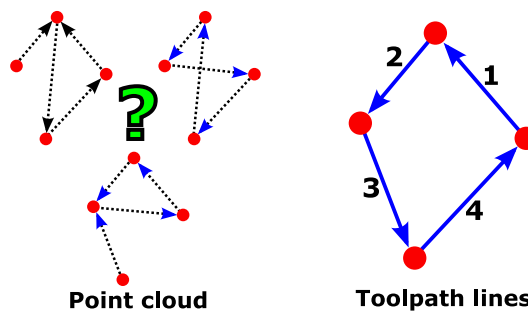


Figure 6.2: A toolpath needs instruction in the form of a line such that it is not ambiguous how to connect coordinates.

ating boundary representations (BRep) as well as the intermediary mesh-based file formats, such as STL files.

To manufacture geometrically customised TPMS structures based on the relationships from Chapter 5, ideally an implicit-based CAM software would be used. Using the TPMS implicit functions is optimal as solving each of the TPMS function into explicit functions is often non trivial. The explicit forms have multiple solutions as the TPMS functions are a combination of trigonometric functions. The challenge is that of the available software either commercially or from research does not have the functionality needed for the aim of this research. A CAM program was then developed in MATLAB to print geometrically customised TPMS structures based on implicit functions. The software creates GCode using input geometric specifications based on a direct slicing method. The novelty of this method is that it not only can controllably create TPMS structures to design specification but also the internal toolpaths are adaptively calculated based on the user's input of the TPMS type, structure type, and outer shape dimensions using the geometric relationships from Chapter 5. Rather than using a solid hatching infill for thickened lattice structure, this software creates toolpaths based on the same TPMS implicit function evaluated at intermediary isovalues, also known as isolines or contour lines. This program is a means to not only print geometrically customised TPMS structures but also as something that could easily be adapted as an infill option into a traditional commercial or implicit CAM software.

## 6.2 Investigating Current Infill Techniques

Before developing the CAM program, the PrusaSlicer Gyroid infill option was investigated. PrusaSlicer is an open source CAM software from the Prusa company [261, 262]. This was to understand the Gyroid infill toolpath algorithm and what information the machine needs to print. The goal is to be able to describe customised TPMS surfaces using toolpath lines rather than a point cloud as 3D printers need toolpath instructions to print. Without any instruction as to where the surface is within a point cloud, connecting the points could be ambiguous as shown in Figure 6.2.

Currently, the Gyroid infill is default infill option in the PrusaSlicer software user interface. The infill is a Gyroid structure with one filament thickness. It can be only customised by a volume percentage that changes the number of lattice unit cells, increasing the infill volume as the number of lattice unit cells increase. As of now, there is no way to thicken the Gyroid infill more than one filament thickness. The C++ source code was translated into a MATLAB environment. In the source code, the Gyroid infill is calculated using the explicit form, shown below

$$y = -\arcsin \frac{\sin(2\pi z) \cos(2\pi x)}{\sqrt{\cos(2\pi z)^2 + \sin(2\pi x)^2}} \pm \arcsin \frac{\sin(2\pi x)}{\sqrt{\cos(2\pi z)^2 + \sin(2\pi x)^2}} \quad (6.1)$$

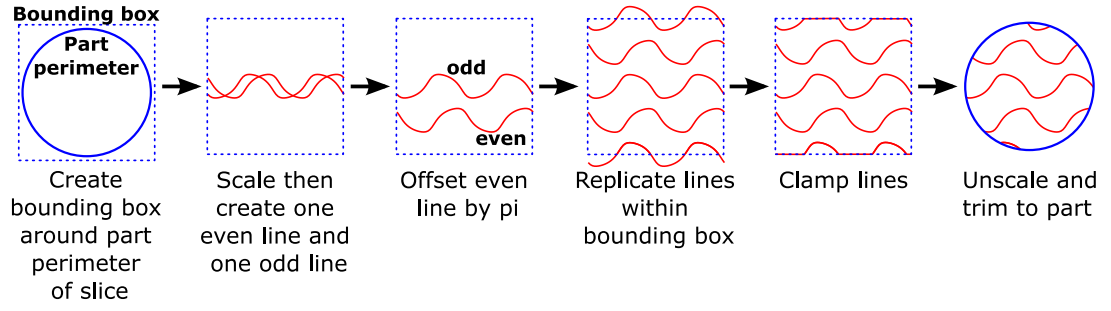


Figure 6.3: The process for creating Gyroid infill toolpaths for a slice in PrusaSlicer. A bounding box is created around the 3D modelled part, then the box is filled with Gyroid infill. The periodicity of the Gyroid lines are based on the input volume fraction from the user. The infill is then trimmed to fit within the inner perimeter of the part. While the diagram depicts only two periods of each Gyroid line, in the program the periodicity, i.e. the number of lattice unit cells, is based on the designer input volume fraction.

where  $x, y, z$  are the Euclidean coordinates relative to the printer bed. The equation is for the pure Gyroid TPMS function where the isovalue is equal to zero. The explicit form containing an isovalue would separately need to be solved. The  $y$  values are calculated by inputting a range of  $x$  values at the slice height, i.e. the  $z$  value, into the Equation 6.1. As the explicit function elicits multiple solutions, the correct solutions are dependent on the parity and the  $z$  height.

The infill algorithm first calculates a bounding box, a scale factor, and the number of lattice periods. The bounding box that encompasses the entire volume of the 3D model of interest. The scale factor is the scalar relationship between the length dimensions of the print bed, in mm, to the dimensionless mathematical scaling of the lattice from  $[0, 2\pi]$ . After scaling to the lattice dimensions, the algorithm then creates Gyroid lines per slice. First, by calculating one period of a single Gyroid wave line for each of the even and odd solutions. The even Gyroid line is then offset by  $\pi$ . The two lines are repeated until the bounding box is filled and the parts of the lines that equate to outside of the box are “clamped” such that they are forced to equal the sides of the box. The lines are then unscaled and fitted to the 3D model to become the toolpath for the 3D printer. A schematic showing this toolpath creation method for a slice is shown in Figure 6.3.

While the explicit function equates to exact solutions and is computationally efficient, for this research this is an unrealistic approach. As mentioned previously, each TPMS implicit function with an isovalue needs to be converted into the explicit form. As discussed in Chapter 5, it is non-trivial solving for the explicit form and the correct roots. As such, a toolpath algorithm was developed that uses TPMS implicit functions to create toolpaths.



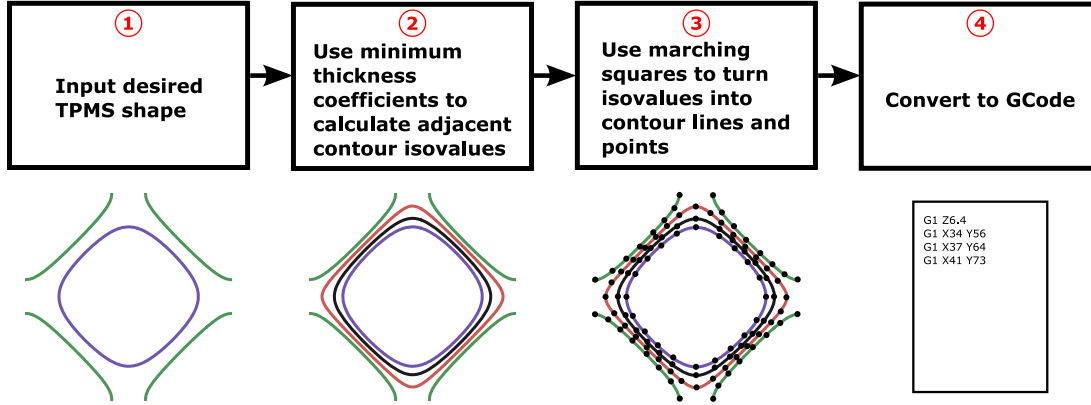


Figure 6.4: The direct slicing toolpath algorithm follows four steps. The algorithm starts by calculating the isovalues for the desired TPMS shape using the relationships from Chapter 5. Then adjacent contour isovalues are calculated. After all isovalues are obtained, the contour lines are calculated per slice. The contour lines are then converted into GCode for the AM machine.

## 6.3 Direct Slicing Toolpath Algorithm

The developed direct slicing toolpath algorithm uses input specifications for a TPMS structure and outputs a GCode file. The algorithm has four steps outlined in Figure 6.4. Based on the inputs, the algorithm calculates the isovalues for the desired TPMS structure using the relationships from Chapter 5. From there, the inset filler isovalues of adjacent contour lines are calculated using the double surface structure minimum thickness polynomial coefficients. After all isovalues are calculated, the algorithm then calculates the toolpaths on a slice-by-slice basis. For each slice, the contour lines and points are calculated from the isovalue using the marching squares algorithm. The lines are then prepared and translated into GCode for the machine.

### 6.3.1 Customised TPMS Structure Inputs

The algorithm calculates contour line toolpaths using isovalues. Before this, all necessary isovalues need to be calculated. The two types of isovalues are perimeter isovalues and filler isovalues. The perimeter isovalues define the perimeter contour of the TPMS structure and the filler isovalues are the inset contours. The perimeter isovalue calculation is based on the work from Chapter 5. The algorithm always requires the inputs of a TPMS type, structure type (isoline, single surface structure, or double surface structure), number of lattice unit cells, and the outer box length dimension (mm).

For customising the TPMS shape, there are two types of input options implemented into the CAM program. The first option is to input isovalue(s) to be directly translated into contour line toolpaths. The other option is to input a geometric specification (volume fraction, surface area, or minimum thickness). The algorithm will automatically calculate all needed isovalues using the geomet-

ric relationships from Chapter 5. This algorithm is an efficient method to create geometrically customised TPMS structures to help designer develop parts. This algorithm can be expanded to calculate isovalues for compound geometric specifications, i.e. SAVR, for design applications, such as the heat exchanger example discussed in Section 5.6.

Before calculating the perimeter isovalues, the shape inputs are transformed from the printer dimensions to one unit cell of a unitless TPMS. This is to be able to use the geometric relationships from Chapter 5 which were established for unitless TPMS. The scaling factor is defined by

$$s = \frac{n}{L} \quad (6.2)$$

where  $s$  is the scale factor,  $n$  is the number of lattice unit cells, and  $L$  outer box length is in mm. Then, the perimeter isovalues needed to give the desired geometric properties to the output lattice are calculated using the relationship coefficients. As the relationships from Chapter 5 are polynomial equations, defined by Equations 5.16 and 5.17, the isovalues are determined by finding the roots of the equation. In the program, the isovalues are calculated using the MATLAB built-in function `roots` which calculates the eigenvalues of the companion matrix. As there will be multiple solutions, only the real solution within the lattice isovalue range, defined in Table 5.1, is valid for this purpose. For double surface structures, this can result in infinite solutions. Therefore, the program was constrained to a subset of isovalue combinations for  $f(x, y, z) = \pm c$ , where  $c$  is the isovalue.

As the polynomial models from Chapter 5 are based on isovalues that are infinitely thin, if the perimeter isovalue(s) are printed as is, the part will be thicker than expected. Therefore, the perimeter isovalue(s) are brought inwards by the nozzle diameter as illustrated in Figure 6.5. The adjustment calculation uses the double surface structure minimum thickness relationship. The adjusted isovalue is calculated by setting an adjusted minimum thickness as the theoretical minimum thickness minus the nozzle diameter.

### 6.3.2 Calculate Adjacent Contour Isovalues

The inset filler isovalues are calculated with the double surface structure minimum thickness relationship from Chapter 5. This ensures that the closest distance between adjacent contour lines is the nozzle diameter. This method is a controllable way of calculating adjacent toolpath lines such that they are not too close causing the print to fail. As this uses the nozzle diameter as the minimum thickness and a known isovalue, the double surface structure coefficients are needed to calculate the next adjacent isovalue.

Before calculating the filler isovalues, the number of filler isovalues are calculated as there will need to be an integer number of toolpath lines. This is based on the nozzle size and the minimum thickness of the TPMS structure defined by the perimeter isovalue(s). For double surface structures, this is between the two

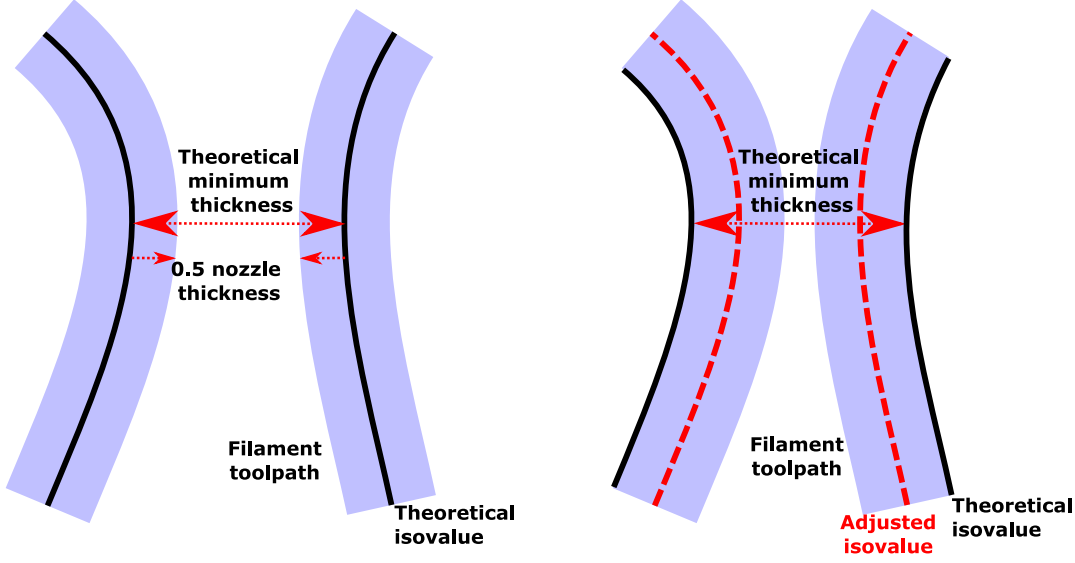


Figure 6.5: Adjusting the perimeter isovalues inwards to account for the nozzle size.

perimeter isovalues. For single surface structures, this is between the perimeter isovalue and the maximum isovalue of the lattice isovalue range from Table 5.1. The number of filler isovalues is calculated using

$$N = \left\lfloor \frac{T}{d} \right\rfloor, \quad (6.3)$$

where  $N$  is the number of filler isovalues,  $T$  is the unitless minimum thickness, and  $d$  is the unitless nozzle diameter (scaled using scaling factor from Equation 6.2). This equation uses the floor function to ensure an integer number of isovalues.

The adjacent isovalues are then iteratively calculated using the relationship coefficients. Each adjacent isovalue is calculated by setting the minimum thickness as  $\frac{d}{N}$  and one isovalue as the known isovalue. The known isovalue starts with the smallest perimeter isovalue, then with each iteration becomes the solved isovalue from the previous iteration. This is done until  $N$  filler isovalues are obtained. The calculated adjacent isovalues are verified by checked they are within the isovalue range of the perimeter isovalues as well as the initial calculation of the integer number of filler isovalues ensures the correct number of filler isovalues. This was further validated with test printing different TPMS structures with varying TPMS type and structure types.

The minimum thickness relationship from Chapter 5 is used to calculate adjacent toolpath lines based on the nozzle diameter. However, in the program, they are set closer than the nozzle diameter to help compensate for the thickness distribution of TPMS structures. If adjacent toolpath lines are set too close this can cause unwanted build-up leading to print failure, as shown in Figure 6.6. The minimum thickness was set to 0.35 mm instead of the nozzle size 0.4 mm as this visually did not create build up.

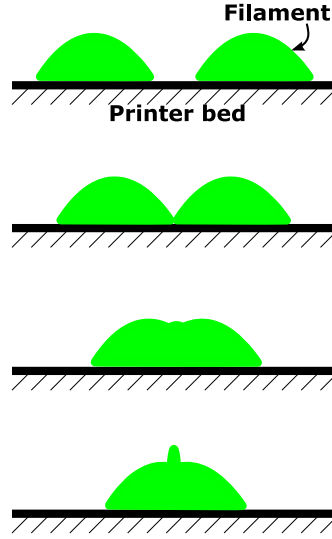


Figure 6.6: Cross-section view of different spacing between adjacent filament ranging from adjacent filament with space between (top) to adjacent filament too close with build-up (bottom).

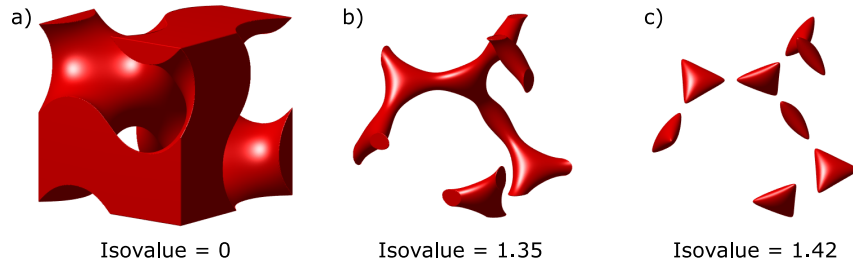


Figure 6.7: Example of a Gyroid single surface structure set to different isovalues. (a) shows the Gyroid set to an isovalue of 0, (b) shows the Gyroid set to an isovalue of 1.35 (maximum lattice isovalue range), and (c) shows the Gyroid set to 1.42. The Gyroid surface beyond the lattice isovalue range until  $f(x, y, z) = \pm 1.5$  is not considered a lattice. Beyond  $f(x, y, z) = \pm 1.5$ , the Gyroid surface does not exist.

For single surface structures, the adjacent filler lines are calculated from the input isovalue to the maximum limit of the lattice isovalue range. Beyond the lattice isovalue range, as the isovalue increases, TPMS become disconnected smaller surfaces before ceasing to exist altogether as shown by Figure 6.7. Hatched solid infill lines are calculated for the region where the surface exists but is beyond the lattice isovalue range. Figure 6.8 shows double and single surface structure Gyroid printed parts with the perimeter, filler, and solid infill lines labelled.

Finally, when both the perimeter and filler isovalues are calculated they are sorted into the order they will be printed. To help stabilise the print, the sorted isovalues start with the isovalue closest to the pure TPMS, then followed by each subsequent adjacent isovalue.

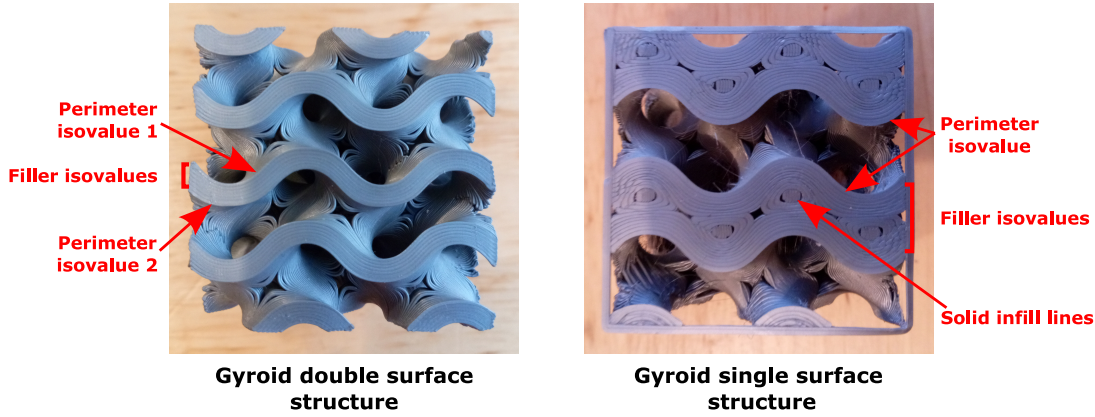


Figure 6.8: Labelled photograph of line types on a Gyroid double surface structure and single surface structure. The perimeter isovalue lines and filler isovalue lines are labelled on both and the solid infill lines where the lattices ceases to exist are labelled on the single surface structure.

### 6.3.3 Calculate Contour Lines Per Slice

After obtaining all isovalues, the program then calculates the contour lines and translates them into GCode on a slice-by-slice basis. The number of slices is based on the input box length and the nozzle size. To calculate the contour lines, the algorithm needs the isovalues, the TPMS implicit function, and the TPMS gradient function.

The 2D marching squares algorithm was used to extract the contour lines per slice. The marching squares algorithm is a robust algorithm for extracting contour lines from implicit functions as previously explained in Section 2.4.1. The program uses the MATLAB built-in function `contourc`, which requires the inputs of an  $[x, y]$  grid, the corresponding function value matrix, and the isovalues. The function value matrix is calculated from the  $[x, y]$  grid at the  $z$ -height, i.e. slice height, using the TPMS implicit function. The program uses uniformly spaced  $100 \times 100$   $[x, y]$  grids. The MATLAB marching cubes algorithm has a grid resolution limit as shown by the asymptotic curve in Figure 6.9. The plot shows  $[x, y]$  grids resolutions beyond  $100 \times 100$  do not change the order of magnitude of the maximum function value error.

Once the contours have been estimated, the contour points are corrected for the marching squares resolution limit, using the Newton-Raphson method outlined in Chapter 5. The Newton-Raphson method corrects the points onto the contour to machine precision. This is done with a fixed  $z$  to ensure all points stay on the same slice. Without this correction, the error is visibly noticeable on printed parts, as shown in Figure 6.10.

Once the contour lines have been calculated, the points are transformed back to the printer coordinates. The lines are then checked for invalid values, such as negative  $z$  or NaN values, as they will cause the machine to crash if included in the GCode file. Certain programming languages, such as MATLAB, when performing calculations that result in invalid values, do not error and continue running by

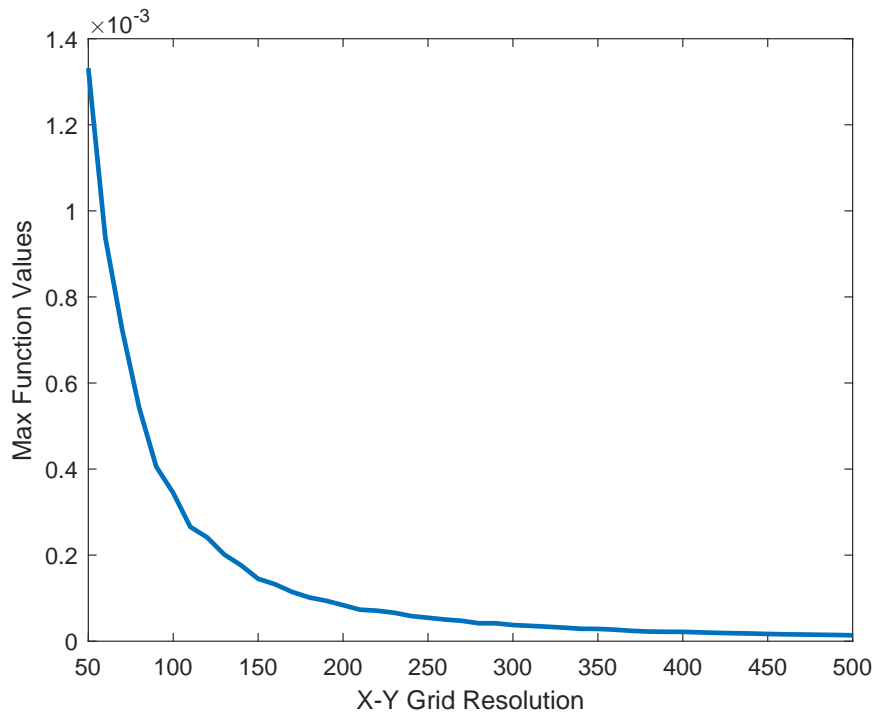


Figure 6.9: Maximum function value of contour points created by MATLAB `contourc` for a Gyroid isovalue of zero vs. the  $[x, y]$  grid resolution. The maximum function value denotes the maximum error as contour points should evaluate to zero.

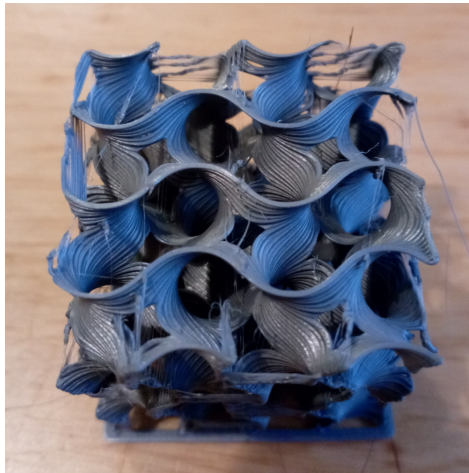
including NaNs values. Also, a check is needed for negative  $z$  values as the printer can travel in the negative regions of the print area. The lines are then translated to the starting coordinates on the printer bed.

The contour lines are reorganised such that as one line finishes printing it will start at the nearest endpoint of the nearest contour lines that has not been printed. This optimises the path for print time as this removes unnecessary time where the printer is moving between printing lines. This means flipping the contour line coordinate order if the endpoint is nearest, an example is shown in Figure 6.11. After the contour lines are reorganised, they are converted into GCode.

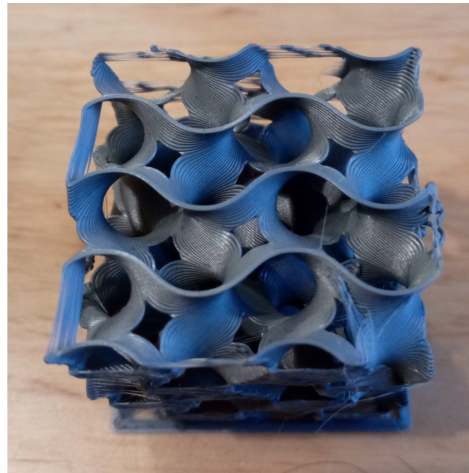
### 6.3.4 Convert To GCode

After the contour lines are created, they are translated into GCode strings on a slice-by-slice basis. After all slices are translated, the GCode file is prepared and exported. An example Prusa GCode file was parsed to establish the machine codes for print commands and auxiliary functions.

Brim and wiping features were added to the GCode as they help improve accuracy and help prevent print failure. The brim is extra filament lines that surrounds the perimeter of the part on the first layer, as shown in Figure 6.12. The first layer is susceptible to peeling, especially in the vicinity of corners. This



Before Newton-Raphson correction



After Newton-Raphson correction

Figure 6.10: Photograph of printed Gyroid parts showing before and after the Newton-Raphson correction was implemented. As the marching squares algorithm is only an estimate of the surface, Newton-Raphson corrects the estimated coordinates onto the surface for each slice. The “after” picture on the right side shows the Gyroid is visibly smoother.

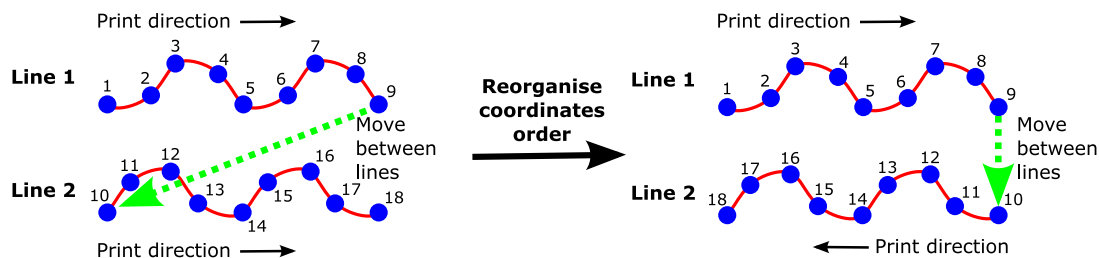


Figure 6.11: Reorganisation of contour line coordinate print order. The numbered coordinates indicated the order they will be printed. The second line coordinate order is flipped as the original endpoint is closest to the endpoint of the first line.

is because the hot filament shrinks as it cools. Wiping is also necessary to improve accuracy and prevent print failure. When the printer finishes printing a line there is residue filament at the tip of the nozzle. Wiping retraces the line backwards for a short distance while negatively extruding. Without wiping, the print quality is visibly reduced and can cause failure. Figure 6.13 shows the same print of a Gyroid before and after the wiping feature was incorporated.

After the GCode file is outputted, there is an optional program to simulate the print. This is to help visualise and troubleshoot before printing to save time, material, and help prevent failures. After the CAM program generates an output GCode file, the simulation program imports the GCode file, parses it, and plots each slice layer. Each slice is plotted one at a time with each line printing in order as it would on the 3D printer in reality, pausing between each line. Each “printed” layer is superimposed on all the preceding layers. The toolpath lines are plotted in green and the movements without extruding filament are plotted



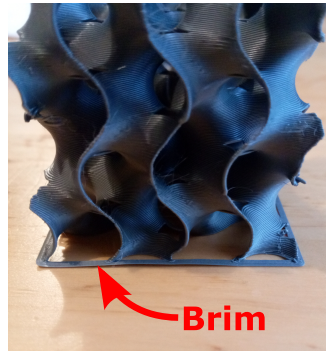


Figure 6.12: Photograph of a printed brim surrounding the perimeter of a Gyroid part on the first layer.

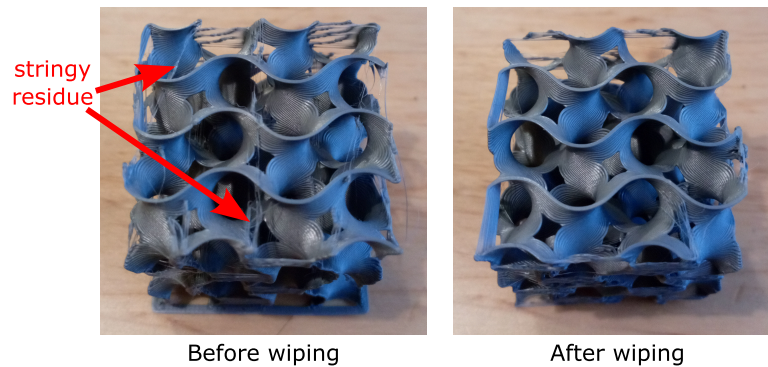


Figure 6.13: Photograph of before and after the wiping feature was incorporated.

in red. This is a top-down perspective of the  $x, y$  print bed, as shown in Figure 6.14.

## 6.4 Discussion

### 6.4.1 Streamlined AM Process Flow

Designing geometrically customised TPMS structures using conventional process flows requires either using CAM infill options or modelling the lattice in CAD. Infill is an efficient method for creating lattices for AM, however, the customisation options are very limited. Alternatively, CAD has many customisation options, however, modelling lattices is computationally limited due to mesh-based modelling. This direct slicing toolpath algorithm is a streamlined method for efficiently creating geometrically customised TPMS structures as infill. As such, this algorithm uses the best features of the two types of conventional process flows for AM lattices addressing the second gap found in the literature in Section 2.4.3. The research contribution is a toolpath algorithm for creating geometrically customised TPMS structures that can be adapted as an infill option in commercial CAM software.



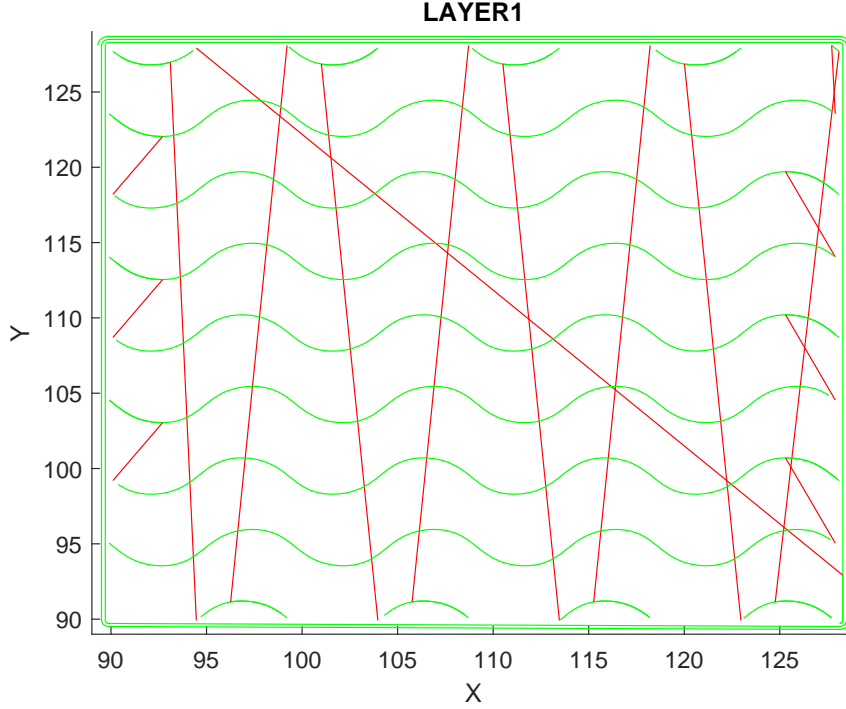


Figure 6.14: Plot showing an example display of the simulation print produced from a GCode file. This is a top-down perspective of the first layer of a Gyroid with  $4 \times 4 \times 4$  lattices unit cells. The green lines are the toolpath lines the printer is extruding and the red lines are where the printer is moving but not extruding. The green box lines around the perimeter are the brim.

Direct slicing methods are also seen in the literature by Ding *et al.* and Feng *et al.*. Both used TPMS implicit functions to directly create GCode for AM machines. Ding *et al.* uses the TPMS function to calculate the contour of TPMS on a slice-by-slice basis for particular isovalues [16]. The contour is then used to essentially cut out solid infill lines into the TPMS shape. They adapt the TPMS structures for the number of unit cells, hybrid TPMS structures, wall thickness gradients, and TPMS structures within TPMS structures. Feng *et al.* use the TPMS functions to create toolpaths then generate equidistant adjacent toolpath lines [229].

Rather than using solid infill lines or equidistant adjacent lines to create uniformly thick structures, this algorithm uses adjacent TPMS contour lines. As TPMS have been shown to have strong mechanical properties [12], this algorithm creates TPMS structures made of nested TPMS structures. The adjacent contour lines are controllably calculated using the minimum thickness relationships from Chapter 5. This ensures that adjacent contour lines are not too close to cause print failure. Also by using contour lines as toolpaths, this reduces the print time as there are less lines to print compared to solid infill, as shown in Figure 4.6.

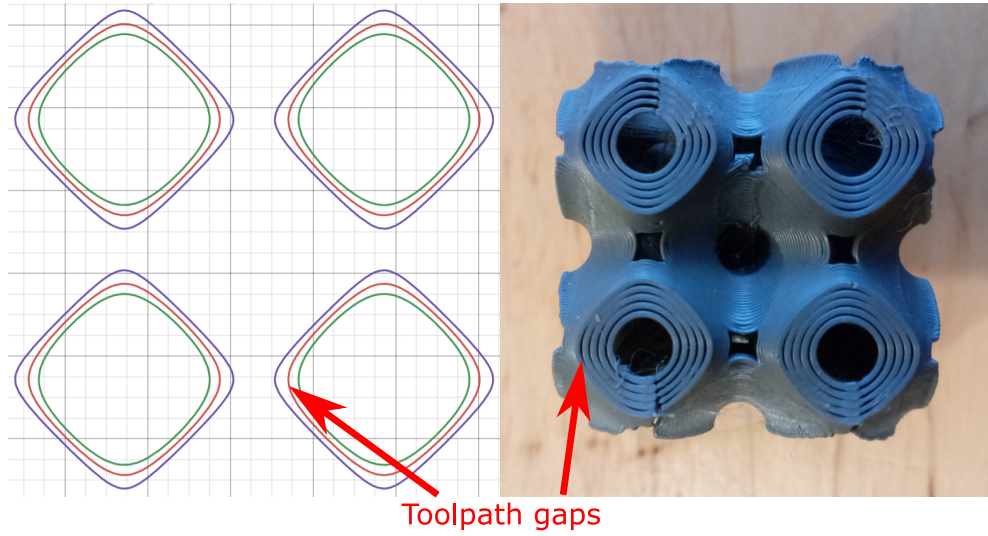


Figure 6.15: Comparison of the mathematical function for Primitive with three varying isovalues using the graphing tool Desmos and a printed Primitive structure. The gaps between the adjacent contour lines match between the mathematical function and the printed specimen.

The algorithm can create TPMS structures based on a geometric specification, i.e. volume fraction, surface area, or minimum thickness. This is done by calculating toolpaths using the relationships from Chapter 5. Using the work from this chapter built on the work from the previous chapter results in a meshless alternative process flow. This process flow allows designers to create customised TPMS structures without the need for inefficient mesh-based modelling or arduous mathematical calculations.

## 6.4.2 Opportunities for Continued Development

### Removing Gaps Between Toolpath Lines

Toolpaths based on TPMS contour lines have gaps between adjacent toolpaths. This is because TPMS structures defined by isovalues do not have uniform thickness. The gaps can be categorised into two different types. Firstly, calculating adjacent contour lines based on the minimum thickness produces gaps in regions where the distance is larger than the minimum thickness value, as shown in Figure 6.15. The diagram shows the Primitive mathematical functions using the visual graphing tool Desmos with three varying isovalues compared with a printed Primitive part showing the matching gaps where there is a greater distance between adjacent lines.

Secondly, TPMS are composed of primitive patches, where the primitive patch is the most elementary patch that can create an entire lattice surface by affine transformations [185] as discussed in Section 2.4.2. When the vertex of the primitive patch has a tangent plane perpendicular to the print direction, this has a high susceptibility of forming a gap as shown in Figure 6.16. The contour lines

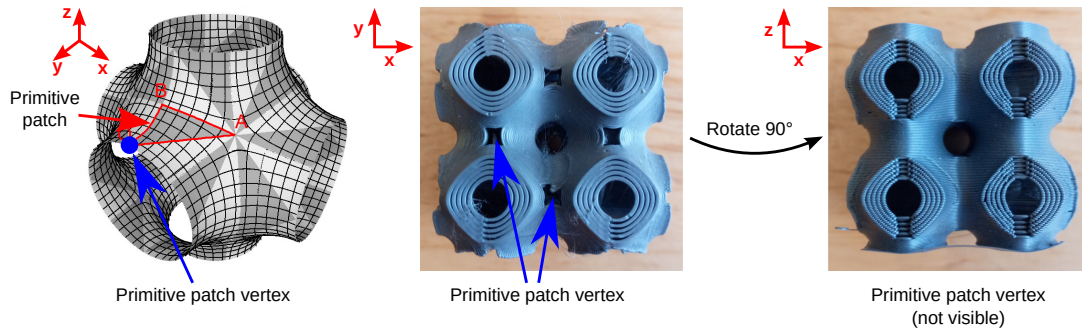


Figure 6.16: Gap between filament occurs at the primitive patch vertex when perpendicular to print direction, i.e.  $z$ -direction. Left-hand diagram shows the TPMS Primitive composed of primitive patches denoted by grey triangles. The vertex that is susceptible to gaps is in blue. The next two diagrams are pictures of a printed Primitive specimen rotated by  $90^\circ$ , as the Primitive is symmetric, showing that the gap only happens when the vertex is perpendicular to the print direction. [Left-hand diagram modified from [commons.wikimedia.org/wiki/File:Lines\\_of\\_curvature\\_make\\_a\\_quadrangulation\\_of\\_the\\_domain.jpg](https://commons.wikimedia.org/wiki/File:Lines_of_curvature_make_a_quadrangulation_of_the_domain.jpg), Licensed under CC-BY-SA, copyright Whitegreen Hua.]

on a slice near the vertices change rapidly as  $z$  changes. The  $z$  height is only increased incrementally by the nozzle size and is therefore difficult to adjust for. When the exact coordinate is not part of the toolpath line there is a high chance for a gap to form as shown by Figure 6.17. This type of gap is also visible in the PrusaSlicer Gyroid infill, which uses the Gyroid explicit function.

### Implementing Further TPMS Types

This algorithm calculates isovalues using the geometric relationships from the previous chapter. As the previous chapter created relationships for five TPMS, other TPMS would not be able to use this algorithm in full. To create other TPMS single and double surface structures, new relationships would have to be established using the methods outlined in the previous chapter. However, the ‘isoline’ structure type would be able to create other TPMS structures if the implicit function and gradient function are implemented into the CAM program.

## 6.5 Conclusion

Geometrically customised TPMS structures can be printed based on an input geometric specification using the developed direct slicing toolpath algorithm. Customised TPMS structures are challenging to create using conventional process flows. This algorithm harnesses the efficiency of infill while offering the customisability of CAD. The geometric properties of TPMS structures can be used to relate to other advanced engineering properties, such as mechanical strength. Once the geometric properties of printed TPMS structures have been related to

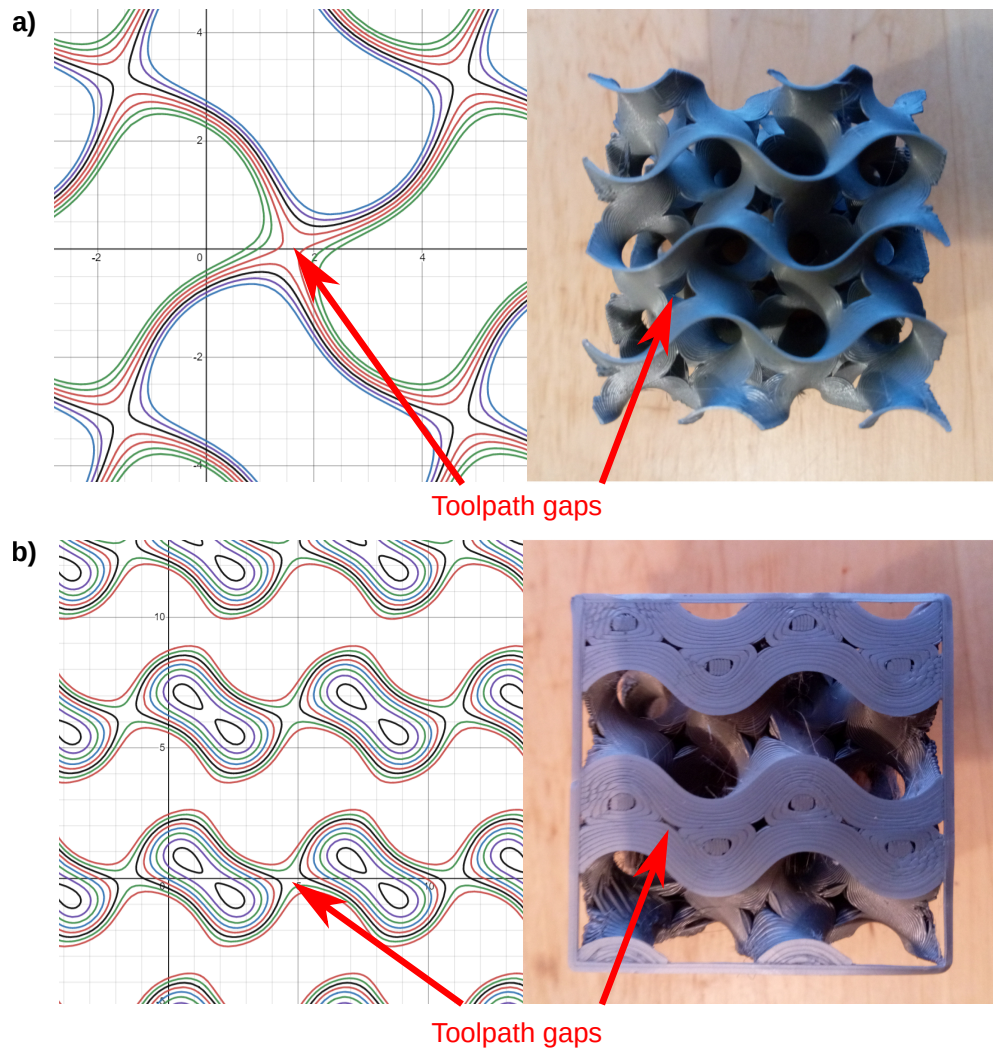


Figure 6.17: Comparison of the mathematical function for a Gyroid double surface structure (a) and single surface structure (b) with varying isovalues. The gaps at the primitive patch vertex match between the mathematical function and the printed specimen.

other properties, these properties can be used directly to create tunable TPMS structures. As such, the final phase of this thesis is to experimentally test customised TPMS in an application, namely compressive mechanical testing. This demonstrates building the relationships between volume fraction with compressive properties of TPMS structures. The experimental testing evaluates the performance of the printed TPMS parts using the direct slicing toolpath algorithm. Also, the testing quantifies the accuracy of the print compared to the calculated geometric properties.

# Chapter 7

## Experimental Application in Additive Manufacturing

### 7.1 Introduction

Many properties of interest to engineers and designers, such as compressive mechanical properties and heat transfer properties, are based on equations that relate to elementary geometric properties. Thus, to design parts with tunable engineering properties, relationships can be established through experimentally testing geometrically customised TPMS structures. These relationships can take advantage of the geometric relationships established in Chapter 5, and then use the toolpath algorithm developed in Chapter 6 to realise the desired geometries.

This chapter focusses on calculating the relationship for creating physical Gyroid structures with tunable compressive strength. The Gyroid was chosen as it is one of the most popular TPMS in the AM community and integrated in commercial toolpath planner software as Gyroid infill. Compressive testing was chosen as there is a generalised relationship between the bulk compressive mechanical properties and the volume fraction of the cellular materials. The relationship is a power law called the Gibson-Ashby relationship

$$E = C(V_f)^n, \quad (7.1)$$

where  $E$  is the Young's modulus,  $V_f$  is the volume fraction between the lattice and a solid object, and  $C$  and  $n$  are constants [240]. The Gibson-Ashby relationship also holds for other properties such as yield strength. The existence and maturity of this empirical model, and the fact that compressive testing can be executed in a controlled manner, makes this a useful mechanism through which to prove the underlying methodology proposed in this research.

### 7.2 Test Specimen Information

Experimental testing was performed on printed Gyroid specimens with a double surface structure. Test specimens were printed using a Prusa Mk3 i3 3D printer

Table 7.1: Test specimen information summary.

| Parameter                   | Data                        |
|-----------------------------|-----------------------------|
| 3D Printer Type             | FDM                         |
| Material                    | PLA                         |
| Nozzle Diameter             | 0.4 mm                      |
| TPMS Type                   | Gyroid                      |
| Outer Geometry              | Cubic                       |
| Dimensions                  | $38 \times 38 \times 38$ mm |
| Number of Cells             | $4 \times 4 \times 4$       |
| Thickness Levels            | 8                           |
| Samples Per Thickness Level | 5                           |

with silver PLA “Prusament” filament and a 0.4 mm nozzle. Specimens were printed with varying volume fractions with the number of lattice unit cells and outer shape held constant. Thus, varying the volume fraction changed the thickness of the specimens, i.e. the number of adjacent toolpath lines. Specimens with different volume fractions will hereafter be referred to as “thickness levels”.

The outer lattice shape is a cube designed with 38 mm side lengths as the circular compression instrument plates have a diameter of 56.57 mm. The lattices were comprised of  $4 \times 4 \times 4$  lattice unit cells. Maskery *et al.* determined Gyroid structures with at least  $4 \times 4 \times 4$  lattice unit cells behave as a bulk lattice structure [10].

For the given geometry and print settings, the maximum possible thickness is eight adjacent filament toolpath lines. Therefore, there were eight thickness levels tested with each thickness level corresponding to the number of integer filament toolpath lines, as shown in Figure 7.1. The thickness level and corresponding isovalues are tabulated in Table 7.2.

The experimental testing followed ISO-604:2003 Plastics - Determination of compressive properties [241]. Each thickness level had five printed specimens leading to a total of forty printed test specimens. Table 7.1 provides the overall information for this set of experiments.

### 7.3 PLA Density Measurement

The density measurement of PLA will be necessary later in this chapter to calculate the volume fraction of the test specimens. The density of Prusament PLA was measured by cutting a piece of filament and measuring the mass  $m_{PLA}$ , the length  $L$ , and the diameter  $d$ . This can be written out as

$$\rho_{PLA} = \frac{m_{PLA}}{\pi(d/2)^2 L}. \quad (7.2)$$

The volume was measured by measuring the length with a metal straight edge and the diameter with calipers. The diameter and mass measurements were mea-



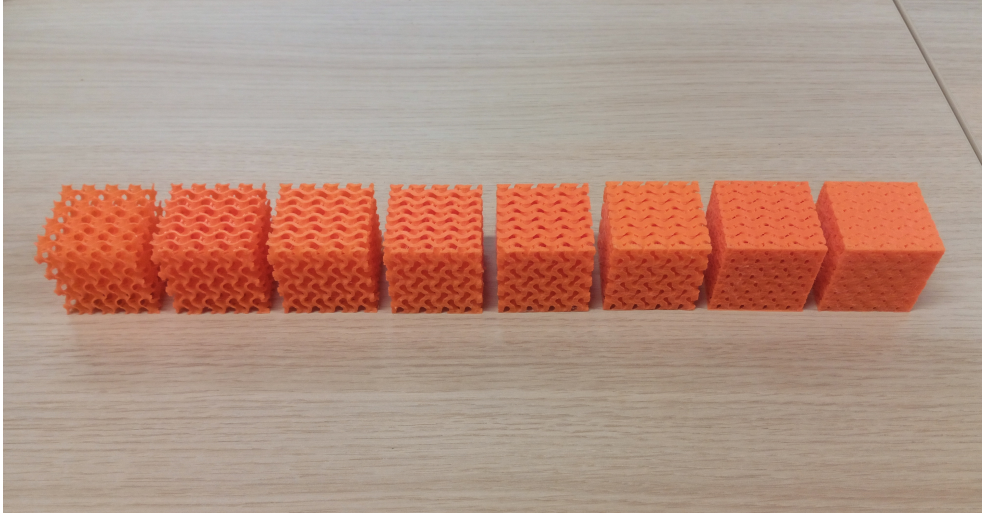


Figure 7.1: Picture of the eight thickness levels of printed Gyroid structures arranged in order of increasing volume fraction.

Table 7.2: Corresponding isovalues to test specimen thickness level. Both perimeter and filler isovalues were calculated with the relationships produced in Chapter 5

| Level | Perimeter Isovalues | Filler Isovalues                    |
|-------|---------------------|-------------------------------------|
| 1     | 0                   |                                     |
| 2     | -0.2, 0.2           |                                     |
| 3     | -0.4, 0.4           | 0                                   |
| 4     | -0.59, 0.59         | -0.2, 0.2                           |
| 5     | -0.77, 0.77         | -0.4, 0, 0.4                        |
| 6     | -0.93, 0.93         | -0.59, -0.2, 0.2, 0.59              |
| 7     | -1.08, 1.08         | -0.77, -0.4, 0, 0.4, 0.77           |
| 8     | -1.21, 1.21         | -0.93, -0.59, -0.2, 0.2, 0.59, 0.93 |

sured with calipers and a weighing scale, respectively, and the measurement was repeated five times. The uncertainties were the standard deviations of the measurements. However, as the section of filament was curved and pliable, the length could not be measured with calipers. Thus the length uncertainty from using the metal straight edge was estimated to be 0.5 mm. The calculated density was  $1.302 \pm 0.032 \text{ g}\cdot\text{cm}^{-3}$ .

## 7.4 Volume Fraction Measurements

The geometric accuracy of the print can be captured by comparing volume fraction measurements to the calculated values from Chapter 5. As such, the volume fractions of the test specimens need to be measured before the compression test-

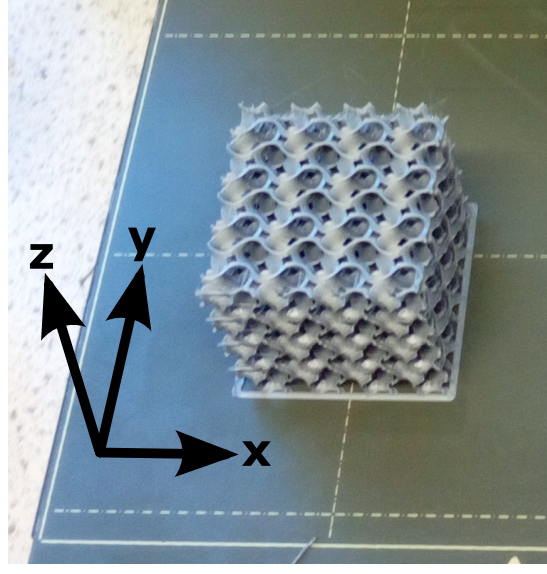


Figure 7.2: Photograph of specimen on printer bed with labelled  $x, y, z$  directions. Print direction is parallel to  $z$  axis.

ing. The volume fraction can be re-written as follows

$$V_f = \frac{\rho_{latt}}{\rho_{PLA}} \quad (7.3)$$

where  $\rho$  is the density. Thus, the three physical quantities to be measured experimentally in the volume fraction can be written as

$$V_f = \frac{m_{latt}}{V_{latt}\rho_{PLA}} \quad (7.4)$$

where  $m_{latt}$  is the mass and  $V_{latt}$  is the overall volume of the specimens.

The mass of each specimen were measured using a Balance Technology AB304-S weighing scale. The volume of the specimens was calculated from measuring each side length. Each specimen side length was measured in the  $x$ -,  $y$ -, and  $z$ -direction using Mitutoyo calipers. The  $x$ -,  $y$ -, and  $z$ -direction are relative to the print direction and print bed as shown in Figure 7.2. The length measurements were measured in different locations on the lattice face. This is to capture that the faces may not be uniform. Table 7.3 summarises the mean and uncertainties of each measured physical property for each thickness level. The measurements were repeated five times to calculate the uncertainty.

The calculated volume fraction using the relationships from Chapter 5 and the experimental volume fraction measurements can now be compared. The discrepancy can be compared to the isovalue that were originally used to calculate the relationships in Chapter 5. Figure 7.3 shows that the discrepancy increases as the thickness increases, i.e. as the volume fraction increases. This shows that as the specimen got thicker and had more toolpath lines, the less accurate the printed specimen became. This is due to the toolpath gaps discussed in Section 6.4.2 and the FDM resolution.



Table 7.3: Mass and length measurements with uncertainties calculated from the standard deviation of five repeats.

| Thickness level | $m_{latt} \pm u(m_{latt})$ g | $x \pm u(x)$ mm    | $y \pm u(y)$ mm    | $z \pm u(z)$ mm    |
|-----------------|------------------------------|--------------------|--------------------|--------------------|
| 1               | $7.9640 \pm 0.0073$          | $38.05 \pm 0.24$   | $38.16 \pm 0.15$   | $37.86 \pm 0.16$   |
| 2               | $15.8673 \pm 0.0052$         | $38.28 \pm 0.32$   | $38.34 \pm 0.20$   | $37.828 \pm 0.067$ |
| 3               | $23.569 \pm 0.010$           | $38.50 \pm 0.10$   | $38.455 \pm 0.060$ | $37.87 \pm 0.10$   |
| 4               | $30.675 \pm 0.013$           | $38.594 \pm 0.052$ | $38.490 \pm 0.061$ | $37.839 \pm 0.044$ |
| 5               | $36.964 \pm 0.015$           | $38.51 \pm 0.12$   | $38.438 \pm 0.068$ | $38.051 \pm 0.045$ |
| 6               | $41.188 \pm 0.035$           | $38.536 \pm 0.086$ | $38.48 \pm 0.21$   | $38.028 \pm 0.065$ |
| 7               | $46.445 \pm 0.087$           | $38.548 \pm 0.063$ | $38.445 \pm 0.091$ | $38.095 \pm 0.078$ |
| 8               | $50.570 \pm 0.064$           | $38.522 \pm 0.083$ | $38.37 \pm 0.14$   | $38.098 \pm 0.082$ |

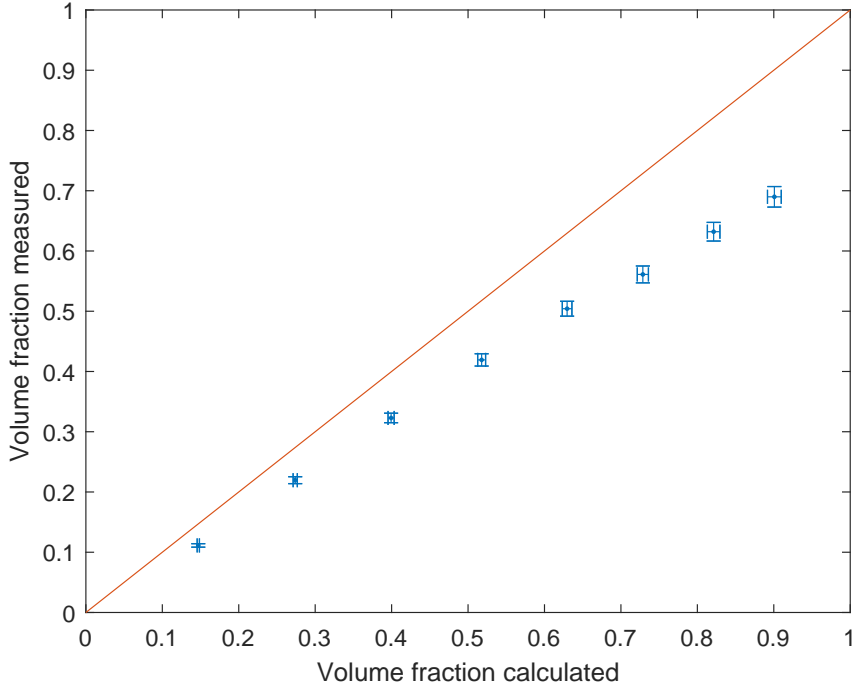


Figure 7.3: The discrepancy between the measured volume fraction and the calculated volume fraction from Chapter 5. As the thickness increase the accuracy decreases due to the toolpath gaps discussed in Chapter 6 and the FDM resolution. The red line is the ideal case of zero discrepancy.

To calculate the combined measurement uncertainty, the general formula [263, 264] for combining uncorrelated measurement is used, specifically

$$\Delta F = \sqrt{\sum_i \left( \frac{\partial F}{\partial x_i} \Delta x_i \right)^2} \quad (7.5)$$

where  $\Delta F$  represents the combined uncertainty of the estimate  $F$  and  $x_i$  are the input estimates.

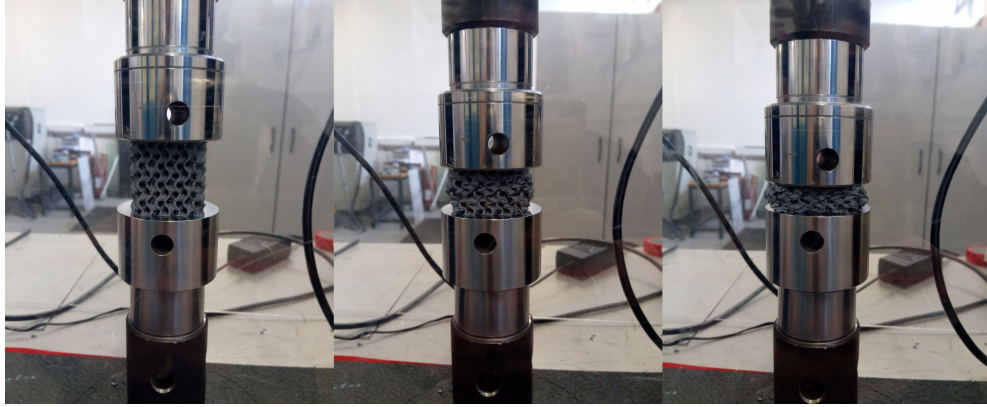


Figure 7.4: Example of the progression of compressive testing.

## 7.5 Compression Testing

The compression testing was conducted on the Instron 3369 using the ISO-604:2003 Plastics — Determination of compressive properties [241]. Each specimen was compressed at a speed of 0.76 mm/min. Each test was run until it was either past the densification point or at the 50 kN limit of the Instron load cell. Figure 7.4 shows an example of the progression of compressive testing. The exported data files contained the distance travelled (mm), force measured (kN), and time (s).

From the raw data, the stress and strain values were calculated and plotted. All raw stress-strain plots of the experimental data are in Appendix B, where there are eight plots for each level and the five curves per sample on each. The stress-strain curves follow three general phases for lattice deformation [265]. At low strains, the lattice elastically deforms, followed by a plastic region, then finally densification.

There were two types of stress-strain plastic behaviour depending on the thickness of the specimen, as shown in Figure 7.5. For thinner specimens, thickness levels one through four, the plastic region had a distinct yield strength, i.e. maximum of the first peak past the elastic region as shown by Figure 7.5(a). These specimens during the compression testing would exhibit a small audible cracking sound at this point. This was especially true for the thickness level one specimens as the plastic region had multiple consistent small peaks for all five repeat specimens. The cracking sounds occurred as there were multiple points of buckling and fracturing as seen in Figure B.1. This is likely because these specimens had no adjacent toolpath lines for support. The consistent buckling behaviour in the plastic region shows that the developed CAM program was able to make consistent structures. As the thickness increased, the plastic region gradually resembled the plastic region of thicker specimens seen in Figure 7.5(b). The thicker specimens did not have a distinct peak where the yield strength occurred. Instead, the peak was more of a “shoulder” where the following plastic region exhibits a shallower gradient on the curve immediately after the elastic region, as plas-

tic deformation sets in. As the specimens become thicker they become stronger as they become more like a solid object. This is a design trade-off between the lightweighting lattice benefit and a solid object.

Using the stress-strain curves, the Young's modulus was calculated from the linear elastic region. All points within this region were then used to create a linear regression model in which the slope is the Young's modulus. The residuals were checked to ensure that the window did not capture nonlinear regions and the largest residual was 0.0032% of the Young's modulus.

## 7.6 Calculate Gibson-Ashby Relationship

The Gibson-Ashby relationship, Equation 7.1, shows that the compressive mechanical properties are directly proportional to the volume fraction of the cellular solid. To solve for Young's modulus, 7.4 was inserted into 7.1

$$E = C \left( \frac{m_{latt}}{V_{latt}\rho_{PLA}} \right)^n, \quad (7.6)$$

where all terms except the constants are experimentally measured. Using non-linear least squares fitting, the Gibson-Ashby relationship for the Young's modulus of the specimens is calculated. The uncertainties of the Gibson-Ashby relationship constants are obtained first by calculating the covariance matrix using the output Jacobian matrix from the MATLAB built-in function `lsqnonlin` with

$$\Sigma = (J^T J)^{-1} \quad (7.7)$$

where  $\Sigma$  is the covariance matrix and  $J$  is the Jacobian matrix. The uncertainties are the square root of the variance terms, i.e. the main diagonal terms, of the covariance matrix. These were used to give the uncertainties of the calculated Young's modulus. The Gibson-Ashby relationship constants were calculated to be  $C = 1274.0 \pm 2.5$  MPa and  $n = 1.4343 \pm 0.0034$ .

The calculated volume fraction using the relationships from Chapter 5 can be substituted into equation 7.6 to obtain the calculated Young's modulus,  $E_{calc}$ . The volume fraction and Young's modulus values were fitted using non-linear least squares regression to obtain the Gibson-Ashby relationship power law constants. The absolute normalised residuals ranged from approximately 1% to 19% as shown in Figure 7.6. All discrepancies are under 10% for volume fractions greater than 20%.

The discrepancy between the measured and calculated Young's modulus was obtained and plotted in Figure 7.7. This assessed how well the physical properties can be predicted from geometric relationships. This shows that the discrepancy increases as the thickness increases. This reflects the volume fraction discrepancy that also increased with increasing thickness.

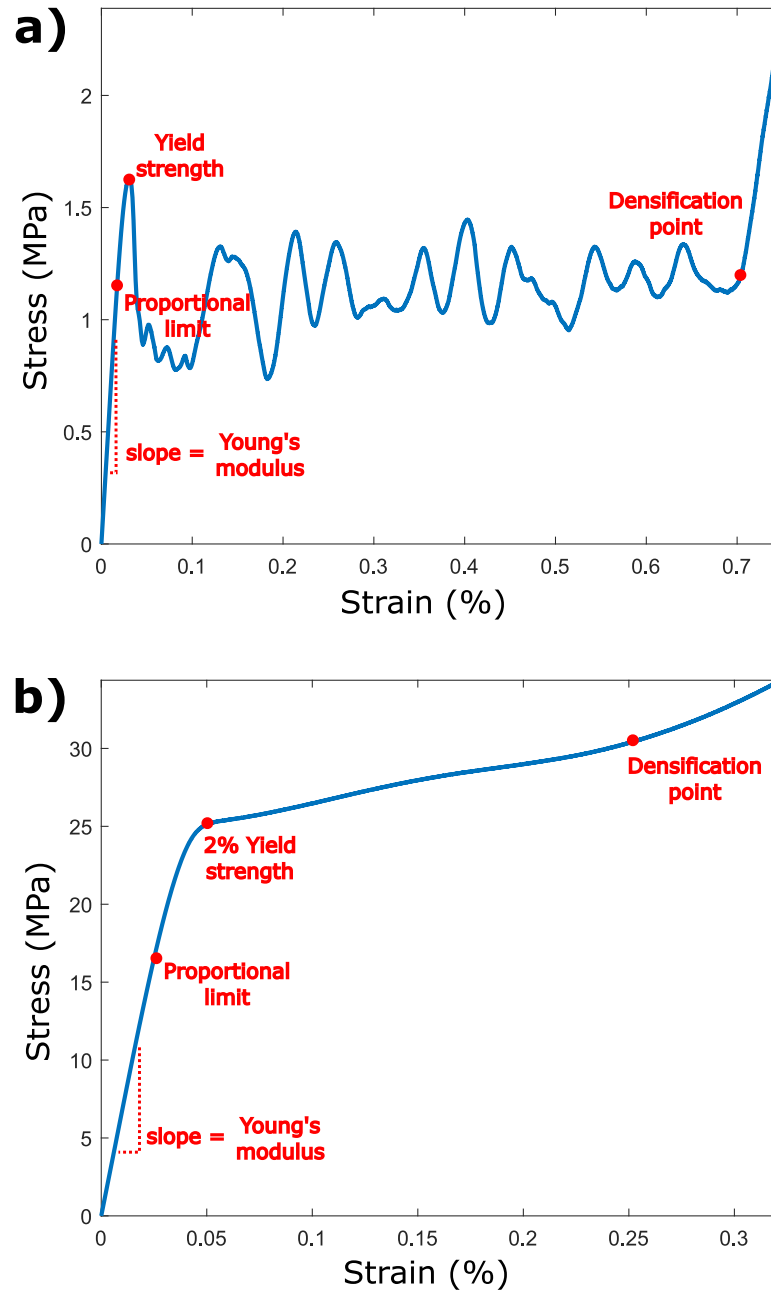


Figure 7.5: Representative results from compression testing for samples of varying thickness. (a) thickness level one. (b) thickness level seven.

## 7.7 Discussion

This chapter relates printed geometrically customised Gyroid double surface structures to compressive mechanical properties. The relationship is calculated between the volume fraction and the Young's modulus based on the Gibson-Ashby relationships. As the measured volume fraction and Young's modulus data are fit to the Gibson-Ashby with low residuals, this successfully shows that the compressive mechanical properties relate to volume fraction as a cellular material. This

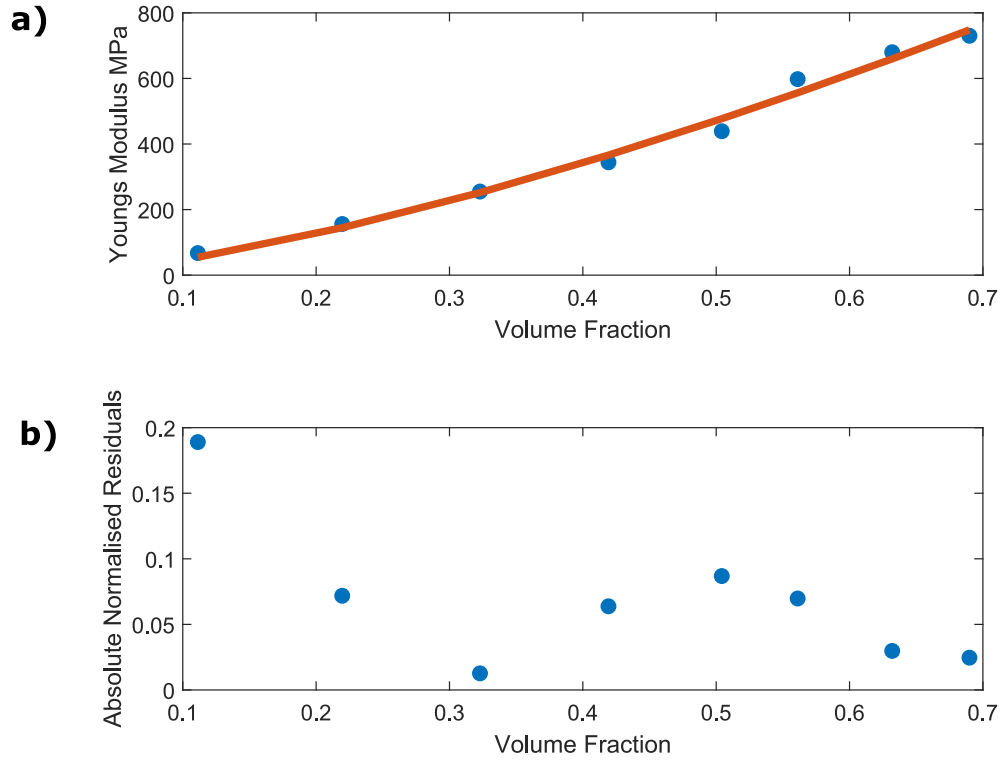


Figure 7.6: Plots depicting the nonlinear fitting of the measured volume fraction and Young's modulus data values. The Gibson-Ashby relationship power law constants were obtained from the fitting. (a) shows the raw data as points and the fitting model as a line plot. (b) shows the absolute normalised residuals showing the magnitude of the relative discrepancy from the fitted power law.

shows that by measuring the volume fraction of Gyroid double structures printed using the CAM program developed in Chapter 6, the Young's modulus can be calculated using the model without having to perform additional compressive testing. From this chapter, the research contribution is this expands on the work of the previous chapter by extending the TPMS structure customisation capabilities to further engineering properties. This further addresses the second research gap identified in Section 2.4.3 by providing a method to customise TPMS using direct slicing methods. Additionally, the accuracy of the toolpath algorithm is quantified and the causes of the toolpath gaps have been identified.

In comparison, there are other research teams who have studied compressive testing on TPMS structures fabricated with FDM using PLA [138, 206–208, 210, 212]. While direct comparisons cannot be made since all but Higuera *et al.* tested different types of TPMS structure. Higuera *et al.* tested double surface Gyroid specimens with varying isovalues and number of lattice unit cells along with different types of FDM filament materials including PLA. The Young's modulus data was not provided and so a direct comparison between this work and the work of Higuera *et al.* was not possible.

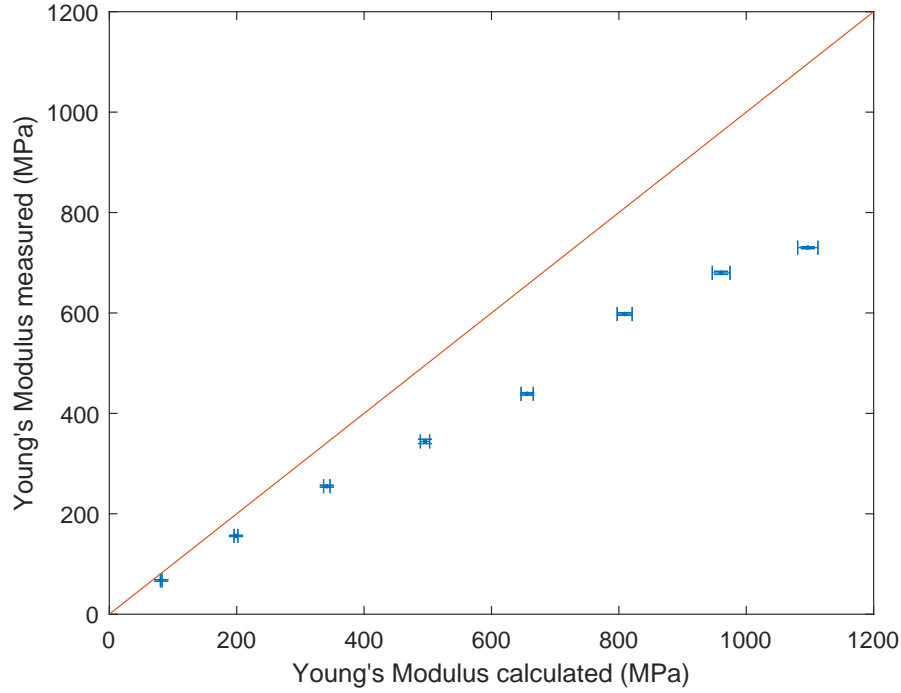


Figure 7.7: The discrepancy between the measured and calculated Young's modulus tended to increase as the thickness increases. This result follows a similar increasing trend to the volume fraction discrepancy. The red line is the ideal case of zero discrepancy.

The volume fraction measurements of the printed specimens are also used to quantify the discrepancy between the measured values and the calculated values using the relationships from Chapter 5. The measured volume fractions are lower than the calculated volume fractions with at least 15% discrepancy as shown in Figure 7.3. The discrepancy increases to almost 30% as the lattice volume fraction is increased. The measurement discrepancies,  $u(v_f)$ , are below 1% and are much smaller in comparison. This indicates that volume fraction discrepancies are due to the toolpath imperfections discussed in Chapter 6 and the FDM filament resolution.

This quantifies the volume fraction discrepancy for a double surface Gyroid. This discrepancy would change for different types of TPMS and structure types. Printed TPMS structures with higher surface area require more filament. If the surface area changes rapidly as the isovalue changes this may indicate more regions where the contour experiences non-isotropic expansion, i.e. more gaps between toolpath lines. As the surface areas for different TPMS types were calculated in Chapter 5, Figures 5.19 and 5.20, this would indicate structures, such as the Diamond, that may have larger volume fraction discrepancies. The different primitive patches of TPMS types will also impact the number of gaps. This is also discussed in Chapter 6, as vertices of primitive patches where the tangent plane is perpendicular to the print direction are susceptible to producing gaps between

toolpath lines. The toolpath algorithm can be optimised to identify regions prone to gaps to reduce the volume fraction discrepancy.

## 7.8 Conclusion

The experiments in this chapter measured the compressive strength for Gyroid structures created using a novel toolpath algorithm, calculated the Gibson-Ashby relationship relating the volume fraction and Young's modulus, and quantified the discrepancies between the measure volume fraction and calculated volume fraction from Chapter 5. From calculating the Gibson-Ashby relationship, this showed the Gyroid structures had compressive mechanical properties of cellular material. The discrepancies between the measure and calculated volume fraction were high, however, this is due to the previously identified issues in Chapter 6. These could be modelled to be accounted for or corrected in the toolpath algorithm as discussed in Chapter 8.

# Chapter 8

## Discussions and Conclusions

### 8.1 Introduction

This thesis details the creation of an alternative process flow for designing and fabricating AM TPMS lattices using meshless methods. Driven by the bottlenecks in the conventional AM process flow, the developed meshless methods allow designers to create customised AM TPMS for a variety of engineering applications. The overarching discussion, conclusion, and future works are detailed in the subsequent sections.

### 8.2 Overarching Discussion

AM is a unique manufacturing method that fabricates parts by adding material in a layer-by-layer fashion. This manufacturing method allows parts to be fabricated with highly customised geometries. In particular, customised lattice structures are feasible with AM. AM lattice structures are attractive across various industries, such as medicine, aerospace, and electrical components, due to their unique high SAVR, porous networks, and lightweight properties.

The challenge with AM lattices is they are difficult to model with the conventional AM process flow. There are two methods for modelling lattices within the conventional AM process flow. AM lattices can be efficiently designed in CAM software as infill. However, there are generally very limited options for lattice type and geometric customisation as discussed in Section 2.3.4. The other method is to design lattices in CAD software for more modelling capability. However, as lattices can have high SAVR, complex topologies, and regions of high curvature, they are difficult to approximate with mesh-based modelling in traditional CAD software and the intermediary file formats as discussed in Section 2.3.4.

This thesis has concentrated on the creation of an alternative AM process flow for lattices, focussing on TPMS, by developing meshless methods, i.e. by using implicit functions. The alternative process flow creates customised TPMS structures as infill in a newly-developed prototype CAM program. This harnesses the efficiency of creating infill whilst having the customisability of CAD modelling.



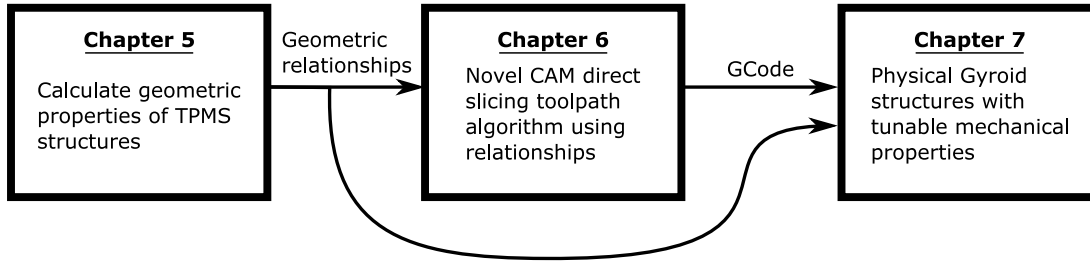


Figure 8.1: The work flow of this research. This shows how the work from each chapter was needed for the next development steps.

The research presented in Chapter 5, Chapter 6, and Chapter 7 follows the progression of an AM process flow. The work from each chapter was needed for the next development steps as shown in Figure 8.1.

This research provides designers with an alternative AM process flow for creating TPMS structures with tunable mechanical properties. As compressive mechanical properties, i.e. Young’s modulus, relates to the volume fraction of cellular structures, the compressive testing in this thesis established the Gibson-Ashby relationship. While there are volume fraction discrepancies, the causes of these issues were identified in Section 6.4.2. From this, the volume fraction for a specified Young’s modulus can be determined. Then, using the determined volume fraction, the direct slicing toolpath algorithm can calculate the exact TPMS implicit function isovalues using the established geometric relationships. Then, with the calculated isovalues and outer shape specifications, the direct slicing toolpath algorithm can output a GCode file to fabricate the customised TPMS structure.

The developed methods addressed the two gaps identified in the literature in Section 2.4.3. The difficulties in creating AM TPMS structures with customised geometric properties was addressed by establishing geometric relationships in Chapter 5. The limited alternative methods to produce customised TPMS structures that avoid mesh-based modelling was addressed in Chapter 6 with the development of the toolpath algorithm. Similar research for creating direct slicing methods for TPMS included the work of Feng *et al.*, Ding *et al.*, and Wang *et al.*. Their work also developed toolpath algorithms to fabricate AM TPMS structures. However, this thesis not only developed a different toolpath algorithm based on contour lines but also the TPMS structures are customisable by a geometric specification input by using geometric relationships from Chapter 5. Also, by using contour lines this produces fewer toolpath lines such that the print runs quickly and smoothly, whilst preserving the TPMS geometry integrity by creating TPMS structures with nested TPMS. Additionally, similar developments for modelling TPMS with implicit functions include the lattice CAD software, such as FLatt Pack, Gen3D, and nTopology [171, 173, 174], and the volumetric extension for 3MF [158]. While they model TPMS using implicit functions, this research models customised TPMS structures as infill in the CAM stage.

There are some known limitations to this research that are worth acknowledging. None of these detract from the originality and, instead, form sensible avenues

for future research. The first limitation is the fact that the developed algorithms and methods have only been developed or applied to a five TPMS geometries. Despite this, the techniques and methods can be extended to new TPMS geometries. The second limitation is that the methods have only been developed and proven for the FDM AM process. However, there are no obviously insurmountable technical barriers that would prevent this research from being modified to suit a different process, such as PBF. These are only current limitations and provide avenues for the methods to be expanded on.

## 8.3 Conclusions

This thesis has fulfilled its aim to develop an alternative AM process flow for creating customised TPMS structures. The work focussed on developing methods to address the identified gaps in literature. As such, the methods resolve difficulties in geometrically customising TPMS structures and provide alternative approaches that avoid the mesh-based bottlenecks in the conventional AM process flow. The research outputs are as follows:

### **Numerical methods to calculate geometric properties for TPMS structures**

A set of numerical methods were established to reliably calculate volume fraction, surface area, and minimum thickness for TPMS structures created with varying isovalues. Multiple numerical techniques were trialled before a set was established based on criteria of reproducibility, accuracy, and computational efficiency. This addresses the discrepancy in creating TPMS structures to a geometric design criteria discussed in Chapter 2. This set of numerical methods and openly available MATLAB program provides designers with a dependable method for generating custom TPMS structures.

### **Relationships between the implicit function isovalue and geometric properties for five TPMS structures**

Empirical relationships between the isovalue and geometric properties were established for Primitive, Gyroid, Diamond, Neovius, and iWP structures. Datasets created using the numerical methods were fit using robust Chebyshev polynomials to a clear accuracy tolerance. The coefficients in a standard polynomial format are available for five TPMS structures for the single and double surface cases. These polynomial relationships are useful as they allow designers to controllably model TPMS structures to design specification by adjusting the TPMS isovalue. While other research teams have calculated geometric properties, this research contributes robust relationships with known tolerances that can be used as is or integrated into the back-end of CAD packages.

**Method to AM TPMS with tunable geometric/mechanical properties without mesh-based CAD or intermediary file formats**

A direct slicing toolpath algorithm was developed that creates GCode for customised TPMS structures based on input geometric property specification. The algorithm adaptively calculates toolpaths based on the contour lines using on the geometric relationships. While other direct slicing methods have been developed by other research groups to create machine code for TPMS, this research can create GCode for geometrically customised TPMS structures. This not only provides developers a deterministic method for manufacturing customised TPMS but also provides a method to relate and tune TPMS structures for an engineering application. Compressive testing was performed on printed Gyroid specimens showed Young's modulus relating to the volume fraction using the Gibson-Ashby relationship. The experiments showed strong preliminary results, with future work identified to close discrepancies.

These research outputs allow designers to model and create geometrically customised TPMS structures and can be implemented into commercial software. From this work, ideas to optimise the methods and augment design capabilities are elaborated below. By fully exploiting the design freedoms permitted by AM, the developed alternative process flow for specially tailored AM TPMS structures can be continually expanded, allowing for more customisability across a range of design specifications in engineering applications.

## 8.4 Future Works

Chapter 2 shows that there is a growing interest of meshless, functional-based modelling and AM TPMS structures within the research communities and industry. There is a continuous need for a standard alternative to mesh-based modelling for structures like lattices. As such, there are a growing number of CAD programs that are based on implicit-based kernels that directly cater to modelling TPMS structures for AM. Alongside, 3MF is releasing a new volumetric intermediary file that can transport functionally-based models to CAM software. These developments compounded with many research groups characterising TPMS structures and their engineering applications in AM indicate a positive future. The contributions from this research support this positive trend.

The following future ideas are a continuation of the work in this thesis. This section starts with ideas for immediate next steps for optimising the developed CAM program. As discussed in Section 6.4.2, the calculated toolpaths for TPMS structures have identified gaps between toolpaths. The toolpath algorithm can be further optimised to mitigate these gaps. Next, this section goes into further developments in the future regarding designing TPMS structures with tunable properties for engineering applications, such as heat exchangers.

### 8.4.1 Optimisation of Toolpath Algorithm

As discussed in Section 6.4.2, there are two identified types of toolpath gaps. The toolpaths are calculated from adjacent contour lines based on the minimum thickness relationships from Chapter 5. As there is a distance distribution between adjacent contour lines, this is where the first type of gap occurs. To mitigate this type of gap, the filament extrusion printer setting could be adaptively adjusted based on distance distribution between adjacent contour lines. As such, the numerical techniques for calculating minimum thickness from Chapter 5 could be adjusted.

Currently, the minimum thickness is calculated as the minimum of the distance travelled of inward facing normals between two surface faces. This algorithm could be altered such that it obtains a representative set of the distance distribution across the structure for the lattice unit cell volume. Then volume regions of the unit cell cube could be categorised based on the thickness distribution. The categorised volume regions could be used in the toolpath algorithm when translating contour lines into GCode. The extrusion value would adaptively be set based on the volume regions.

The other gap occurs at TPMS primitive patch vertices that have a tangential plane perpendicular to the print direction. This region has a high susceptibility of forming a gap as the contour lines change rapidly as  $z$  changes. To potentially mitigate this gap, an extra calculation step could be added to flag this region. TPMS are minimal surfaces defined as having zero mean curvature at every point on the surface. The primitive patch vertices also evaluate to zero Gaussian curvature as they are inflection points [266]. As such, when the contour lines are calculated in the toolpath algorithm, the Gaussian curvature could be calculated for the contour points. This would require the additional calculation step when running the CAM program as well as the Gaussian curvature function to be implemented for each TPMS type.

### 8.4.2 Tunable Properties for Wide Range of Engineering Applications

The alternative process flow can be further developed to enhance the customisation of TPMS structures. As it is further optimised and augmented for new customisation capabilities, this increases the breadth of designing for new engineering applications. Once the toolpath algorithm is optimised such that it can create fully closed structures, the toolpath algorithm can be expanded from only creating GCode for FDM. The algorithm could be generalised to adaptively calculate contours based on different toolpath widths, e.g. laser beam width for PBF, and other technology-specific parameters, such as laser power. The translation of the generalised contour toolpaths could also be expanded to translate into machine code based on the AM technology and machine brand.

Additionally, as the algorithm customises TPMS structures for one geometric specification input at a time, it could be adjusted so it could optimise TPMS

structures for compound geometric properties, such as SAVR. The algorithm can select multiple possible structures that fulfil the compound geometric specification, and then choose a final structure based on other factors such as the AM technology, application properties, etc. For example, a novel heat exchanger with a TPMS structure, such as the example from Chapter 5 in Section 5.6, could be customised with tunable heat transfer properties. Building from the optimisation ideas to print closed structures and implementing other machine code syntax to print on other AM technologies, the toolpath algorithm could implement different types of geometric inputs, such as SAVR or hydraulic diameters. Heat exchangers could then be manufactured with varying specifications and tested for heat transfer properties. This concept could also be applied to other engineering applications, such as lightweighting aerospace structural components. These are a few ideas for expanding the alternative process flow, however, as one of the key benefit of AM is the customisability through a wide range of available AM technologies and materials, there are many more possible avenues for future projects.

# References

- [1] U. M. Dilberoglu, B. Gharehpapagh, U. Yaman, and M. Dolen, “The Role of Additive Manufacturing in the Era of Industry 4.0,” in *Procedia Manufacturing*, vol. 11, pp. 545–554, 2017.
- [2] A. D. Maynard, “Navigating the fourth industrial revolution,” *Nature Nanotechnology*, vol. 10, no. 12, pp. 1005–1006, 2015.
- [3] S. H. Huang, P. Liu, A. Mokasdar, and L. Hou, “Additive manufacturing and its societal impact: a literature review,” *The International Journal of Advanced Manufacturing Technology*, vol. 67, pp. 1191–1203, jul 2013.
- [4] N. Saengchairat, T. Tran, and C.-k. Chua, “A review: additive manufacturing for active electronic components,” *Virtual and Physical Prototyping*, 2017.
- [5] K. V. Wong and A. Hernandez, “A Review of Additive Manufacturing,” *ISRN Mechanical Engineering*, 2012.
- [6] T. D. Ngo, A. Kashani, G. Imbalzano, K. T. Nguyen, and D. Hui, “Additive manufacturing (3D printing): A review of materials, methods, applications and challenges,” *Composites Part B: Engineering*, vol. 143, pp. 172–196, jun 2018.
- [7] A. Uriondo, M. Esperon-Miguez, and S. Perinpanayagam, “The present and future of additive manufacturing in the aerospace sector: A review of important aspects,” *Proceedings of the Institution of Mechanical Engineers, Part G: Journal of Aerospace Engineering*, 2015.
- [8] G. Costabile, M. Fera, F. Fruggiero, A. Lambiase, and D. Pham, “Cost models of additive manufacturing : A literature review,” *International Journal of Industrial Engineering Computations*, vol. 8, pp. 263–282, 2017.
- [9] A. du Plessis, S. M. J. Razavi, M. Benedetti, S. Murchio, M. Leary, M. Watson, D. Bhate, and F. Berto, “Properties and applications of additively manufactured metallic cellular materials: A review,” *Progress in Materials Science*, vol. 125, p. 100918, 2022.

- [10] I. Maskery, L. Sturm, A. O. Aremu, A. Panesar, C. B. Williams, C. J. Tuck, R. D. Wildman, I. A. Ashcroft, and R. J. Hague, “Insights into the mechanical properties of several triply periodic minimal surface lattice structures made by polymer additive manufacturing,” *Polymer*, pp. 1–10, 2017.
- [11] T. J. Gordelier, P. R. Thies, L. Turner, and L. Johanning, “Optimising the FDM additive manufacturing process to achieve maximum tensile strength: a state-of-the-art review,” *Rapid Prototyping Journal*, vol. 25, no. 6, pp. 953–971, 2019.
- [12] O. Al-Ketan and R. K. Abu Al-Rub, “Multifunctional Mechanical Metamaterials Based on Triply Periodic Minimal Surface Lattices,” *Advanced Engineering Materials*, vol. 21, no. 10, pp. 1–39, 2019.
- [13] S. R. K. Ledalla, B. Tirupathi, and V. Sriram, “Performance Evaluation of Various STL File Mesh Refining Algorithms Applied for FDM-RP Process,” *Journal of The Institution of Engineers (India): Series C*, vol. 99, no. 3, pp. 339–346, 2018.
- [14] C. Iancu, D. Iancu, and A. Stancioiu, “From CAD model to 3D print via “STL” file format,” *Fiabilitate si Durabilitate*, pp. 73–80, 2010.
- [15] I. Stroud and P. C. Xirouchakis, “STL and extensions,” *Advances in engineering software*, vol. 31, pp. 83–95, 2000.
- [16] J. Ding, Q. Zou, S. Qu, P. Bartolo, X. Song, and C. C. Wang, “STL-free design and manufacturing paradigm for high-precision powder bed fusion,” in *CIRP Annals - Manufacturing Technology*, vol. 70, pp. 167–170, 2021.
- [17] D. Ma, F. Lin, and C. K. Chua, “Rapid Prototyping Applications in Medicine . Part 2 : STL File Generation and Case Studies,” *Advanced Manufacturing Technology*, pp. 118–127, 2001.
- [18] O. Fryazinov and A. Pasko, “Interactive ray shading of FRep objects,” *16th International Conference in Central Europe on Computer Graphics, Visualization and Computer Vision*, pp. 145–152, 2008.
- [19] D. Popov, E. Maltsev, O. Fryazinov, A. Pasko, and I. Akhatov, “Efficient contouring of functionally represented objects for additive manufacturing,” *Computer-Aided Design*, dec 2020.
- [20] O. Al-Ketan, M. Pelanconi, A. Ortona, and R. K. Abu Al-Rub, “Additive manufacturing of architected catalytic ceramic substrates based on triply periodic minimal surfaces,” *Journal of the American Ceramic Society*, vol. 102, no. 10, pp. 6176–6193, 2019.
- [21] I. Gibson, D. Rosen, and B. Stucker, *Additive Manufacturing Technologies*. Springer, 2015.

- 
- [22] W. E. Masters, "United States Patent: 4665492 - Computer automated manufacturing process and system," 1987.
- [23] "3-D Printing Steps into the Spotlight," 2013.
- [24] R. Howard, *Connecting the dots: my life and inventions, from X-rays to death rays*. Welcome Rain, 2009.
- [25] R. Jones, P. Haufe, E. Sells, P. Iravani, V. Olliver, C. Palmer, and A. Bowyer, "Reprap - The replicating rapid prototyper," *Robotica*, vol. 29, pp. 177–191, 2011.
- [26] C. Barnatt, *3D Printing: The Next Industrial Revolution*. ExplainingTheFuture.com, 2013.
- [27] "The Evolution of 3D Printing: Past, Present and Future," 2015. <https://3dprintingindustry.com/news/evolution-3d-printing-past-present-future-90605>.
- [28] "ISO/ASTM 52900:2021 Additive manufacturing — General principles — Fundamentals and vocabulary," 2021.
- [29] A. Zhang, Y. Bernard, "AM Feature and Knowledge Based Process Planning for Additive Manufacturing in Multiple Parts Production Context," in *Proceedings of 25th Annual International Solid Freeform Fabrication Symposium*, vol. 44, pp. 1259–1276, 2014.
- [30] Z. Zhu, V. G. Dhokia, A. Nassehi, and S. T. Newman, "A review of hybrid manufacturing processes - state of the art and future perspectives," *International Journal of Computer Integrated Manufacturing*, vol. 26, no. 7, pp. 596–615, 2013.
- [31] O. Abdulhameed, A. Al-ahmari, W. Ameen, and S. H. Mian, "Additive manufacturing: Challenges, trends, and applications," *Advances in Mechanical Engineering*, vol. 11, no. 2, pp. 1–27, 2019.
- [32] W. Gao, Y. Zhang, D. Ramanujan, K. Ramani, Y. Chen, C. B. Williams, C. C. L. Wang, Y. C. Shin, S. Zhang, and P. D. Zavattieri, "The status , challenges , and future of additive manufacturing in engineering," *Computer-Aided Design*, vol. 69, pp. 65–89, 2015.
- [33] P. Foteinopoulos, A. Papacharalampopoulos, and P. Stavropoulos, "On thermal modeling of Additive Manufacturing processes," *CIRP Journal of Manufacturing Science and Technology*, vol. 20, pp. 66–83, 2018.
- [34] E. Mirkoohi, J. Ning, P. Bocchini, O. Fergani, K.-N. Chiang, and S. Liang, "Thermal Modeling of Temperature Distribution in Metal Additive Manufacturing Considering Effects of Build Layers, Latent Heat, and Temperature-Sensitivity of Material Properties," *Journal of Manufacturing and Materials Processing*, vol. 2, no. 3, p. 63, 2018.
-



- 
- [35] B. Durakovic and B. Durakovic, “Design for Additive Manufacturing : Benefits , Trends and Challenges,” *Periodicals of Engineering and Natural Sciences*, vol. 6, no. 2, pp. 179–191, 2018.
- [36] J. T. Collins, J. Knapper, J. Stirling, J. Mduda, C. Mkindi, V. Mayagaya, G. A. Mwakajinga, P. T. Nyakyi, V. L. Sanga, D. Carbery, *et al.*, “Robotic microscopy for everyone: the openflexure microscope,” *Biomedical Optics Express*, vol. 11, no. 5, pp. 2447–2460, 2020.
- [37] J. Stirling, V. L. Sanga, P. T. Nyakyi, G. A. Mwakajinga, J. T. Collins, K. Bumke, J. Knapper, Q. Meng, S. McDermott, and R. Bowman, “The openflexure project. the technical challenges of co-developing a microscope in the uk and tanzania,” in *2020 IEEE Global Humanitarian Technology Conference (GHTC)*, pp. 1–4, IEEE, 2020.
- [38] World Health Organization, “Guidelines for health care equipment donations,” tech. rep., 2000.
- [39] M. D. Monzón, Z. Ortega, A. Martínez, and F. Ortega, “Standardization in additive manufacturing : activities carried out by international organizations and projects,” *International Journal of Advanced Manufacturing Technology*, pp. 1111–1121, 2015.
- [40] R. Bonnard, J. Y. Hascoët, and P. Mognol, “Data model for additive manufacturing digital thread: state of the art and perspectives,” *International Journal of Computer Integrated Manufacturing*, vol. 32, no. 12, pp. 1170–1191, 2019.
- [41] R. Bonnard, P. Mognol, and J. Y. Hascoët, “A new digital chain for additive manufacturing processes,” *Virtual and Physical Prototyping*, vol. 5, no. 2, pp. 75–88, 2010.
- [42] D. Zhao, T. Liu, M. Zhang, R. Liang, and B. Wang, “Fabrication and characterization of aerosol-jet printed strain sensors for multifunctional composite structures,” *Smart Materials and Structures*, vol. 21, 2012.
- [43] J. Li, T. Unander, A. Cabezas, B. Shao, Z. Liu, Y. Feng, E. Forsberg, Z. Zhang, I. Jogi, X. Gao, M. Borman, L. Zheng, M. Ostling, H. Nilsson, and S. Zhang, “Ink-jet printed thin-film transistors with carbon nanotube channels shaped in long strips,” *Journal of Applied Physics*, vol. 109, 2011.
- [44] P. Beecher, P. Servati, A. Rozhin, V. Scardaci, S. Pisana, T. Hasan, A. J. Flewitt, J. Robertson, and G. W. Hsieh, “Ink-jet printing of carbon nanotube thin film transistors,” *Journal of Applied Physics*, vol. 102, 2007.
- [45] K. Gnanasekaran, T. Heijmans, S. Bennekom, H. Woldhuis, S. Wijnia, G. With, and H. Friedrich, “3D Printing of CNT- and Graphene-Based Conductive Nanocomposites by Fused Deposition Modeling,” *Applied Materials Today*, pp. 21–28, 2017.
-

- 
- [46] S. Dul, L. Fambri, and A. Pegoretti, “Fused deposition modelling with ABS – graphene nanocomposites,” *Composites: Part A*, vol. 85, pp. 181–191, 2016.
- [47] E. B. Secor, P. L. Prabhumirashi, K. Puntambekar, M. L. Geier, and M. C. Hersam, “Inkjet Printing of High Conductivity , Flexible Graphene Patterns,” *Physical Chemistry Letters*, 2013.
- [48] H. Ning, J. H. Pikul, R. Zhang, X. Li, S. Xu, J. Wang, J. A. Rogers, W. P. King, and P. V. Braun, “Holographic patterning of high-performance on-chip 3D lithium-ion microbatteries,” *Proceedings of the National Academy of Sciences of the United States of America*, vol. 112, no. 21, pp. 6573–6578, 2015.
- [49] K. Sun, T.-s. Wei, B. Y. Ahn, J. Y. Seo, S. J. Dillon, and J. A. Lewis, “3D Printing of Interdigitated Li-Ion Microbattery Architectures,” *Advanced Materials*, vol. 25, pp. 4539–4543, 2013.
- [50] J. Li, X. Liang, F. Liou, and J. Park, “Macro-/Micro-Controlled 3D Lithium-Ion Batteries via Additive Manufacturing and Electric Field Processing,” *Scientific Reports*, no. October 2017, pp. 1–11, 2018.
- [51] K. Fu, Y. Wang, C. Yan, Y. Yao, Y. Chen, J. Dai, S. Lacey, Y. Wang, J. Wan, T. Li, Z. Wang, Y. Xu, and L. Hu, “Graphene Oxide-Based Electrode Inks for 3D-Printed Lithium-Ion Batteries,” *Advanced Materials*, vol. 28, pp. 2587–2594, 2016.
- [52] E. García-Tuñón, S. Barg, J. Franco, R. Bell, S. Eslava, D. Elia, R. C. Maher, F. Guitian, and E. Saiz, “Printing in three-dimensions with graphene,” *Advanced Materials*, pp. 1–14, 2015.
- [53] T. Rahman, L. Renaud, D. Heo, and M. Renn, “Aerosol based direct-write micro-additive fabrication method for sub-mm 3D metal-dielectric structures,” *Journal of Micromechanics and Microengineering*, vol. 25, 2015.
- [54] B. H. King, M. J. O. Reilly, and S. M. Barnes, “Characterizing Aerosol Jet Multi-Nozzle Process Parameters For Non-Contact Front Side Metallization of Silicon Solar Cells,” in *Photovoltaic Specialists, IEEE Conference*, 2009.
- [55] J. R. Castrejon-Pita, W. R. S. Baxter, J. Morgan, S. Temple, G. D. Martin, and I. M. Hutchings, “Future , Opportunities and Challenges of Inkjet Technologies,” *Atomization and Sprays*, vol. 23, pp. 541–565, 2013.
- [56] A. Boschetto, V. Giordano, and F. Veniali, “Modelling micro geometrical profiles in fused deposition process,” *International Journal of Advanced Manufacturing Technology*, 2011.
- [57] T. D. Seers and N. Alyafei, “Open Source Toolkit for Micro-Model Generation Using 3D Printing,” in *Society of Petroleum Engineers*, 2018.
-

- 
- [58] J. A. McGeough, M. C. Leu, K. P. Rajurkar, A. K. M. De Silva, and Q. Liu, "Electroforming Process and Application to Micro/Macro Manufacturing," *CIRP Annals*, vol. 50, no. 2, pp. 499–514, 2001.
- [59] A. Lopes, E. MacDonald, and R. Wicker, "Integrating Stereolithography and Direct Print Technologies for 3D Structural Electronics Fabrication," *Rapid Prototyping Journal*, 2014.
- [60] F. Niesler and M. Hermatschweiler, "Additive Manufacturing of Micro-sized Parts," *Laser Technik Journal*, pp. 16–18, 2014.
- [61] S. L. N. Ford, "Additive Manufacturing Technology: Potential Implications for U.S. Manufacturing," *Journal of International Commerce and Economics*, 2014.
- [62] M. Delic and D. R. Evers, "Additive manufacturing : empirical evidence for supply chain integration and performance from the automotive industry," *Supply Chain Management*, no. December 2017, 2019.
- [63] P. A. Kobryn, N. R. Ontko, L. P. Perkins, and J. S. Tiley, "Additive Manufacturing of Aerospace Alloys for Aircraft Structures," in *Defense Technical Information Center*, 2006.
- [64] R. Leal, F. M. Barreiros, L. Alves, F. Romeiro, J. C. Vasco, M. Santos, and C. Marto, "Additive manufacturing tooling for the automotive industry," *Journal of Advanced Manufacturing Technology*, pp. 1671–1676, 2017.
- [65] M. Richardson and B. Haylock, "Designer/Maker: The Rise of Additive Manufacturing, Domestic-Scale Production and the Possible Implications for the Automotive Industry," *Computer-Aided Design*, no. 2, pp. 33–48, 2012.
- [66] M. Hoppe and T. Trachsel, "Emerging trends in transport technologies : The potential for transformation towards sustainable mobility," in *ICTTE 2018, Belgrade, Serbia, 27-28 September 2018*, 2018.
- [67] A. Fortier, M. G. Pecht, and Y. Xing, "Embedded Sensors for In-Situ Cell Monitoring of Batteries," 2018.
- [68] A. G. Cooper, S. Kang, J. W. Kietzman, F. B. Prinz, J. L. Lombardi, and L. E. Weiss, "Automated Fabrication of Complex Molded Parts Using Mold Shape Deposition Manufacturing," *Materials and Design*, vol. 20, no. 2, pp. 83–89, 1999.
- [69] T. Fabian, F. Holman, S. Kang, H.-C. Liu, M. Matsunaga, F. B. Prinz, and H. Prinz, Menlo Park, CA Tsuru, "Miniature Gas Turbine Enginer With Unitary Rotor Shaft For Power Generator," 2005.
-

- 
- [70] D. Ding, Z. Pan, D. Cuiuri, and H. Li, “Wire-feed additive manufacturing of metal components : technologies , developments and future interests,” *International Journal of Advanced Manufacturing Technology*, 2015.
- [71] G. Baudana, S. Biamino, D. Ugues, M. Lombardi, P. Fino, M. Pavese, and C. Badini, “Titanium aluminides for aerospace and automotive applications processed by Electron Beam Melting : Contribution of Politecnico di Torino,” *Metal Powder Report*, vol. 71, no. 3, pp. 193–199, 2016.
- [72] F. Ning, W. Cong, J. Qiu, J. Wei, and S. Wang, “Additive Manufacturing of Carbon Fiber Reinforced Thermoplastic Composites Using Fused Deposition Modeling,” *Composites Part B*, pp. 369–378, 2015.
- [73] M. A. Caminero, J. M. Chacón, I. García-moreno, and J. M. Reverte, “Interlaminar bonding performance of 3D printed continuous fibre reinforced thermoplastic composites using fused deposition modelling,” *Polymer Testing*, vol. 68, pp. 415–423, 2018.
- [74] A. Katz-Demyanetz, V. V. Popov Jr., A. Kovalevsky, D. Safranchik, and A. Koptug, “Powder-bed additive manufacturing for aerospace application: Techniques , metallic and metal / ceramic composite materials and trends,” *Manufacturing Review*, vol. 5, 2019.
- [75] E. C. Tsirogiannis, G. E. Stavroulakis, and S. S. Makridis, “Electric Car Chassis for Shell Eco Marathon Competition : Design , Modelling and Finite Element Analysis,” *World Electric Vehicle Journal*, pp. 1–13, 2019.
- [76] J. Gussone, Y.-c. Hagedorn, H. Gherekhloo, G. Kasperovich, T. Merzouk, and J. Hausmann, “Microstructure of gamma-titanium aluminide processed by selective laser melting at elevated temperatures,” *Intermetallics*, vol. 66, pp. 133–140, 2015.
- [77] J. J. S. Dilip, H. Miyanaji, A. Lassell, T. L. Starr, and B. Stucker, “A novel method to fabricate TiAl intermetallic alloy 3D parts using additive manufacturing,” *Defence Technology*, vol. 13, pp. 72–76, 2017.
- [78] V. Juechter, M. M. Franke, T. Merenda, A. Stich, C. Körner, and R. F. Singer, “Additive manufacturing of Ti-45Al-4Nb-C by selective electron beam melting for automotive applications,” *Additive Manufacturing*, vol. 22, pp. 118–126, 2018.
- [79] P. R. Gradl, W. Brandsmeier, and S. E. Greene, “Channel Wall Nozzle Manufacturing and Hot-Fire Testing using a Laser Wire Direct Closeout Technique for Liquid Rocket Engines,” in *2018 Joint Propulsion Conference*, (Reston, Virginia), pp. 1–13, American Institute of Aeronautics and Astronautics, jul 2018.
-

- 
- [80] E. Fonda-Marsland, G. Roberts, D. Gibbon, and C. Ryan, "Development of a Low-Cost 0.1N High Test Peroxide Thruster Using Additive Manufacturing," in *AIAA Propulsion and Energy 2019 Forum*, pp. 1–17, 2019.
- [81] L. E. Murr, S. M. Gaytan, A. Ceylan, E. Martinez, J. L. Martinez, D. H. Hernandez, B. I. Machado, D. A. Ramirez, F. Medina, S. Collins, and R. B. Wicker, "Characterization of titanium aluminide alloy components fabricated by additive manufacturing using electron beam melting," *Acta Materialia*, vol. 58, pp. 1887–1894, 2010.
- [82] M. Todai, T. Nakano, T. Liu, H. Y. Yasuda, K. Hagihara, K. Cho, M. Ueda, and M. Takeyama, "Effect of building direction on the microstructure and tensile properties of Ti-48Al-2Cr-2Nb alloy additively manufactured by electron beam melting," *Additive Manufacturing*, vol. 13, pp. 61–70, 2017.
- [83] M. F. E. Kashouty, A. E. W. Rennie, and M. Ghazy, "Assessing additive and subtractive manufacturing technologies for the production of tools in the automotive industry," in *The 23rd CAPE Conference: Manufacturing Research and its Applications in the 21st Century*, 2015.
- [84] M. Yakout, A. Cadamuro, M. A. Elbestawi, and S. C. Veldhuis, "The Selection of Process Parameters in Additive Manufacturing for Aerospace Alloys," *Advanced Manufacturing Technology*, pp. 2081–2098, 2017.
- [85] C. Zhou, H. Wang, T. A. Perry, and J. G. Schroth, "On The Analysis Of Metal Droplets During Cold Metal Transfer," *Procedia Manufacturing*, vol. 10, pp. 694–707, 2017.
- [86] S. Selvi, A. Vishvakshnan, and E. Rajasekar, "Cold metal transfer (CMT) technology - An overview," *Defence Technology*, vol. 14, pp. 28–44, 2018.
- [87] J. Gou, J. Shen, S. Hu, Y. Tian, and Y. Liang, "Microstructure and mechanical properties of as-built and heat-treated Ti-6Al-4V alloy prepared by cold metal transfer additive manufacturing," *Journal of Manufacturing Processes*, vol. 42, pp. 41–50, 2019.
- [88] X. Zhang, R. Tiwari, A. H. Shooshtari, and M. M. Ohadi, "An additively manufactured metallic manifold-microchannel heat exchanger for high temperature applications," *Applied Thermal Engineering*, vol. 143, pp. 899–908, 2018.
- [89] Y. Ding, M. Akbari, and R. Kovacevic, "Process planning for laser wire-feed metal additive manufacturing system," *International Journal of Advanced Manufacturing Technology*, 2018.
- [90] B. M. Peters, J. Kumpfert, C. H. Ward, and C. Leyens, "Titanium Alloys for Aerospace Applications," *Advanced Engineering Materials*, vol. 5, no. 6, pp. 419–427, 2003.
-

- 
- [91] C. Beyer and D. Figueroa, "Design and Analysis of Lattice Structures for Additive Manufacturing," *Journal of Manufacturing Science and Engineering*, vol. 138, pp. 1–15, 2016.
- [92] M. Salmi, "Possibilities of Preoperative Medical Models Made by 3D Printing or Additive Manufacturing," *Journal of Medical Engineering*, 2016.
- [93] J. Tuomi, K.-s. Paloheimo, and M. Salmi, "A Novel Classification and On-line Platform for Planning and Documentation of Medical Applications of Additive Manufacturing," *Surgical Innovation*, 2014.
- [94] SME, "Medical Additive Manufacturing/ 3D Printing," tech. rep., 2018. available at: <https://www.sme.org/medical-am3dp>.
- [95] A. D. Plessis, I. Yadroitsava, I. Yadroitsev, S. G. le Roux, and D. C. Blaine, "Numerical comparison of lattice unit cell designs for medical implants by Numerical comparison of lattice unit cell designs for medical implants by additive manufacturing," *Virtual and Physical Prototyping*, pp. 1–16, 2018.
- [96] M. Salmi, K.-s. Paloheimo, J. Tuomi, J. Wolff, and A. Mäkitie, "Accuracy of medical models made by additive manufacturing (rapid manufacturing)," *Journal of Cranio-Maxillofacial Surgery*, 2013.
- [97] J. M. Pinto, C. Arrieta, M. E. Andia, S. Uribe, J. Ramos-Grez, A. Vargas, P. Irarrazaval, and C. Tejos, "Geometric Error in Rapid Prototyping Models for Oral and Maxillofacial Applications Sensitivity Analysis of Geometric Errors in Additive Manufacturing Medical Models," *Medical Engineering and Physics*, vol. 37, pp. 328–334, 2015.
- [98] Z. Fourie, J. Damstra, R. H. Schepers, P. O. Gerrits, and Y. Ren, "Segmentation process significantly influences the accuracy of 3D surface models derived from cone beam computed tomography," *European Journal of Radiology*, vol. 81, pp. 524–530, 2012.
- [99] A. Mellati, S. Dai, J. Bi, B. Jin, and H. Zhang, "A biodegradable thermosensitive hydrogel with tuneable properties for mimicking three-dimensional microenvironments of stem cells," *RSC Advances*, pp. 63951–63961, 2014.
- [100] Y. Brudno and D. J. Mooney, "On-demand drug delivery from local depots," *Journal of Controlled Release*, vol. 219, pp. 8–17, 2015.
- [101] S. Y. Chin, Y. C. Poh, A.-c. Kohler, J. T. Compton, L. Hsu, K. M. Lau, S. Kim, B. W. Lee, F. Y. Lee, and K. Samuel, "Additive manufacturing of hydrogel-based materials for next-generation implantable medical devices," *Science Robotics*, 2017.
- [102] P. Sofokleous, E. Stride, W. Bonfield, and M. Edirisinghe, "Design construction and performance of a portable handheld electrohydrodynamic
-

- 
- multi-needle spray gun for biomedical application,” *Material Science and Engineering C*, vol. 33, pp. 213–223, 2013.
- [103] L. Koch, A. Deiwick, S. Schlie, S. Michael, M. Gruene, V. Coger, D. Zychlinski, A. Schambach, K. Reimers, P. M. Vogt, and B. Chichkov, “Skin tissue generation by laser cell printing Skin Tissue Generation by Laser Cell Printing,” *Biotechnology and Bioengineering*, 2012.
- [104] A. Atala and G. Forgacs, “Three-Dimensional Bioprinting in Regenerative Medicine: Reality, Hype, and Future,” *Stem Cells Translational Medicine*, pp. 744–745, 2019.
- [105] D. A. Neamen, *Semiconductor Physics and Devices*. McGraw-Hill Higher Education, 3 ed., 2003.
- [106] J. G. Korvink and A. Greiner, *Semiconductors for Micro- and Nanotechnology*. Wiley-VCH, 2002.
- [107] A. Panesar, M. Abdi, D. Hickman, and I. Ashcroft, “Strategies for functionally graded lattice structures derived using topology optimisation for Additive Manufacturing,” *Additive Manufacturing*, vol. 19, pp. 81–94, 2018.
- [108] J. A. Harris, R. E. Winter, and G. J. McShane, “Impact response of additively manufactured metallic hybrid lattice materials,” *International Journal of Impact Engineering*, vol. 104, pp. 177–191, 2017.
- [109] A. Pasko, O. Fryazinov, T. Vilbrandt, P. A. Fayolle, and V. Adzhiev, “Procedural function-based modelling of volumetric microstructures,” *Graphical Models*, vol. 73, no. 5, pp. 165–181, 2011.
- [110] R. Attarzadeh, M. Rovira, and C. Duwig, “Design analysis of the “Schwartz D” based heat exchanger: A numerical study,” *International Journal of Heat and Mass Transfer*, vol. 177, oct 2021.
- [111] S. Chekurov, J. Kajaste, K. Saari, H. Kauranne, M. Pietola, and J. Partanen, “Additively manufactured high-performance counterflow heat exchanger,” *Progress in Additive Manufacturing*, vol. 4, pp. 55–61, 2019.
- [112] M. Pelanconi, M. Barbato, S. Zavattoni, G. Vignoles, and A. Ortona, “Thermal design, optimization and additive manufacturing of ceramic regular structures to maximize the radiative heat transfer,” *Materials and Design*, vol. 163, feb 2019.
- [113] N. A. Dudukovic, E. J. Fong, H. B. Gemed, J. R. DeOtte, M. R. Cerón, B. D. Moran, J. T. Davis, S. E. Baker, and E. B. Duoss, “Cellular fluidics,” *Nature*, vol. 595, no. 7865, pp. 58–65, 2021.
-

- 
- [114] S. Kim, D. H. Kim, W. Kim, Y. T. Cho, and N. X. Fang, “Additive Manufacturing of Functional Microarchitected Reactors for Energy, Environmental, and Biological Applications,” *International Journal of Precision Engineering and Manufacturing - Green Technology*, vol. 8, no. 1, pp. 303–326, 2021.
- [115] N. Burns, M. Burns, D. Travis, L. Geekie, and A. E. Rennie, “Designing Advanced Filtration Media through Metal Additive Manufacturing,” *Chemical Engineering and Technology*, vol. 39, no. 3, pp. 535–542, 2016.
- [116] M. S. Saleh, J. Li, J. Park, and R. Panat, “3D printed hierarchically-porous microlattice electrode materials for exceptionally high specific capacity and areal capacity lithium ion batteries,” *Additive Manufacturing*, vol. 23, pp. 70–78, 2018.
- [117] Y. Zhu, J. Li, M. S. Saleh, H. Pham, T. P. Plateau, R. Panat, and J. Park, “Towards high-performance Li-ion batteries via optimized three-dimensional micro-lattice electrode architectures,” *Journal of Power Sources*, vol. 476, 2020.
- [118] C. Xu, B. M. Gallant, P. U. Wunderlich, T. Lohmann, and J. R. Greer, “Three-Dimensional Au Microlattices as Positive Electrodes for Li-O<sub>2</sub> Batteries,” *ACS Nano*, vol. 9, no. 6, pp. 5876–5883, 2015.
- [119] M. Bici, S. Brischetto, F. Campana, C. G. Ferro, C. Seclì, S. Varetto, P. Maggiore, and A. Mazza, “Development of a multifunctional panel for aerospace use through SLM additive manufacturing,” in *11th CIRP Conference on Intelligent Computation in Manufacturing Engineering, CIRP ICME '17 Development*, vol. 67, pp. 215–220, 2018.
- [120] J. Bühring, M. Nuño, and K.-U. Schröder, “Additive manufactured sandwich structures: Mechanical characterization and usage potential in small aircraft,” *Aerospace Science and Technology*, vol. 111, apr 2021.
- [121] M. Khorasani, A. H. Ghasemi, B. Rolfe, and I. Gibson, “Additive manufacturing a powerful tool for the aerospace industry,” *Rapid Prototyping Journal*, vol. 28, no. 1, pp. 87–100, 2022.
- [122] A. Kantaros and D. Piromalis, “Fabricating Lattice Structures via 3D Printing: The Case of Porous Bio-Engineered Scaffolds,” *Applied Mechanics*, vol. 2, no. 2, pp. 289–302, 2021.
- [123] B. I. Oladapo, S. A. Zahedi, and S. O. Ismail, “Mechanical performances of hip implant design and fabrication with PEEK composite,” *Polymer*, vol. 227, p. 123865, jun 2021.
- [124] J. A. Tamayo, M. Riascos, C. A. Vargas, and L. M. Baena, “Additive manufacturing of Ti6Al4V alloy via electron beam melting for the development of implants for the biomedical industry,” *Heliyon*, vol. 7, no. 5, 2021.
-



- 
- [125] F. Caiazzo, V. Alfieri, and B. D. Bujazha, “Additive manufacturing of biomorphic scaffolds for bone tissue engineering,” *International Journal of Advanced Manufacturing Technology*, vol. 113, no. 9-10, pp. 2909–2923, 2021.
- [126] J. Feng, B. Liu, Z. Lin, and J. Fu, “Isotropic octet-truss lattice structure design and anisotropy control strategies for implant application,” *Materials and Design*, vol. 203, p. 109595, may 2021.
- [127] N. Sharma, D. Ostas, H. Rotar, P. Brantner, and F. M. Thieringer, “Design and Additive Manufacturing of a Biomimetic Customized Cranial Implant Based on Voronoi Diagram,” *Frontiers in Physiology*, vol. 12, no. April, pp. 1–12, 2021.
- [128] M. J. Munford, D. Xiao, and J. R. Jeffers, “Lattice implants that generate homeostatic and remodeling strains in bone,” *Journal of Orthopaedic Research*, no. February, pp. 1–7, 2021.
- [129] A. Kovalcik, L. Sangroniz, M. Kalina, K. Skopalova, P. Humpolíček, M. Omastova, N. Mundigler, and A. J. Müller, “Properties of scaffolds prepared by fused deposition modeling of poly(hydroxyalkanoates),” *International Journal of Biological Macromolecules*, vol. 161, pp. 364–376, oct 2020.
- [130] H. M. Eltaher, F. E. Abukunna, L. Ruiz-Cantu, Z. Stone, J. Yang, and J. E. Dixon, “Human-scale tissues with patterned vascular networks by additive manufacturing of sacrificial sugar-protein composites,” *Acta Biomaterialia*, vol. 113, pp. 339–349, sep 2020.
- [131] T. Funkhouser, “Curved Surfaces,” 1999.
- [132] A. Ceruti, R. Ferrari, and A. Liverani, “Design for Additive Manufacturing Using LSWM: A CAD Tool for the Modelling of Lightweight and Lattice Structures,” in *International Conference on Sustainable Design and Manufacturing*, vol. 68, pp. 756–765, 2017.
- [133] A. H. Azman, F. Vignat, and F. Villeneuve, “CAD tools and file format performance evaluation in designing lattice structures for additive manufacturing,” *Jurnal Teknologi*, vol. 80, no. 4, pp. 87–95, 2018.
- [134] Y. Chahid, R. Racasan, L. Pagani, A. Townsend, A. Liu, P. Bills, and L. Blunt, “Parametrically designed surface topography on CAD models of additively manufactured lattice structures for improved design validation,” *Additive Manufacturing*, vol. 37, p. 101731, jan 2021.
- [135] M. Schmitt and I. Y. Kim, “Schmitt–Kim additive manufacturing evaluation tree: a guide for new users,” *Progress in Additive Manufacturing*, no. 0123456789, 2021.
-

- 
- [136] “All3DP,” 2022. <https://all3dp.com/2/infill-3d-printing-what-it-means-and-how-to-use-it>.
- [137] N. Papakostas, A. Newell, and A. George, “An Agent-Based Decision Support Platform for Additive Manufacturing Applications,” *Applied Sciences*, vol. 10, jul 2020.
- [138] J. Podroužek, M. Marcon, K. Ninčević, and R. Wan-Wendner, “Bio-inspired 3D infill patterns for additive manufacturing and structural applications,” *Materials*, vol. 12, no. 3, pp. 1–12, 2019.
- [139] C. Sigg, *Representation and rendering of implicit surfaces*. PhD thesis, ETH Zurich, 2006.
- [140] W. Zha and S. Anand, “Geometric approaches to input file modification for part quality improvement in additive manufacturing,” *Journal of Manufacturing Processes*, vol. 20, pp. 465–477, 2015.
- [141] R. Olszewski, P. Szymor, and M. Kozakiewicz, “Accuracy of three-dimensional , paper-based models generated using a low-cost , three-dimensional printer,” *Journal of Cranio-Maxillofacial Surgery*, vol. 42, no. 8, pp. 1847–1852, 2014.
- [142] “Fusion 360 with NetFabb,” 2022. <https://www.autodesk.co.uk>.
- [143] C. K. Lee, H. D. Hwang, and S. H. Yoon, “Bézier triangles with G2 continuity across boundaries,” *Symmetry*, vol. 8, no. 3, pp. 1–12, 2016.
- [144] S. Liu, T. Liu, Q. Zou, W. Wang, E. L. Doubrovski, and C. C. Wang, “Memory-Efficient Modeling and Slicing of Large-Scale Adaptive Lattice Structures,” *Journal of Computing and Information Science in Engineering*, vol. 21, no. 6, pp. 1–16, 2021.
- [145] S. Valette, J. M. Chassery, and R. Prost, “Generic remeshing of 3D triangular meshes with metric-dependent discrete voronoi diagrams,” *IEEE Transactions on Visualization and Computer Graphics*, vol. 14, no. 2, pp. 369–381, 2008.
- [146] L. Chougrani, J.-p. Pernot, P. Véron, and S. Abed, “Lattice structure lightweight triangulation for additive manufacturing,” *Computer-Aided Design*, vol. 90, pp. 95–104, sep 2017.
- [147] R. Paul and S. Anand, “A new Steiner patch based file format for Additive Manufacturing processes,” *Computer-Aided Design*, vol. 63, pp. 86–100, 2015.
- [148] G. H. Loh, E. Pei, D. Harrison, and M. D. Monzón, “An overview of functionally graded additive manufacturing,” *Additive Manufacturing*, vol. 23, pp. 34–44, 2018.
-

- 
- [149] A. Tibaut, D. Rebolj, and M. Nekrep, "Interoperability requirements for automated manufacturing systems in construction," *Intelligent Manufacturing*, vol. 27, pp. 251–262, 2016.
- [150] C. Iancu, "About 3D Printing File Formats," *Annals of the Constantin Brancusi University of Targu Jiu*, no. 2, pp. 135–138, 2018.
- [151] Y. Qin, Q. Qi, P. J. Scott, and X. Jiang, "Status, comparison, and future of the representations of additive manufacturing data," *Computer Aided Design*, vol. 111, pp. 44–64, 2019.
- [152] G. Savio, R. Meneghello, S. Rosso, and G. Concheri, "3D Model Representation and Data Exchange for Additive Manufacturing," in *International Journal on Interactive Design and Manufacturing*, vol. 12, pp. 412–421, Springer, 2019.
- [153] R. Bonnard, J. Y. Hascoët, P. Mognol, and I. Stroud, "STEP-NC digital thread for additive manufacturing: data model, implementation and validation," *International Journal of Computer Integrated Manufacturing*, vol. 31, no. 11, pp. 1141–1160, 2018.
- [154] R. Vaidya and S. Anand, "Image Processing Assisted Tools for Pre- and Post-processing Operations in Additive Manufacturing," *Procedia Manufacturing*, vol. 5, pp. 958–973, 2016.
- [155] "3MF Beam Lattice Extension About this Specification Part I : 3MF Documents Chapter 1 . Overview of Additions," 2018.
- [156] E. Maltsev, D. Popov, S. Chugunov, A. Pasko, and I. Akhatov, "An Accelerated Slicing Algorithm for Frep Models," *Applied Sciences*, vol. 11, no. 15, 2021.
- [157] K. M. Nsiempba, M. Wang, and M. Vlasea, "Geometrical degrees of freedom for cellular structures generation: A new classification paradigm," *Applied Sciences*, vol. 11, no. 9, 2021.
- [158] "3MF Consortium Announces Volumetric Design Support, Grows Adoption of 3D Printing Specification," 2021.
- [159] W. E. Lorensen and H. E. Cline, "Marching cubes: A high resolution 3D surface construction algorithm," *Computer Graphics*, vol. 21, no. 4, pp. 163–169, 1987.
- [160] C. Maple, "Geometric design and space planning using the marching squares and marching cube algorithms," in *Proceedings - 2003 International Conference on Geometric Modeling and Graphics, GMAG, IEEE*, pp. 90–95, 2003.
-

- 
- [161] T. S. Newman and H. Yi, “A survey of the marching cubes algorithm,” *Computers & Graphics*, vol. 30, pp. 854–879, oct 2006.
  - [162] Y. Song, Z. Yang, Y. Liu, and J. Deng, “Function representation based slicer for 3D printing,” *Computer Aided Geometric Design*, vol. 62, pp. 276–293, 2018.
  - [163] J. C. Steuben, A. P. Iliopoulos, and J. G. Michopoulos, “Implicit slicing for functionally tailored additive manufacturing,” *CAD Computer Aided Design*, vol. 77, pp. 107–119, 2016.
  - [164] D. Adams and C. J. Turner, “An implicit slicing method for additive manufacturing processes,” *Virtual and Physical Prototyping*, jan 2017.
  - [165] Y. Zhang, S. Tan, L. Ding, and A. Bernard, “A toolpath-based layer construction method for designing and printing porous structure,” *CIRP Annals - Manufacturing Technology*, vol. 70, no. 1, pp. 123–126, 2021.
  - [166] “Creo: Design,” 2022. <https://www.ptc.com/en/products/creo>.
  - [167] “Materialise 3-matic,” 2022. <https://www.materialise.com/en/software/3-matic>.
  - [168] “Carbon Design Engine,” 2022. <https://www.carbon3d.com/products/carbon-design-engine>.
  - [169] “Ansys SpaceClaim,” 2022. <https://www.ansys.com/en-gb/products/3d-design/ansys-spaceclaim>.
  - [170] “NX,” 2022. <https://www.plm.automation.siemens.com>.
  - [171] I. Maskery, L. Parry, D. Padrão, R. Hague, and I. Ashcroft, “FLatt Pack: A research-focussed lattice design program,” *Additive Manufacturing*, vol. 49, 2022.
  - [172] “Rhino3D,” 2022. <https://www.rhino3d.com>.
  - [173] “Gen3D,” 2022. <https://gen3d.com/>.
  - [174] “nTopology,” 2022. <https://ntopology.com>.
  - [175] H. Karcher and K. Polthier, “Construction of Triply Periodic Minimal Surfaces,” *The Royal Society*, pp. 2077–2104, 1996.
  - [176] H. A. Schwarz, *Gesammelte Mathematische Abhandlungen*. American Mathematical Soc., 260 ed., 1972.
  - [177] E. R. Neovius, *Bestimmung zweier speciellen periodischen Minimalflächen*, *Helsingfors: Akad. Abhandlungen*, 1883.
-

- 
- [178] A. H. Schoen, “Infinite Periodic Minimal Surfaces Without Self-Intersections,” tech. rep., NASA, 1970.
- [179] H. Karcher, “The triply periodic minimal surfaces of Alan Schoen and their constant mean curvature companions,” *Manuscripta Mathematica*, vol. 64, no. 3, pp. 291–357, 1989.
- [180] Y. Wang, “Degree Elevation and Reduction of Periodic Surfaces,” *Computer-Aided Design and Applications*, vol. 5, pp. 841–854, jan 2008.
- [181] M. Afshar, A. P. Anaraki, H. Montazerian, and J. Kadkhodapour, “Additive manufacturing and mechanical characterization of graded porosity scaffolds designed based on triply periodic minimal surface architectures,” *Journal of the Mechanical Behavior of Biomedical Materials*, vol. 62, pp. 481–494, 2016.
- [182] M. Keshavarzan, M. Kadkhodaei, M. Badrossamay, and M. Karamooz Ravari, “Investigation on the failure mechanism of triply periodic minimal surface cellular structures fabricated by Vat photopolymerization additive manufacturing under compressive loadings,” *Mechanics of Materials*, vol. 140, jan 2020.
- [183] S. Lidin and S. Larsson, “Bonnet Transformation of Infinite Periodic Minimal Surfaces with Hexagonal Symmetry,” *J. Chem. Soc. Faraday Trans.*, vol. 86, no. 916, pp. 769–775, 1990.
- [184] H. Terrones, “Computation of Minimal Surfaces,” *Journal de Physique Colloques*, vol. 51, 1990.
- [185] P. J. F. Gandy and J. Klinowski, “Exact computation of the triply periodic Schwarz P minimal surface,” *Chemical Physics Letters*, no. December, pp. 543–551, 2000.
- [186] P. J. F. Gandy and J. Klinowski, “Exact computation of the triply periodic G (‘Gyroid’) minimal surface,” *Chemical Physics Letters*, no. December, pp. 363–371, 2000.
- [187] P. J. F. Gandy, D. Cvijović, A. L. Mackay, and J. Klinowski, “Exact computation of the triply period D (‘diamond’) minimal surface,” *Chemical Physics Letters*, vol. 314, pp. 543–551, 1999.
- [188] P. Anderson, David M., Ström, “Polymerized Lyotropic Liquid Crystals As Contact Lens Materials,” *Physica A*, vol. 176, pp. 151–167, 1991.
- [189] M. E. Davis, “Organizing for better synthesis,” *Nature*, vol. 364, pp. 391–393, 1993.
-

- 
- [190] T. Landh, "From entangled membranes to eclectic morphologies: cubic membranes as subcellular space organizers," *FEBS Letters*, vol. 369, pp. 13–17, 1995.
- [191] Y. Deng and T. Landh, "The Cubic Gyroid-based Membrane Structure of the Chloroplast in *Zygnema* (Chlorophyceae zygnematles)," *Zoological Studies*, vol. 34, 1995.
- [192] J. Charvolin and J. F. Sadoc, "Periodic Systems of Frustrated Fluid Films and 'Micellar' Cubic Structures in Liquid Crystals," *Journal de Physique*, vol. 48, no. 9, pp. 1559–1569, 1987.
- [193] Y. Bouligand, "Comparative Geometry of Cytomembranes and Water-Lipid Systems," *Le Journal de Physique Colloques*, vol. 51, 1990.
- [194] H.-U. Nissen, "Crystal Orientation and Plate Structure in Echinoid Skeletal Units," *Advancement Of Science*, vol. 166, no. 3909, pp. 1150–1152, 1969.
- [195] O. Al-Ketan, R. Rowshan, and R. K. Abu Al-Rub, "Topology-mechanical property relationship of 3D printed strut, skeletal, and sheet based periodic metallic cellular materials," *Additive Manufacturing*, vol. 19, pp. 167–183, 2018.
- [196] F. Liu, Z. Mao, P. Zhang, D. Z. Zhang, J. Jiang, and Z. Ma, "Functionally graded porous scaffolds in multiple patterns: New design method, physical and mechanical properties," *Materials and Design*, vol. 160, pp. 849–860, 2018.
- [197] I. Maskery, A. O. Aremu, L. Parry, R. D. Wildman, C. J. Tuck, and I. A. Ashcroft, "Effective design and simulation of surface-based lattice structures featuring volume fraction and cell type grading," *Materials and Design*, vol. 155, pp. 220–232, 2018.
- [198] D. Li, W. Liao, N. Dai, G. Dong, Y. Tang, and Y. Min, "Computer-Aided Design Optimal design and modeling of gyroid-based functionally graded cellular structures for additive manufacturing," *Computer-Aided Design*, vol. 104, pp. 87–99, 2018.
- [199] N. Strömberg, "Optimal grading of TPMS-based lattice structures with transversely isotropic elastic bulk properties," *Engineering Optimization*, vol. 0, no. 0, pp. 1–14, 2020.
- [200] S. Ma, K. Song, J. Lan, and L. Ma, "Biological and mechanical property analysis for designed heterogeneous porous scaffolds based on the refined TPMS," *Journal of the Mechanical Behavior of Biomedical Materials*, vol. 107, no. February, 2020.
-

- 
- [201] S. Ma, Q. Tang, X. Han, Q. Feng, J. Song, R. Setchi, Y. Liu, Y. Liu, A. Goulas, D. S. Engström, Y. Y. Tse, and N. Zhen, “Manufacturability, Mechanical Properties, Mass-Transport Properties and Biocompatibility of Triply Periodic Minimal Surface (TPMS) Porous Scaffolds Fabricated by Selective Laser Melting,” *Materials and Design*, vol. 195, oct 2020.
- [202] K. Song, Z. Wang, J. Lan, and S. Ma, “Porous structure design and mechanical behavior analysis based on TPMS for customized root analogue implant,” *Journal of the Mechanical Behavior of Biomedical Materials*, vol. 115, no. July 2020, 2021.
- [203] S. Saghaian, A. Amerinatanzi, N. Moghaddam, A. Majumdar, M. Nematollahi, S. Saedi, M. Elahinia, and H. Karaca, “Mechanical and shape memory properties of triply periodic minimal surface (TPMS) NiTi structures fabricated by selective laser melting,” *Biology, Engineering and Medicine*, vol. 3, no. 5, pp. 1–7, 2019.
- [204] D. W. Abueidda, M. Bakir, R. K. Abu Al-Rub, J. S. Bergström, N. A. Sobh, and I. Jasiuk, “Mechanical properties of 3D printed polymeric cellular materials with triply periodic minimal surface architectures,” *Materials and Design*, vol. 122, pp. 255–267, 2017.
- [205] E. Yang, M. Leary, B. Lozanovski, D. Downing, M. Mazur, A. Sarker, A. M. Khorasani, A. Jones, T. Maconachie, S. Bateman, M. Easton, M. Qian, P. Choong, and M. Brandt, “Effect of geometry on the mechanical properties of Ti-6Al-4V Gyroid structures fabricated via SLM: A numerical study,” *Materials and Design*, vol. 184, p. 108165, 2019.
- [206] M. Sychoy, L. Lebedev, S. Dyachenko, and L. Nefedova, “Mechanical properties of energy-absorbing structures with triply periodic minimal surface topology,” *Acta Astronautica*, vol. 150, pp. 81–84, sep 2018.
- [207] Z. Cai, Z. Liu, X. Hu, H. Kuang, and J. Zhai, “The effect of porosity on the mechanical properties of 3D-printed triply periodic minimal surface (TPMS) bioscaffold,” *Bio-Design and Manufacturing*, vol. 2, no. 4, pp. 242–255, 2019.
- [208] R. Sankineni and Y. R. Kumar, “Evaluation of energy absorption capabilities and mechanical properties in FDM printed PLA TPMS structures,” *Proceedings of the Institution of Mechanical Engineers, Part C: Journal of Mechanical Engineering Science*, 2021.
- [209] D. A. de Aquino, I. Maskery, G. A. Longhitano, A. L. Jardini, and E. G. del Conte, “Investigation of load direction on the compressive strength of additively manufactured triply periodic minimal surface scaffolds,” *International Journal of Advanced Manufacturing Technology*, vol. 109, no. 3-4, pp. 771–779, 2020.
-

- 
- [210] S. Higuera, R. Miralbes, and D. Ranz, “Mechanical properties and energy-absorption capabilities of thermoplastic sheet gyroid structures,” *Mechanics of Advanced Materials and Structures*, pp. 1–15, may 2021.
- [211] C. Yan, L. Hao, A. Hussein, P. Young, J. Huang, and W. Zhu, “Microstructure and mechanical properties of aluminium alloy cellular lattice structures manufactured by direct metal laser sintering,” *Materials Science and Engineering A*, vol. 628, pp. 238–246, 2015.
- [212] Y. Tripathi, M. Shukla, and A. D. Bhatt, “Implicit-Function-Based Design and Additive Manufacturing of Triply Periodic Minimal Surfaces Scaffolds for Bone Tissue Engineering,” *Journal of Materials Engineering and Performance*, vol. 28, no. 12, pp. 7445–7451, 2019.
- [213] S. Z. Khan, S. H. Masood, E. Ibrahim, and Z. Ahmad, “Compressive behaviour of Neovius Triply Periodic Minimal Surface cellular structure manufactured by fused deposition modelling,” *Virtual and Physical Prototyping*, vol. 14, no. 4, pp. 360–370, 2019.
- [214] Z. Wang, X. Wang, T. Gao, and C. Shi, “Mechanical behavior and deformation mechanism of triply periodic minimal surface sheet under compressive loading,” *Mechanics of Advanced Materials and Structures*, vol. 0, no. 0, pp. 1–13, 2020.
- [215] A. S. Dalaq, D. W. Abueidda, R. K. A. Al-rub, and I. Jasiuk, “Finite element prediction of effective elastic properties of interpenetrating phase composites with architected 3D sheet reinforcements,” *International Journal of Solids and Structures*, vol. 83, pp. 169–182, 2016.
- [216] D. W. Lee, K. A. Khan, and R. K. Abu Al-Rub, “Stiffness and yield strength of architected foams based on the Schwarz Primitive triply periodic minimal surface,” *International Journal of Plasticity*, vol. 95, pp. 1–20, 2017.
- [217] S. Vijayavenkataraman, L. Zhang, S. Zhang, J. Y. H. Fuh, and W. F. Lu, “Triply Periodic Minimal Surfaces Sheet Scaffolds for Tissue Engineering Applications: An Optimization Approach Toward Biomimetic Scaffold Design,” *ACS Applied Bio Materials*, vol. 1, no. 2, pp. 259–269, 2018.
- [218] S. C. Kapfer, S. T. Hyde, K. Mecke, C. H. Arns, and G. E. Schröder-Turk, “Minimal surface scaffold designs for tissue engineering,” *Biomaterials*, vol. 32, no. 29, pp. 6875–6882, 2011.
- [219] B. D. Nguyen, S. C. Han, Y. C. Jung, and K. Kang, “Design of the P-surfaced shellular, an ultra-low density material with micro-architecture,” *Computational Materials Science*, vol. 139, pp. 162–178, 2017.
- [220] W. Jiang, W. Liao, T. Liu, X. Shi, C. Wang, J. Qi, Y. Chen, Z. Wang, and C. Zhang, “A voxel-based method of multiscale mechanical property
-



- optimization for the design of graded TPMS structures,” *Materials and Design*, vol. 204, p. 109655, 2021.
- [221] Y. Jung and S. Torquato, “Fluid permeabilities of triply periodic minimal surfaces,” *Physical Review E - Statistical, Nonlinear, and Soft Matter Physics*, vol. 72, no. 5, pp. 1–8, 2005.
- [222] Z. Cheng, R. Xu, and P.-X. Jiang, “Morphology, flow and heat transfer in triply periodic minimal surface based porous structures,” *International Journal of Heat and Mass Transfer*, vol. 170, p. 120902, 2021.
- [223] W. Yang, J. An, C. K. Chua, and K. Zhou, “Acoustic absorptions of multifunctional polymeric cellular structures based on triply periodic minimal surfaces fabricated by stereolithography,” *Virtual and Physical Prototyping*, vol. 15, no. 2, pp. 242–249, 2020.
- [224] R. Ďuriš and E. Labašová, “The design of an impedance tube and testing of sound absorption coefficient of selected materials,” in *IOP Conference Series: Materials Science and Engineering*, vol. 1050, 2021.
- [225] D. W. Abueidda, R. K. Abu Al-Rub, A. S. Dalaq, D. W. Lee, K. A. Khan, and I. Jasiuk, “Effective conductivities and elastic moduli of novel foams with triply periodic minimal surfaces,” *Mechanics of Materials*, vol. 95, pp. 102–115, 2016.
- [226] D. W. Abueidda, A. S. Dalaq, R. K. Abu Al-Rub, and H. A. Younes, “Finite element predictions of effective multifunctional properties of interpenetrating phase composites with novel triply periodic solid shell architected reinforcements,” *International Journal of Mechanical Sciences*, vol. 92, pp. 80–89, mar 2015.
- [227] D. W. Abueidda, A. S. Dalaq, R. K. Abu Al-Rub, and I. Jasiuk, “Micromechanical finite element predictions of a reduced coefficient of thermal expansion for 3D periodic architected interpenetrating phase composites,” *Composite Structures*, vol. 133, pp. 85–97, dec 2015.
- [228] D.-J. Yoo, “Advanced Porous Scaffold Design using Multi-Void Triply Periodic Minimal Surface Models with High Surface Area to Volume Ratios,” *International Journal of Precision Engineering and Manufacturing*, vol. 15, no. 8, pp. 1657–1666, 2014.
- [229] J. Feng, J. Fu, Z. Lin, C. Shang, and X. Niu, “Layered infill area generation from triply periodic minimal surfaces for additive manufacturing,” *Computer Aided Design*, vol. 107, pp. 50–63, 2019.
- [230] Z. Wang, Y. Zhang, and A. Bernard, “A Novel Knowledge-Based Tool-path Constructive Approach For Designing High-Precision Graded Lattice Structures,” in *Solid Freeform Fabrication 2021: Proceedings of the 32nd Annual International*, pp. 1185–1201, 2021.

- 
- [231] Z. Chen, Y. M. Xie, X. Wu, Z. Wang, Q. Li, and S. Zhou, “On hybrid cellular materials based on triply periodic minimal surfaces with extreme mechanical properties,” *Materials and Design*, vol. 183, 2019.
- [232] L. Hao, D. Raymont, C. Yan, A. Hussein, and P. Young, “Design and additive manufacturing of cellular lattice structures,” *Innovative Developments in Virtual and Physical Prototyping*, no. November 2014, pp. 249–254, 2011.
- [233] G. Savio, R. Meneghello, and G. Concheri, “Design of variable thickness triply periodic surfaces for additive manufacturing,” *Progress in Additive Manufacturing*, vol. 4, no. 3, pp. 281–290, 2019.
- [234] D. Montoya-Zapata, A. Moreno, J. Pareja-Corcho, J. Posada, and O. Ruiz-Salguero, “Density-Sensitive Implicit Functions Using Sub-Voxel Sampling in Additive Manufacturing,” *Metals*, vol. 9, p. 1293, nov 2019.
- [235] “Materialise Magics.” <https://www.materialise.com/en/software/magics>.
- [236] A. R. Nassar and E. W. Reutzel, “A proposed digital thread for additive manufacturing,” in *24th International Solid Freeform Fabrication Symposium*, (University of Texas at Austin), pp. 19–43, 2013.
- [237] A. Sherstyuk, “Fast ray tracing of implicit surfaces,” *Computer Graphics Forum*, vol. 18, no. 2, pp. 139–148, 1999.
- [238] GitLab repository of TPMS geometric properties [https://gitlab.com/Soo-Hwa\\_Kim/tpms-geometric-properties](https://gitlab.com/Soo-Hwa_Kim/tpms-geometric-properties).
- [239] GitLab repository of CAM program [https://gitlab.com/Soo-Hwa\\_Kim/tpms-geom-slicer](https://gitlab.com/Soo-Hwa_Kim/tpms-geom-slicer).
- [240] M. F. Ashby and L. J. Gibson, *Cellular solids: structure and properties*. Cambridge, UK: Press Syndicate of the University of Cambridge, 1997.
- [241] “ISO 604 Plastics — Determination of compressive properties,” 2003.
- [242] S. S. Du, C. Jin, J. D. Lee, M. I. Jordan, B. Póczos, and A. Singh, “Gradient descent can take exponential time to escape saddle points,” in *Conference on Neural Information Processing Systems*, pp. 1068–1078, 2017.
- [243] C. Zhang and T. Chen, “Efficient feature extraction for 2D/3D objects in mesh representation,” in *Proceedings 2001 International Conference on Image Processing, IEEE*, pp. 935–938, 2001.
- [244] X. Li, W. Wang, R. R. Martin, and A. Bowyer, “Using low-discrepancy sequences and the Crofton formula to compute surface areas of geometric models,” *CAD Computer Aided Design*, vol. 35, no. 9, pp. 771–782, 2003.
-

- 
- [245] H. Niederreiter, “Quasi-Monte Carlo Methods and Pseudo-Random Numbers,” *Bulletin of the American Mathematical Society*, vol. 84, no. 6, pp. 957–1041, 1978.
- [246] L. Y. Deng and D. Bowman, “Developments in pseudo-random number generators,” *Wiley Interdisciplinary Reviews: Computational Statistics*, vol. 9, no. 5, 2017.
- [247] N. A. Mohammed, Q.-m. C. Sobol, and N. A. Mohammed, “Comparing Halton and Sobol Sequences in Integral Evaluation,” *Zanco Journal of Pure and Applied Sciences*, vol. 31, no. 1, pp. 32–39, 2019.
- [248] C. B. Moler, *Numerical Computing with MATLAB*. SIAM, 2010.
- [249] H. C. Chia, J. C. Po, J. C. C. Fei, and S. L. Jin, “A comparative study of implementing fast marching method and A\* search for mobile robot path planning in grid environment: Effect of map resolution,” *Proceedings of IEEE Workshop on Advanced Robotics and its Social Impacts, ARSO*, 2007.
- [250] W. Press, S. A. Teukolsky, W. T. Vetterling, and B. P. Flannery, *Numerical Recipes in C: The Art of Scientific Computing (3rd Edition)*. Cambridge University Press, 2007.
- [251] C. P. Robert and G. Casella, *Monte Carlo Statistical Methods*, vol. 2. Springer, 2013.
- [252] F. Neugebauer, I. Polian, and J. P. Hayes, “Building a Better Random Number Generator for Stochastic Computing,” *Proceedings - 20th Euromicro Conference on Digital System Design, DSD 2017*, pp. 1–8, 2017.
- [253] A. J. Conejo and L. Baringo, *Power System Operations*. Power Electronics and Power Systems, Cham: Springer International Publishing, 2018.
- [254] M. Pharr, W. Jakob, and Humpherys, *Physically Based Rendering: From Theory to Implementation*. Morgan Kaufmann, 2016.
- [255] S. P. Radzevich, *Geometry of Surfaces: A Practical Guide for Mechanical Engineers*. Springer International Publishing, 2019.
- [256] J. F. Epperson, “On the Runge Example,” *The American Mathematical Monthly*, vol. 94, pp. 329–341, apr 1987.
- [257] C. J. Demeure, “Fast QR Factorization of Vandermonde Matrices,” *Linear Algebra And Its Applications*, vol. 194, no. 1989, pp. 165–194, 1989.
- [258] J. C. Mason and D. C. Handscomb, *Chevyshev Polynomials*. Chapman and Hall/CRC, 2002.
-

- 
- [259] Kim, S., Stirling, J., Flynn, J., in press. Dataset for "Volume-fraction, surface area and minimum thickness parameters for five triply-periodic minimal surfaces". Bath: University of Bath Research Data Archive. <https://doi.org/10.15125/BATH-00998>.
- [260] T. A. Cowell, "A general method for the comparison of compact heat transfer surfaces," *Journal of Heat Transfer*, vol. 112, no. 2, pp. 288–294, 1990.
- [261] "PrusaSlicer," 2022. <https://www.prusa3d.com/>.
- [262] "prusa3d," 2022. <https://github.com/prusa3d/PrusaSlicer>.
- [263] J. 101:2008, "Evaluation of measurement data — Guide to the expression of uncertainty in measurement," 2008.
- [264] "M3003: Expanded Uncertainty And Coverage Factors for Calculating Uncertainty," 2019.
- [265] M. F. Ashby, "Mechanical Properties of Cellular Solids," *Metallurgical Transactions A*, vol. 14A, no. September, pp. 1755–1769, 1983.
- [266] R. E. Rahal, T. Jeremiah, S. Kim, K. Fraser, O. Pountney, and J. Flynn, "Approximations of Triply Periodic (Minimal) Gyroid Surfaces for use in CAD Modelling and Simulations," 2022. *In preparation*.

# Appendices

# Appendix A

## Appendix: Polynomial Fitting and Residual Plots

Modelling TPMS structures for AM to a design specification was challenging as the relationship between underlying implicit function and the geometric properties was not intuitive. In Chapter 5, the geometric properties (volume fraction, surface area, and minimum thickness) were calculated for five TPMS structures. This was done by varying the implicit function isovalues for single and double surface structures. For each case, Chebyshev polynomial fitting models were produced to establish empirical relationships between the isovalue and the geometric properties.

To show confidence of the fits this Appendix shows how well the polynomial fitting models fit the raw geometric datasets. There are two types of plots for each case. First is a plot showing the polynomial fitting with the raw data. Second is the residual plot also displaying the maximum error. These plots are discussed in Section 5.4.7.

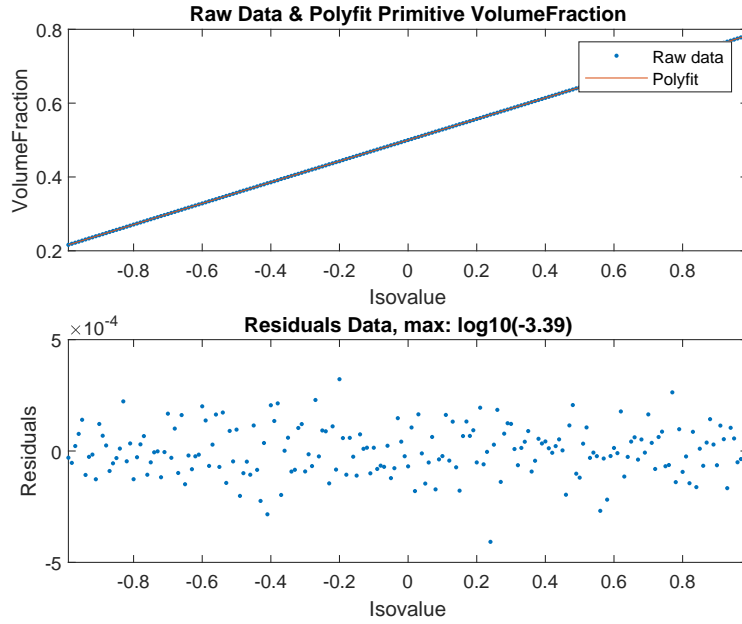


Figure A.1: Primitive single surface structure volume fraction: polynomial fitting with the raw data (top) and residual plot with the maximum error (bottom).

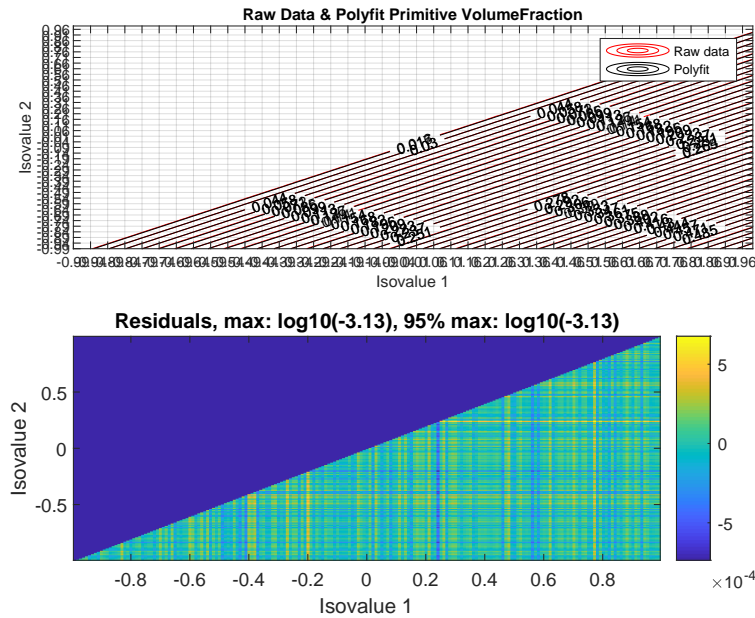


Figure A.2: Primitive double surface structure volume fraction: polynomial fitting with the raw data (top) and residual plot with the maximum error (bottom).

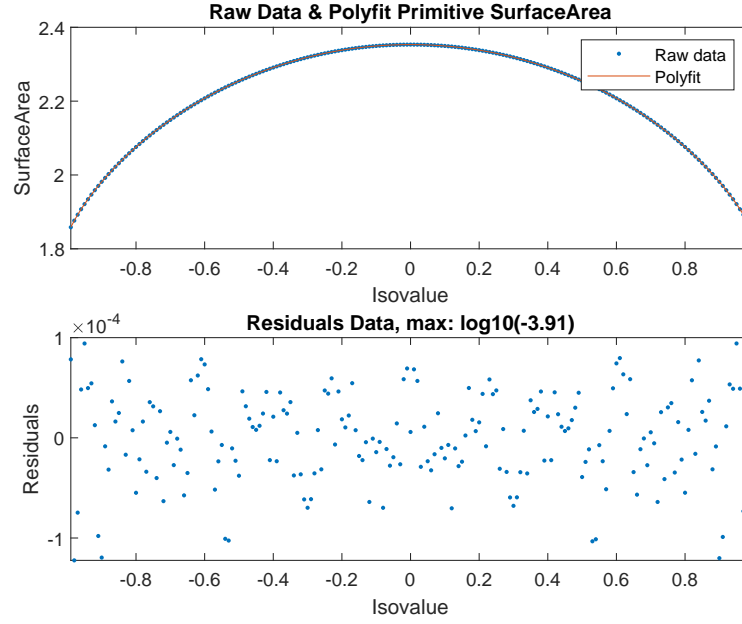


Figure A.3: Primitive single surface structure surface area: polynomial fitting with the raw data (top) and residual plot with the maximum error (bottom).

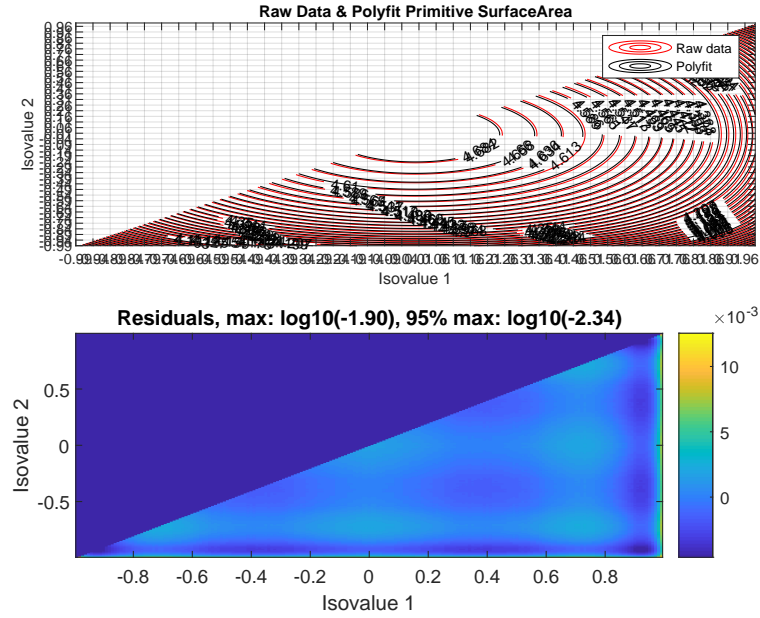


Figure A.4: Primitive double surface structure surface area: polynomial fitting with the raw data (top) and residual plot with the maximum error (bottom).



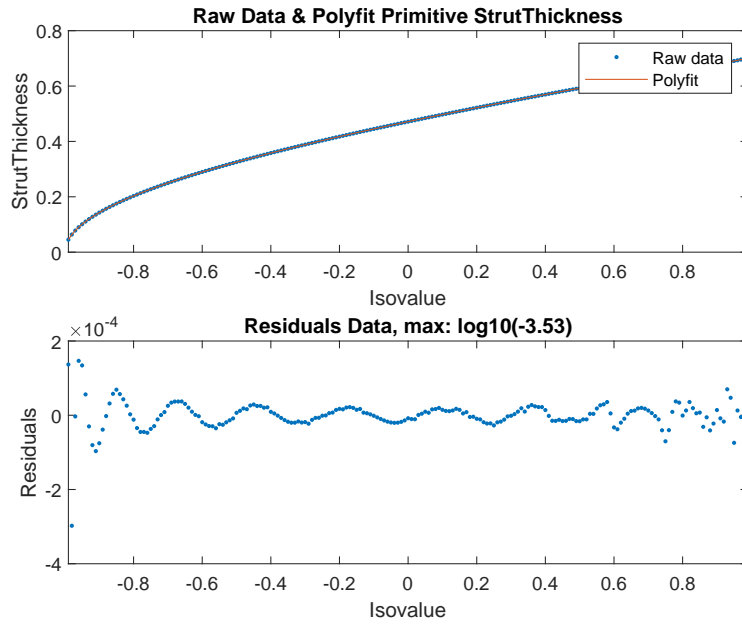


Figure A.5: Primitive single surface structure minimum thickness: polynomial fitting with the raw data (top) and residual plot with the maximum error (bottom).

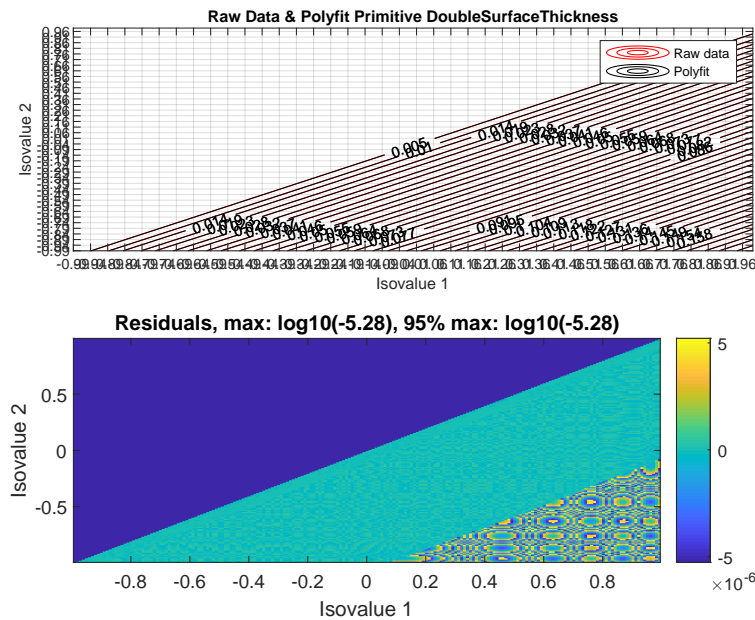


Figure A.6: Primitive double surface structure minimum thickness: polynomial fitting with the raw data (top) and residual plot with the maximum error (bottom).

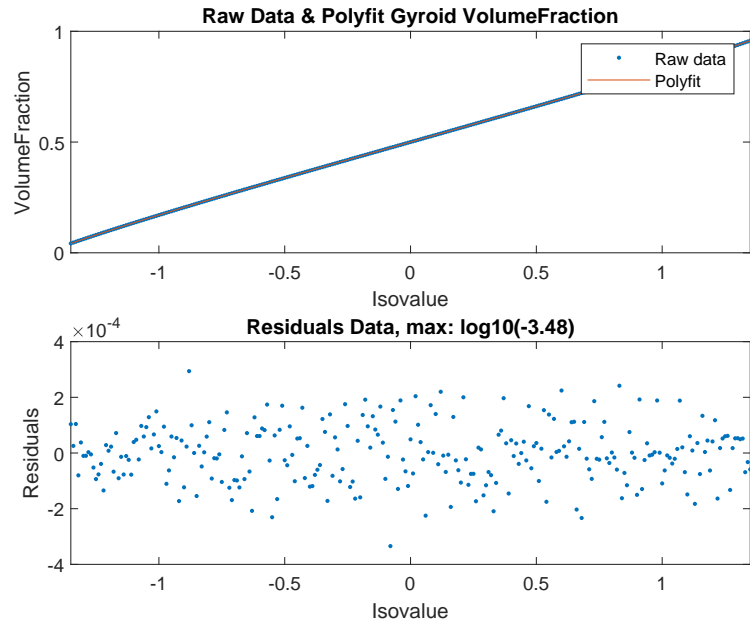


Figure A.7: Gyroid single surface structure volume fraction: polynomial fitting with the raw data (top) and residual plot with the maximum error (bottom).

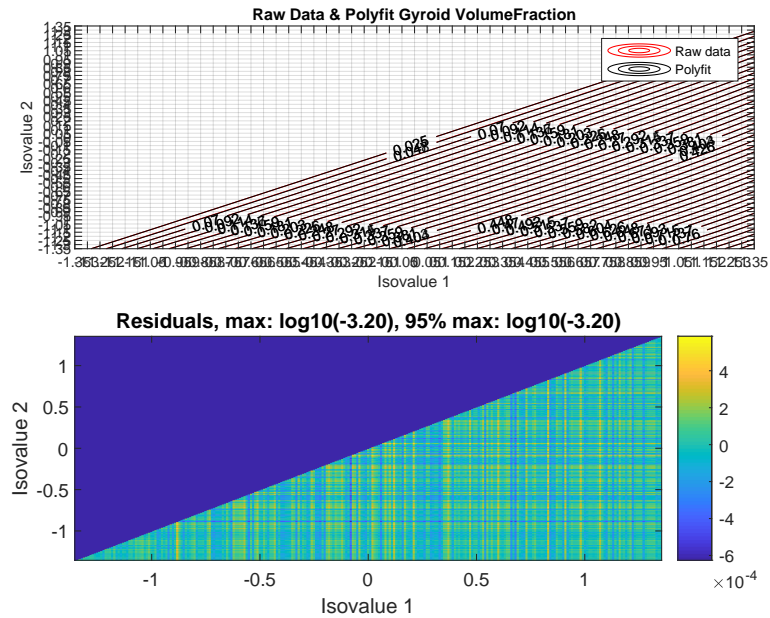


Figure A.8: Gyroid double surface structure volume fraction: polynomial fitting with the raw data (top) and residual plot with the maximum error (bottom).

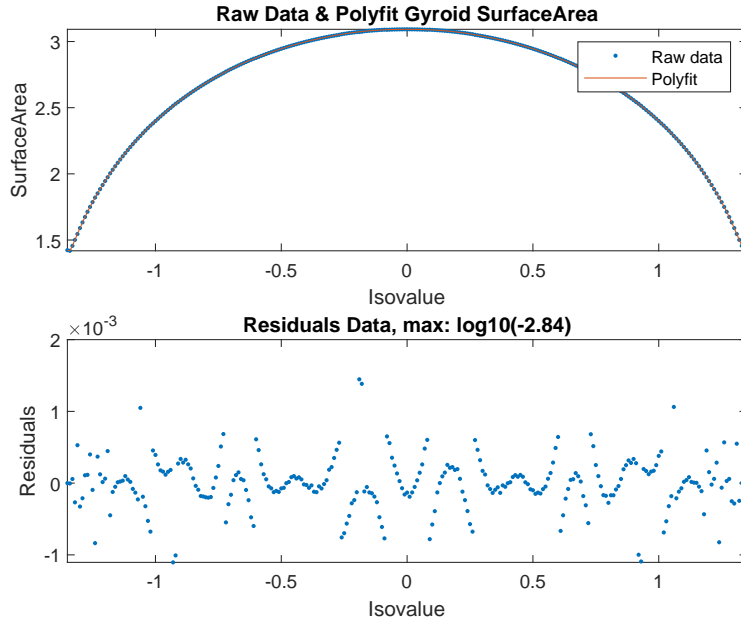


Figure A.9: Gyroid single surface structure surface area: polynomial fitting with the raw data (top) and residual plot with the maximum error (bottom).

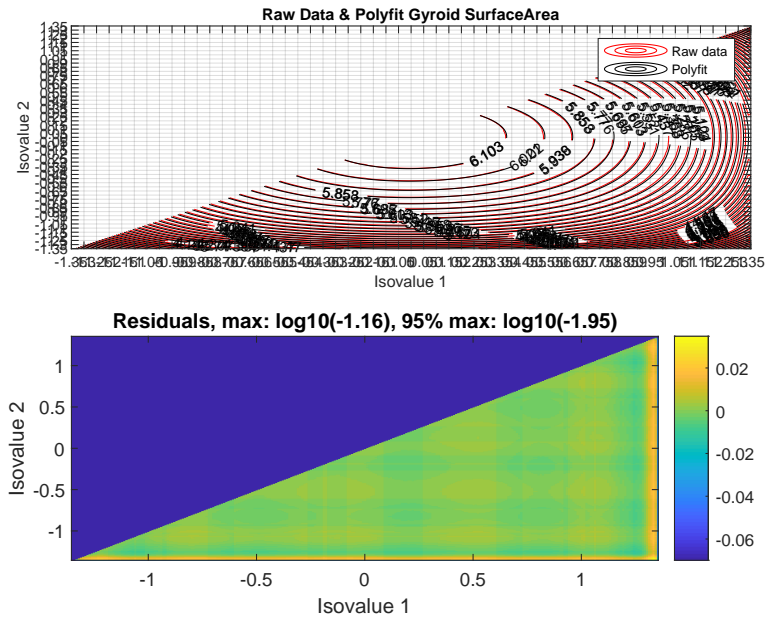


Figure A.10: Gyroid double surface structure surface area: polynomial fitting with the raw data (top) and residual plot with the maximum error (bottom).

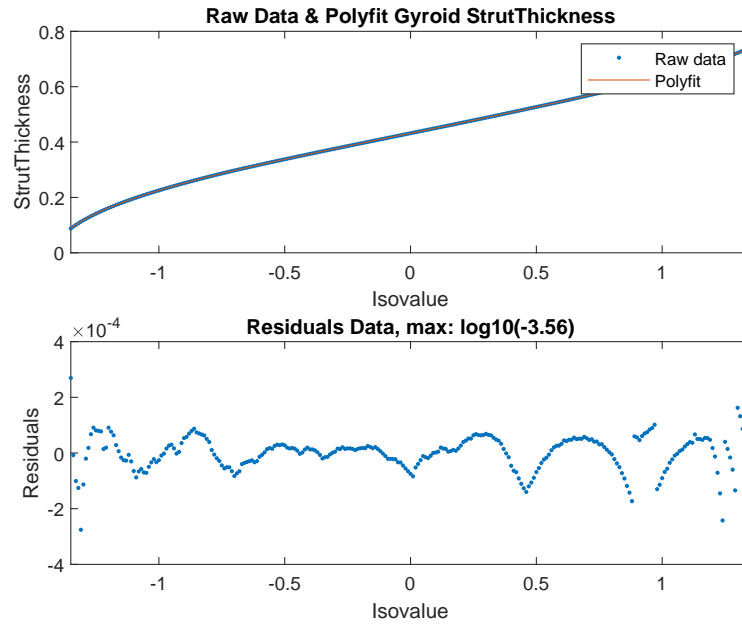


Figure A.11: Gyroid single surface structure minimum thickness: polynomial fitting with the raw data (top) and residual plot with the maximum error (bottom).

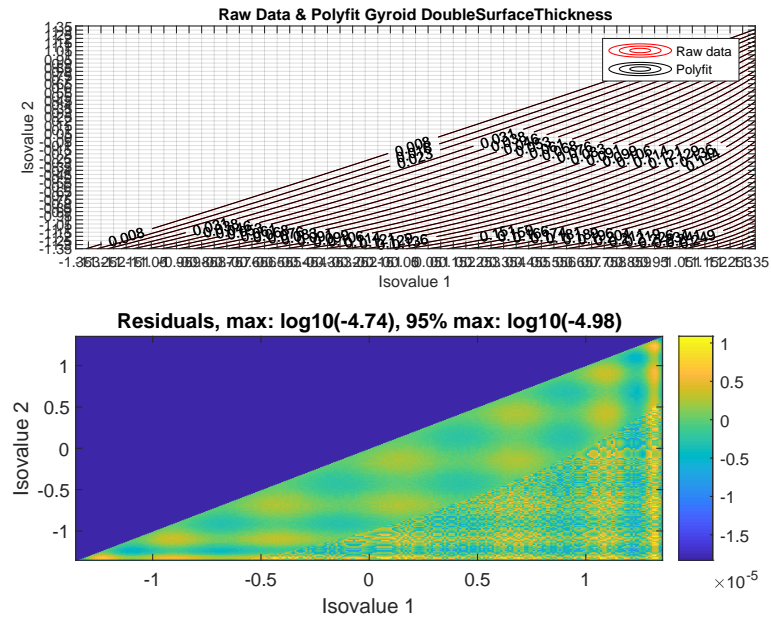


Figure A.12: Gyroid double surface structure minimum thickness: polynomial fitting with the raw data (top) and residual plot with the maximum error (bottom).

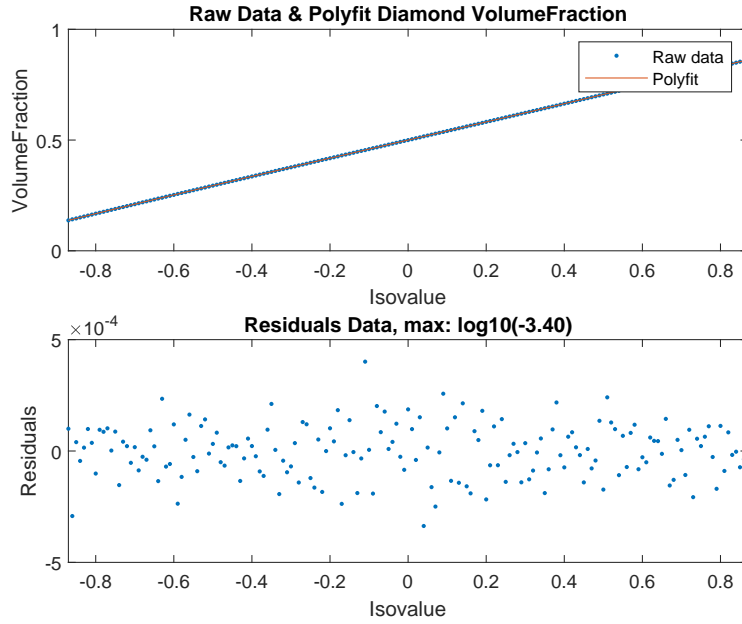


Figure A.13: Diamond single surface structure volume fraction: polynomial fitting with the raw data (top) and residual plot with the maximum error (bottom).

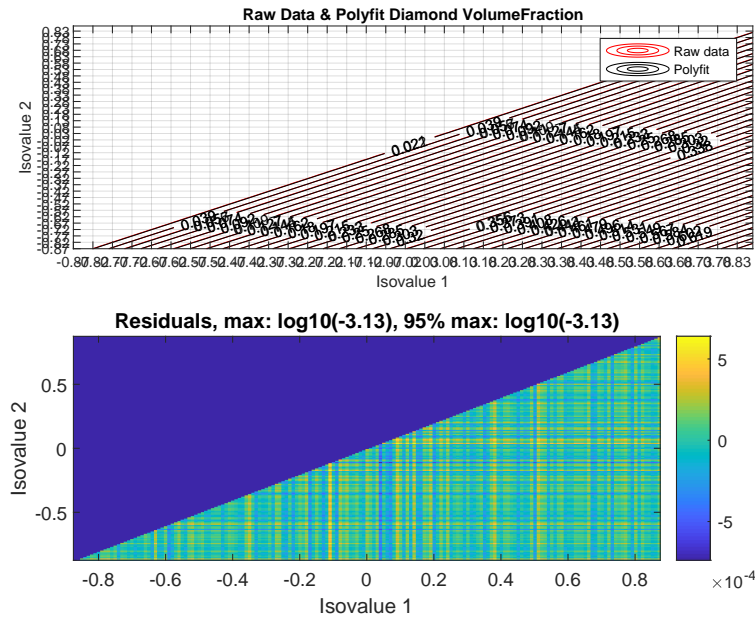


Figure A.14: Diamond double surface structure volume fraction: polynomial fitting with the raw data (top) and residual plot with the maximum error (bottom).

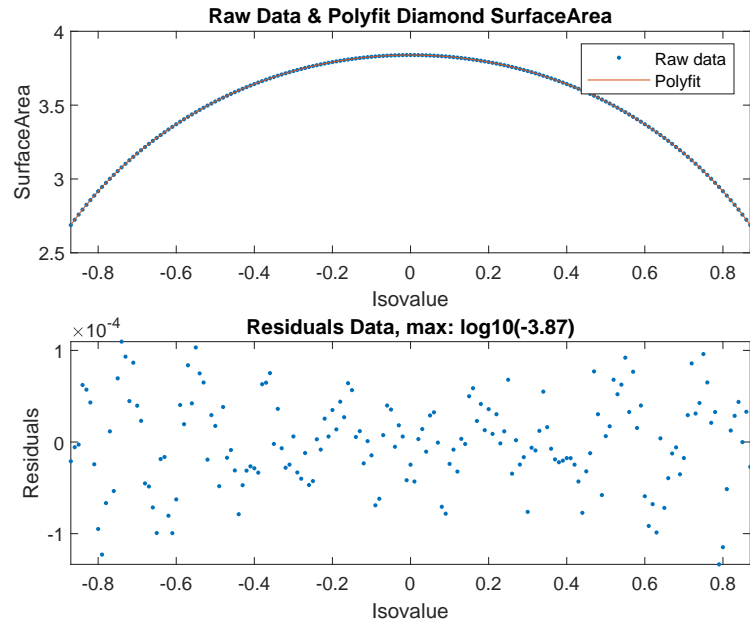


Figure A.15: Diamond single surface structure surface area: polynomial fitting with the raw data (top) and residual plot with the maximum error (bottom).

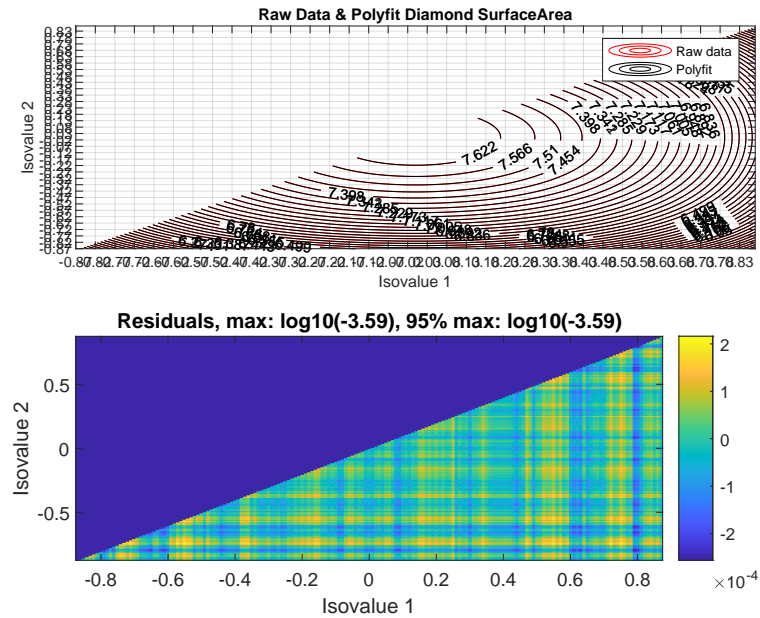


Figure A.16: Diamond double surface structure surface area: polynomial fitting with the raw data (top) and residual plot with the maximum error (bottom).

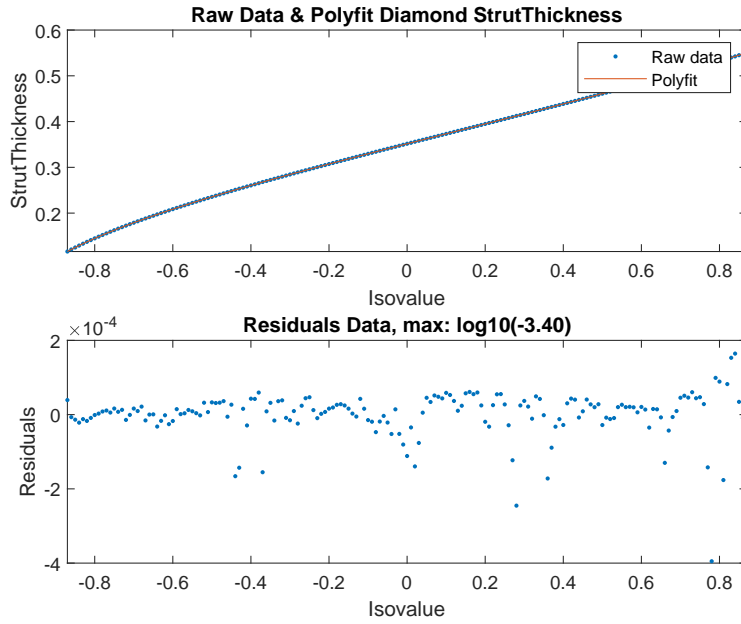


Figure A.17: Diamond single surface structure minimum thickness: polynomial fitting with the raw data (top) and residual plot with the maximum error (bottom).

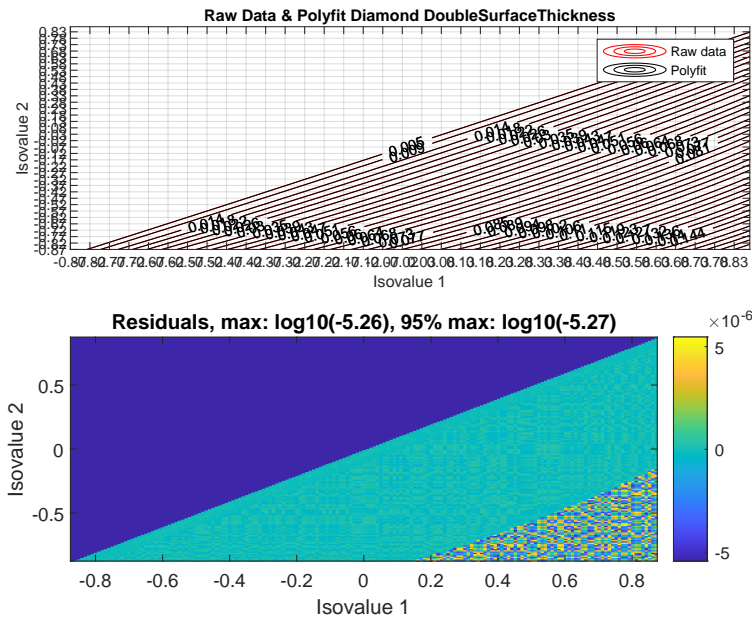


Figure A.18: Diamond double surface structure minimum thickness: polynomial fitting with the raw data (top) and residual plot with the maximum error (bottom).

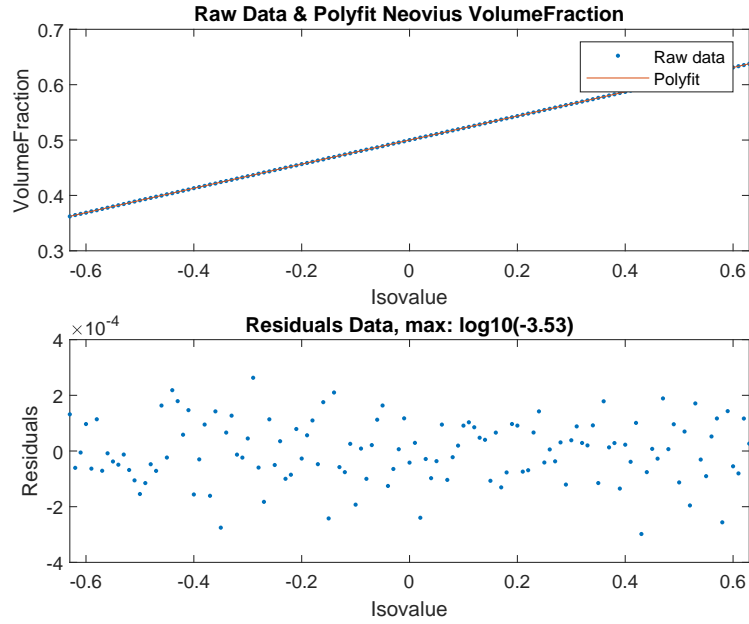


Figure A.19: Neovius single surface structure volume fraction: polynomial fitting with the raw data (top) and residual plot with the maximum error (bottom).

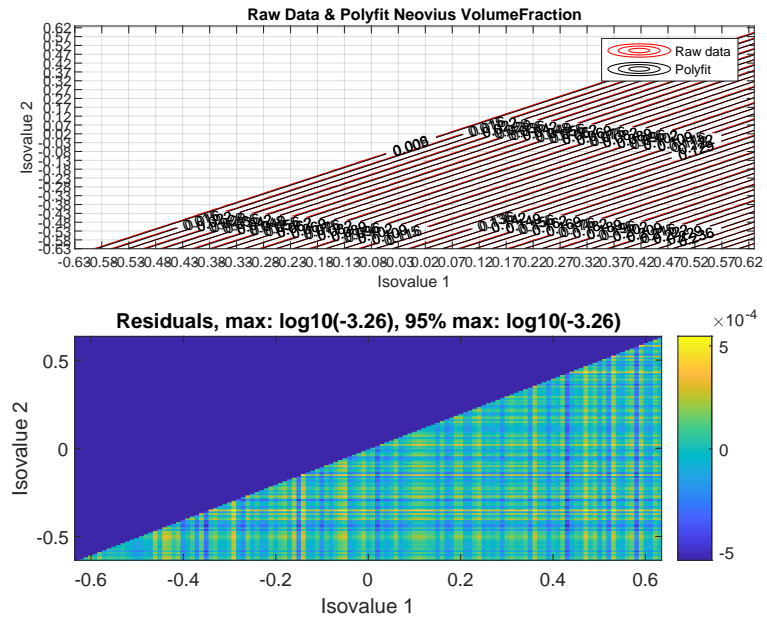


Figure A.20: Neovius double surface structure volume fraction: polynomial fitting with the raw data (top) and residual plot with the maximum error (bottom).



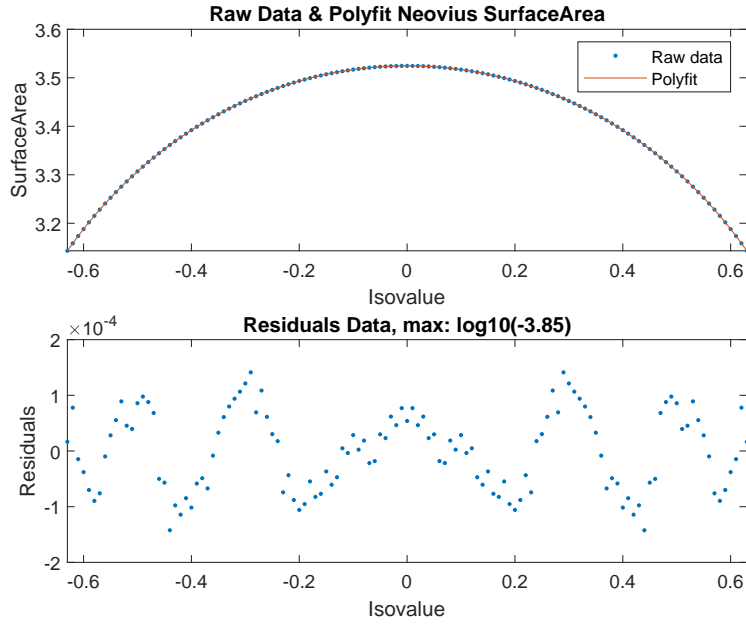


Figure A.21: Neovius single surface structure surface area: polynomial fitting with the raw data (top) and residual plot with the maximum error (bottom).

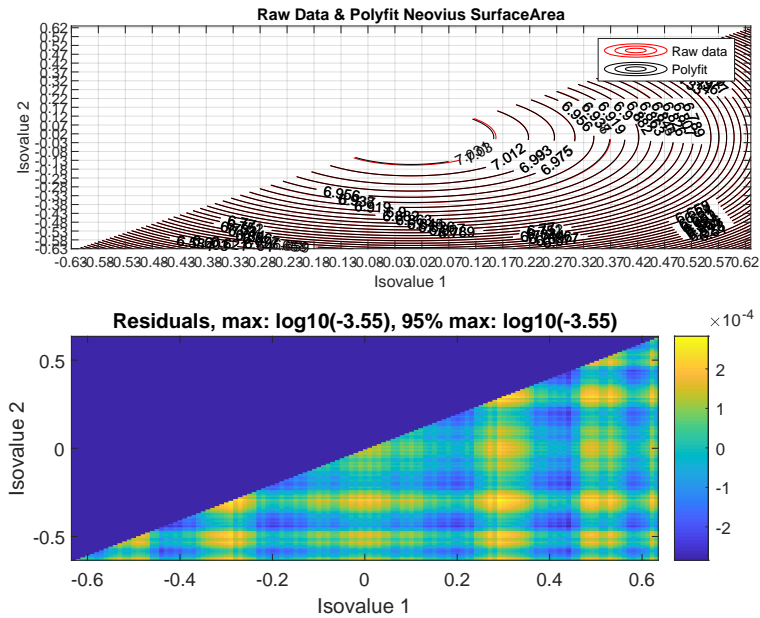


Figure A.22: Neovius double surface structure surface area: polynomial fitting with the raw data (top) and residual plot with the maximum error (bottom).

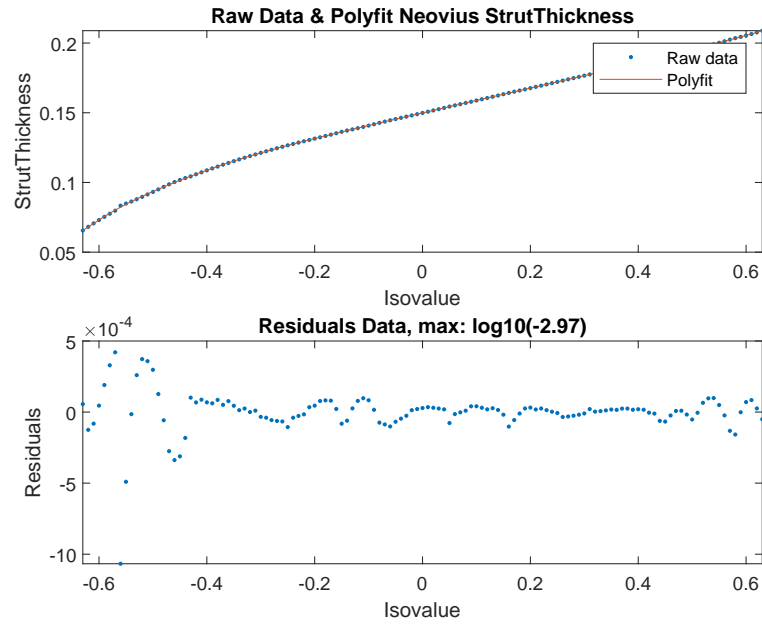


Figure A.23: Neovius single surface structure minimum thickness: polynomial fitting with the raw data (top) and residual plot with the maximum error (bottom).

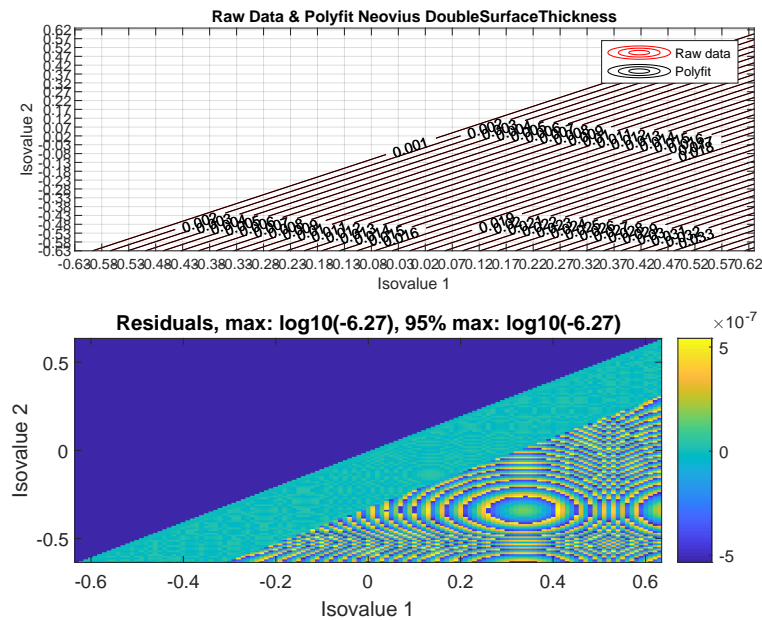


Figure A.24: Neovius double surface structure minimum thickness: polynomial fitting with the raw data (top) and residual plot with the maximum error (bottom).

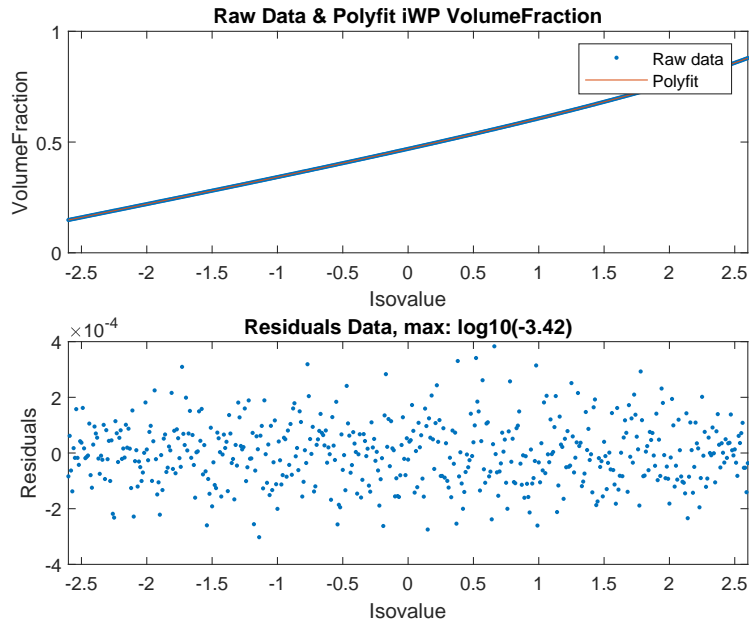


Figure A.25: iWP single surface structure volume fraction: polynomial fitting with the raw data (top) and residual plot with the maximum error (bottom).

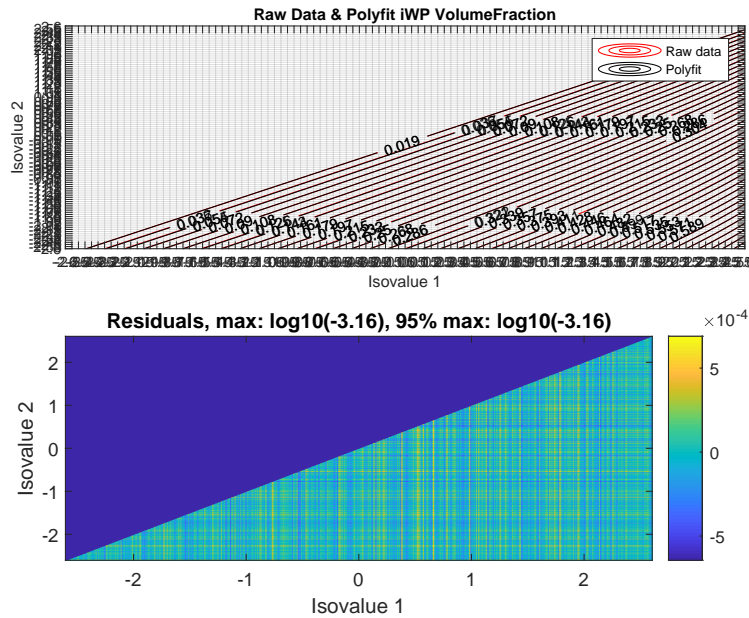


Figure A.26: iWP double surface structure volume fraction: polynomial fitting with the raw data (top) and residual plot with the maximum error (bottom).

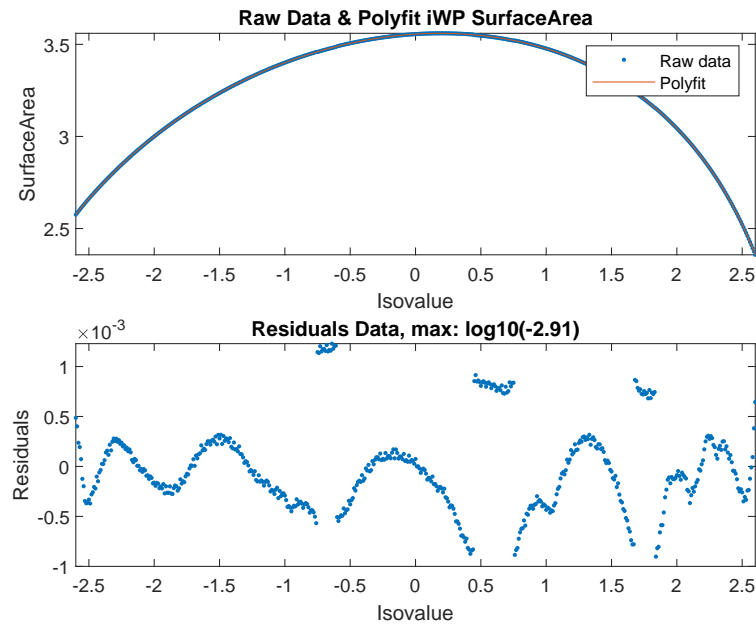


Figure A.27: iWP single surface structure surface area: polynomial fitting with the raw data (top) and residual plot with the maximum error (bottom).

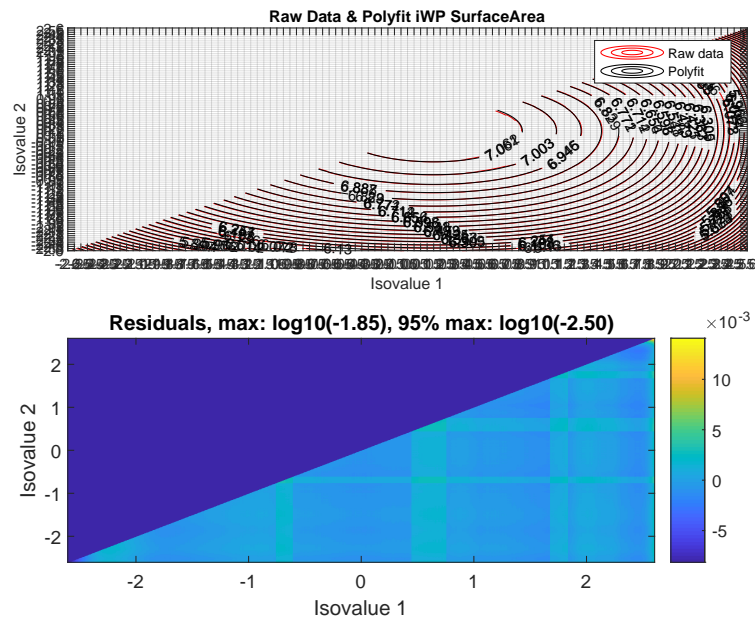


Figure A.28: iWP double surface structure surface area: polynomial fitting with the raw data (top) and residual plot with the maximum error (bottom).

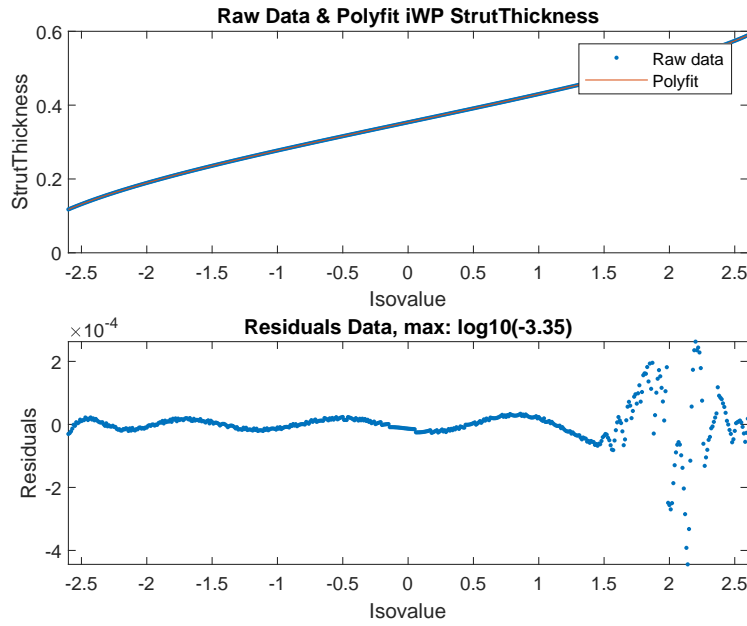


Figure A.29: iWP single surface structure minimum thickness: polynomial fitting with the raw data (top) and residual plot with the maximum error (bottom).

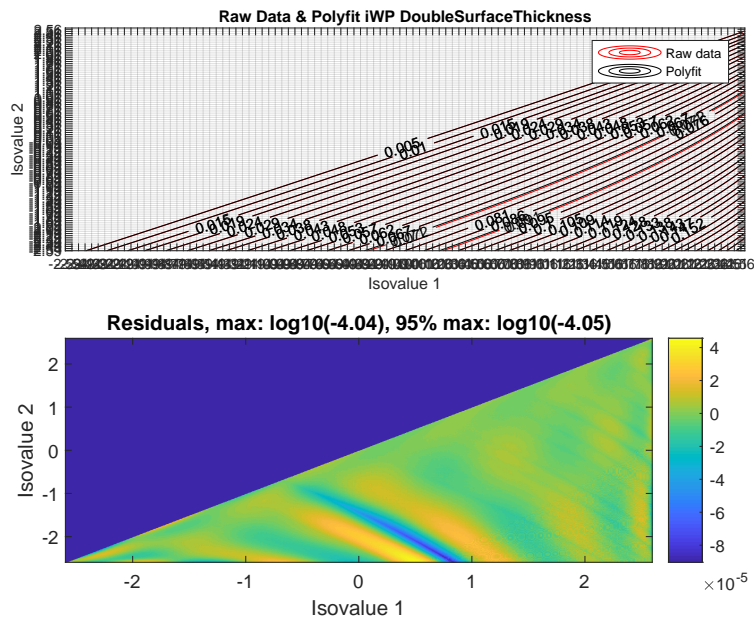


Figure A.30: iWP double surface structure minimum thickness: polynomial fitting with the raw data (top) and residual plot with the maximum error (bottom).

## Appendix B

### Appendix: Experimental Compressive Testing Plots

To establish the relationships to create Gyroid structures with tunable mechanical properties an experimental campaign was conducted in Chapter 7. Compressive testing related Gyroid structures with varying volume fractions with the Young's modulus based on the Gibson-Ashby relationship. The Gyroid specimens were printed using the direct slicing toolpath algorithm from Chapter 6 based on the geometric relationships from Chapter 5. was developed to create toolpath lines from TPMS implicit functions in Chapter 5.

The compressive testing on Gyroid double surface structures followed the ISO-604:2003 using the Instron 3369. There were eight thickness levels of varying volume fractions and each level had five repeat specimens for a total of 40 specimens. Below are the stress-strain plots where there are eight plots for each the thickness levels in order of increasing volume fraction. The five repeat specimen compression tests for each thickness level are plotted on the same graph. These plots are discussed in Section 7.5.

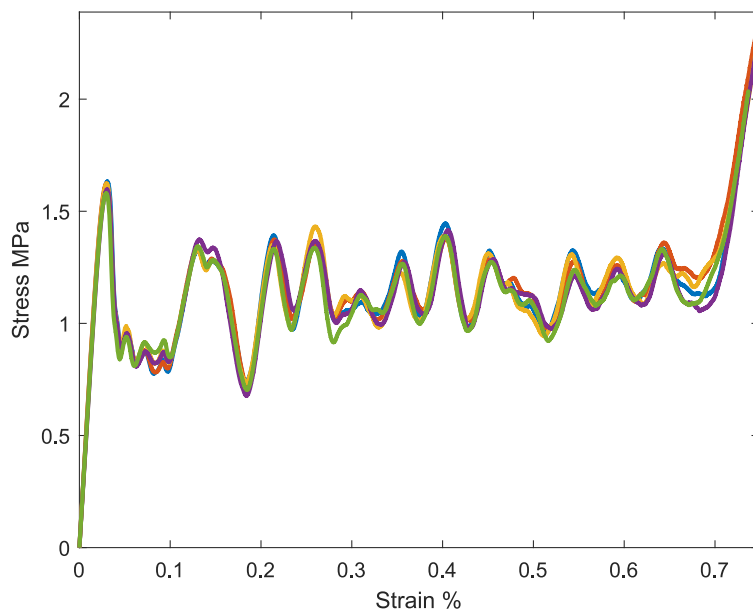


Figure B.1: Stress-strain plot for Gyroid double surface structure specimens, thickness level 1.

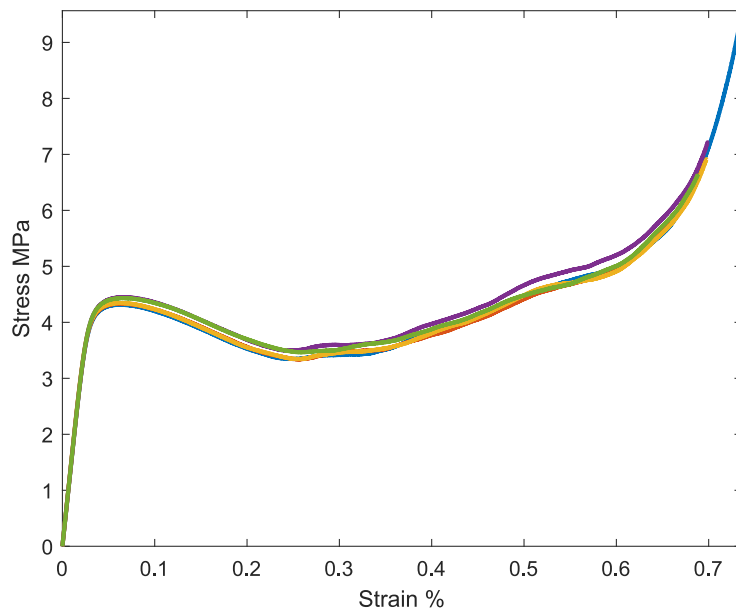


Figure B.2: Stress-strain plot for Gyroid double surface structure specimens, thickness level 2.

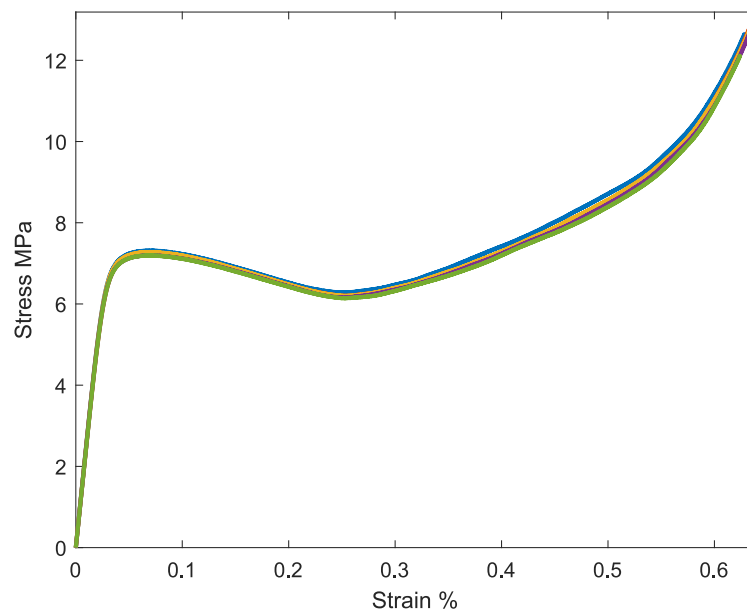


Figure B.3: Stress-strain plot for Gyroid double surface structure specimens, thickness level 3.

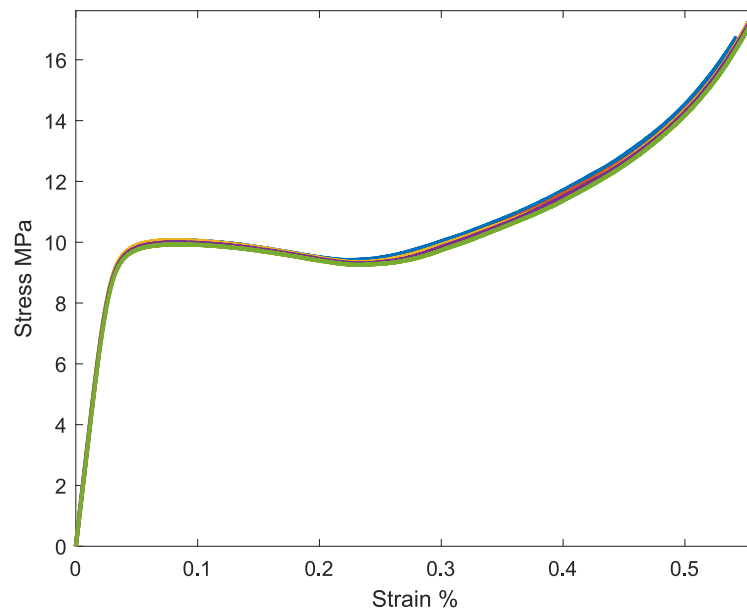


Figure B.4: Stress-strain plot for Gyroid double surface structure specimens, thickness level 4.



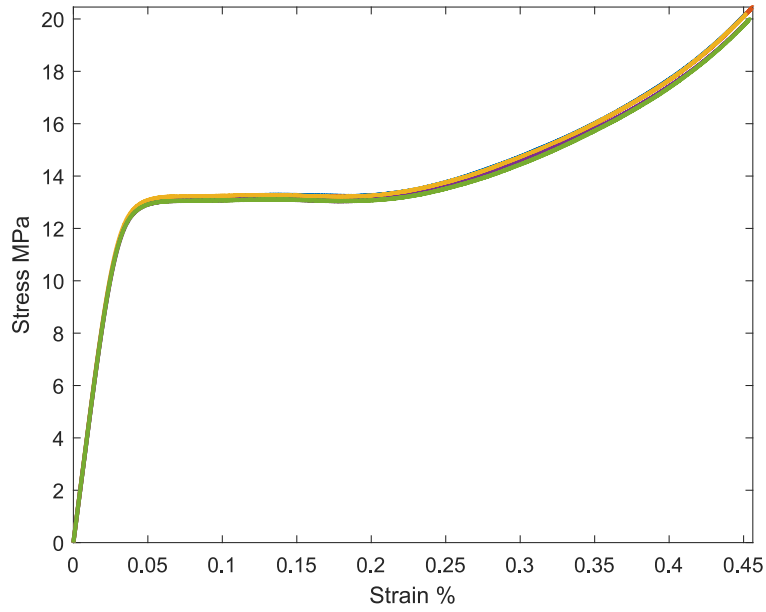


Figure B.5: Stress-strain plot for Gyroid double surface structure specimens, thickness level 5.

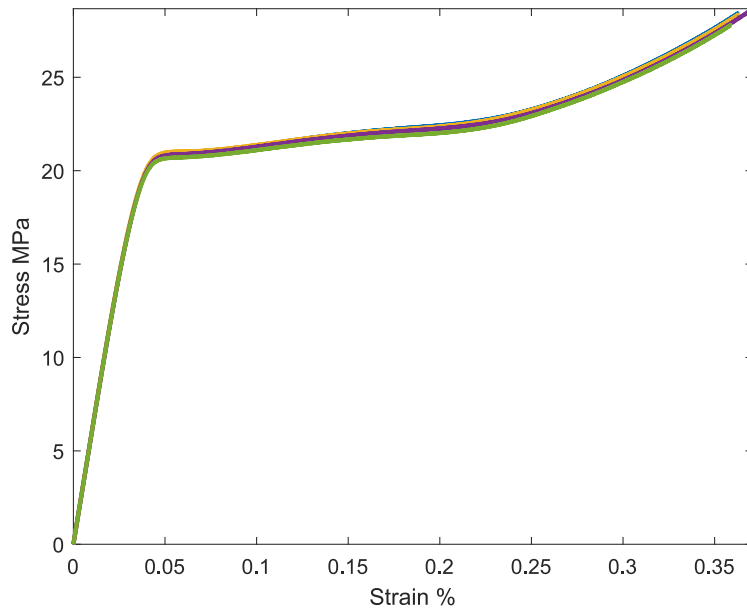


Figure B.6: Stress-strain plot for Gyroid double surface structure specimens, thickness level 6.

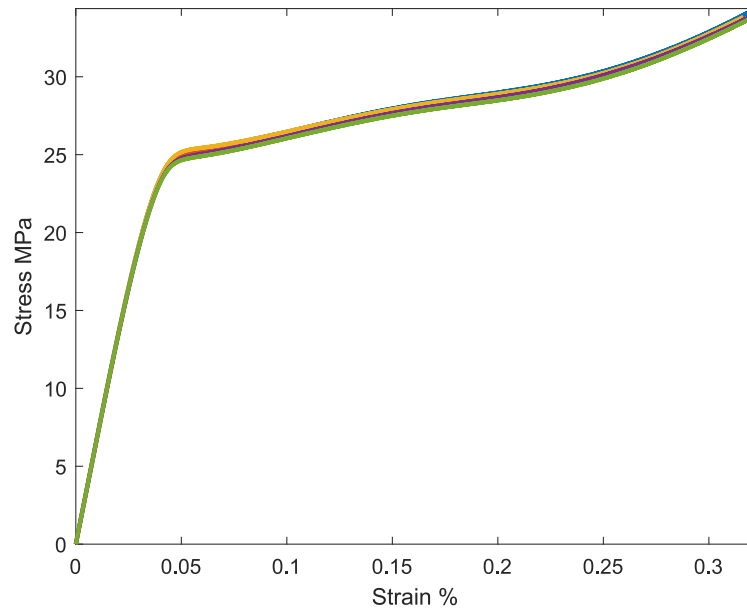


Figure B.7: Stress-strain plot for Gyroid double surface structure specimens, thickness level 7.

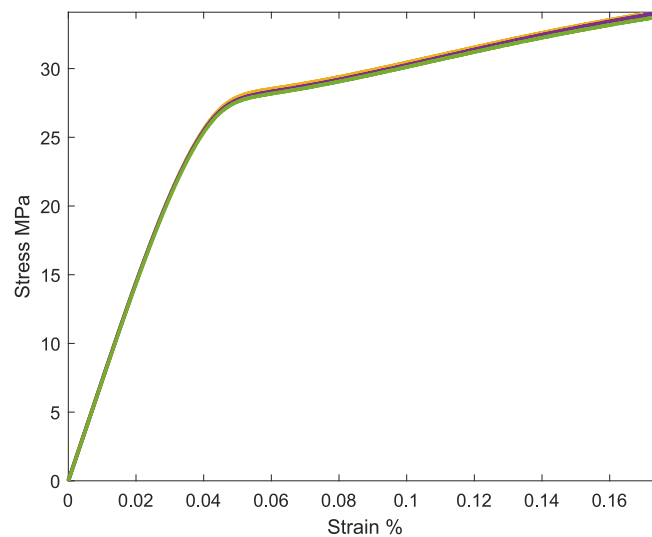


Figure B.8: Stress-strain plot for Gyroid double surface structure specimens, thickness level 8.